Non-Invasive Metal Detection

A Major Qualifying Project Report:

submitted to the Faculty

of the

WORCESTER POLYTECHNIC INSTITUTE

In partial fulfillment of the requirements for the

Degree of Bachelor of Science

By

_____

Brian M. Foley

_____

Sean Hallinan

_____

Hans Erik Jensen

Date: April 20, 2007

Approved:

_____

Professor Stephen J. Bitar, Major Advisor

_____

Professor Sergey Makarov, Co-Advisor

_____

Professor Reinhold Ludwig, Co-Advisor

Abstract

A system for detecting molten aluminum through six (6) inches of resin-bonded sand is presented. Its implementation is based upon the concept of eddy current testing as a means of non-destructive evaluation. This report details the design of an electro-magnet as a transducer and an Automatic Gain Control (AGC) circuit built upon an Op-Amp resonator. The project was funded by General Motors and the performance of the system was evaluated through testing with molten aluminum at Metal Casting Technology, Inc.

Table of Contents

Table of Figures

Table of Tables

Executive Summary

Metal Casting Technologies, Inc and General Motors Corporation are interested in the development of a feedback control system to be implemented in their Precision Sand-Casting (PSC) processes. When casting parts with complex geometries, sudden changes in volume as the molten metal fills the cast can cause significant defects to the structural integrity of the part. These defects can be minimized by controlling the flow rate of the molten metal. Therefore, the challenge presented by our sponsors is to create a sensor that can detect the presence and flow rate of molten aluminum through six inches of lake-sand bonded with a phenolic urethane. The information from this sensor could then be used to control the flow rate of the aluminum and consequently minimize the number of defects that occur in the part.

This report documents the development of the sensor for this feedback control system. An electromagnet transducer driven by a resonant Automatic Gain Control (AGC) circuit is presented as an effective means of detecting molten aluminum through six inches of bonded sand.

The theory behind its operation is based on eddy currents being induced in the molten aluminum. An eddy current is the circular flow of electric charge within a conductive medium that arises when it is subjected to a time-varying magnetic field. The circulation of eddy currents result in power losses dissipated within the conductive material in the form of heat. This power comes from the source of the time-varying magnetic field that is present, as its energy is coupled to the conductive medium.

In addition, the eddy currents that flow in the material produce their own magnetic fields which interact with the primary magnetic field. This interaction between the magnetic fields is called Mutual Induction. Mutual induction between a coil transducer and a conducting medium affects the electrical impedance, Z, of the transducer. By measuring changes in the resistive and inductive characteristics of the coils complex impedance, information can be gathered about the conducting material.

Figure 1: C-core coil sensor

The transducer in the system is the c-core coil sensor pictured in Figure 1. The sensor is comprised of a ferrite core serving as the coil former and 120 turns of 16 AWG magnet wire. When the coil is energized, the magnetic moments of the ferrite particles are aligned, causing an increase in the strength of the magnetic field emanating from the sensor. The shape of the coil keeps the majority of the magnetic energy aimed in the forward-direction by orienting both of the magnet's poles towards the region of interest.

With no aluminum present, the inductance and series resistance of the coil were measured with an LCR meter to be 1.5355 mH and 7.18 Ω, respectively. The total change in these values upon introducing a large aluminum plate positioned six inches from the coil were extremely small, deviating by less than 3.5%. To measure these small changes, an extremely sensitive drive-circuit was necessary.

To accomplish this, an op-amp resonator was developed with the coil-sensor serving as the inductor in an LC-tank network. This resonator serves as the foundation for an Automatic Gain Control (AGC) loop which compensates for ohmic losses due to mutual induction by increasing the gain of the op-amp resonator as aluminum is detected by the transducer. The AGC circuit varies the gain of the resonator by adjusting the R_{DS} value of a CD4007 MOSFET device based upon an error signal corresponding to the amount of deviation between a predetermined voltage value and the actual voltage across the transducer. This error signal can then be measured and processed to determine the position of the aluminum with respect to time.

Several tests with both solid and molten aluminum were performed, requiring a variety of data acquisition (DAQ) systems. Two DAQ systems were created that interfaced LabView 8.0 with the Agilent MSO6012A Oscilloscope and acquired data from both single and multiple-coil system configurations. A third DAQ system was developed with the Data Acquisition Toolbox (DAT) in MATLAB and the 1608FS hardware DAQ from Measurement Computing to enable higher sample rates and streamline the process for analyzing the data.

Initial tests were performed with solid aluminum to determine the field-of-view (FOV) of the c-core sensor for calibration purposes. Using a linear-motion table to move a sheet of aluminum into the coils magnetic field at a constant rate, the vertical FOV of the c-core sensor was determined to be ±3.5 inches from the center-line of the coil (seven inches total) as shown in Figure 2.
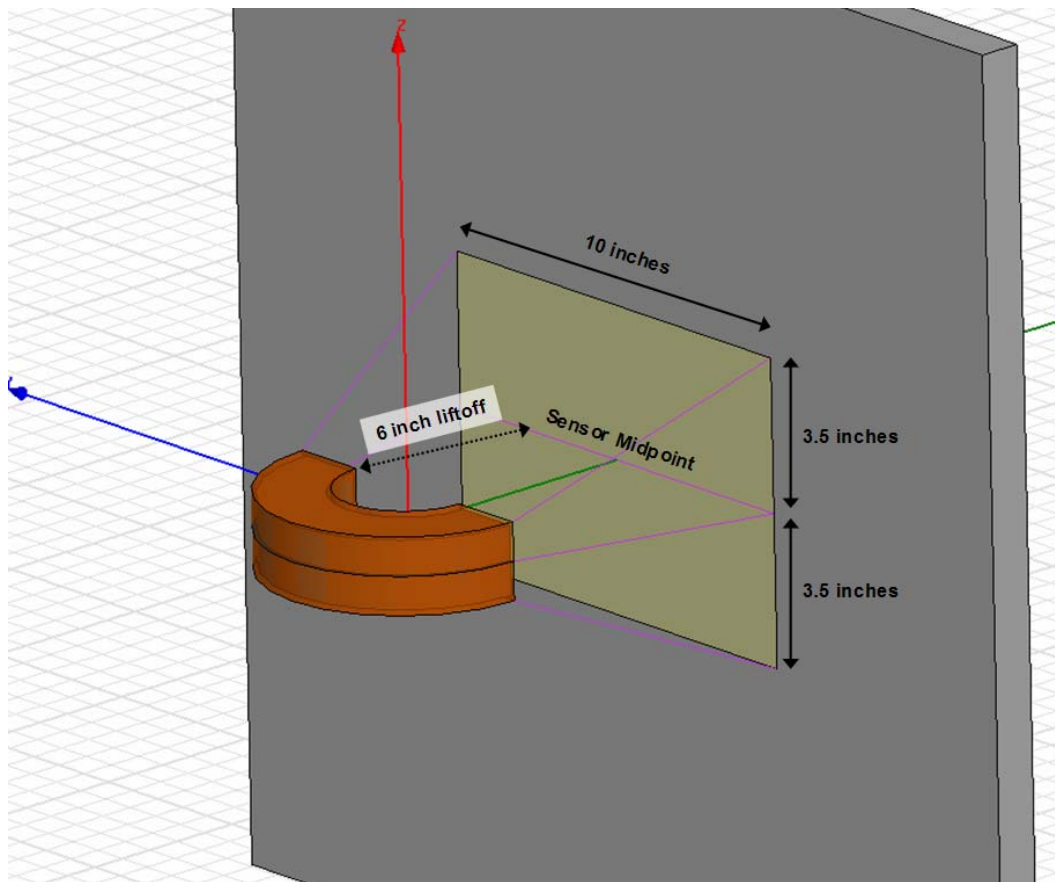
Figure 2: Field-of-View (FOV) of the C-core coil

Three separate tests were performed with molten aluminum at Metal Casting Technologies in Milford, NH. The first and second tests on November 10th, 2006 and December 8th, 2006 were for proof-of-concept purposes concerning single and multiple coil configurations.

The third test on March 5th, 2007 was intended to evaluate the performance of the AGC circuit and establish the resolution of the system.

In the third test, thermocouples were placed in the mold as a means of validating the accuracy of the metal sensing system. Based on the data acquired from both the coil-sensor and the thermocouples, it was determined that the molten-metal sensing system was capable of determining the position of the metal to within an uncertainty of ±0.25 inches, largely due to the noise present on the signal. The plot in Figure 3 depicts the comparison between the sensor signal and the thermocouple traces.
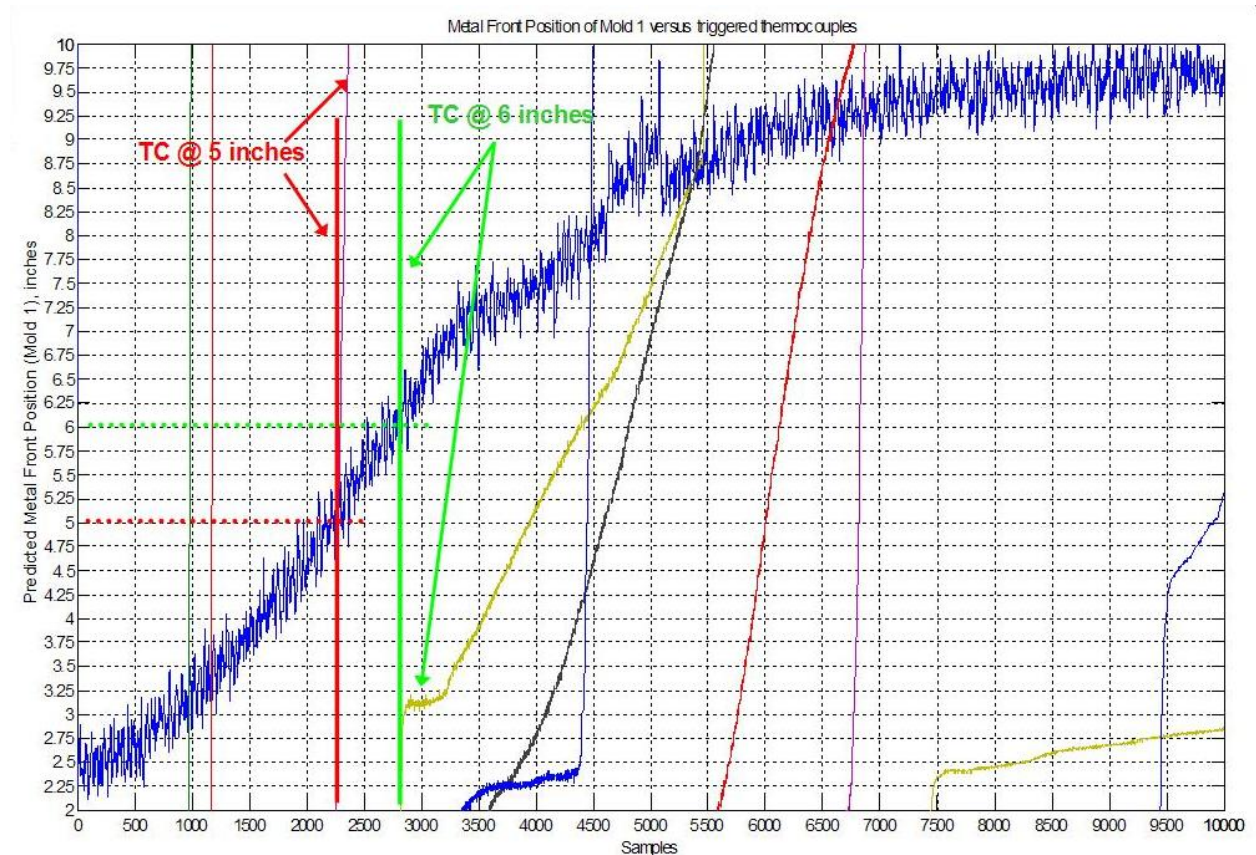
Figure 3: Sensor signal and thermocouple data illustrating the accuracy of the AGC system

While the accuracy of the system was good, a lack in repeatability between subsequent experiments was identified. A drift in the output signal from the AGC circuit was observed between consecutive tests, affecting the sensitivity of the system. This drift is caused by temperature variations in the vicinity of the AGC circuit, affecting the electron mobility of semiconductor devices present in the closed compensation loop. If the sensitivity of the system

is not constant from one mold to the next, it will be impossible to predict the position of the aluminum metal front in real-time to an appropriate degree of accuracy.

Further research is necessary to eliminate this temperature-dependency, either through in-circuit compensation or some other circuit configuration which eliminates the temperature-sensitive components. Additionally, the coil sensors could be optimized to both create a specific field-of-view, as well as increase the sensitivity of the coil via different techniques of magnetic field-focusing.

1 Problem Statement

General Motor Corporation (GM) and Metal Casting Technologies (MCT), a subsidiary of GM and Hitchner Manufacturing, are faced with many challenges and problems associated with the casting of GM's V-block engines. Due to the engine block complexity, it is very difficult to machine an engine block from a single piece of aluminum. As an alternative, a method called Precision Sand Casting (PSC) makes it possible to cast an engine block with great ease and dimensional accuracy. The eight-cylinder, V-block engine is an example of a part that GM creates using the PSC method.

Due to the complex geometry of some cast parts, there is inevitably a host of problems that a metallurgist must address to produce a quality casting. In the case of the V-block engine, there are a variety of areas that pose a problem. Looking at the side view of the engine block as seen in Figure 1.1, it can be seen that the profile of the block results in a constantly changing part-volume. An important piece of information to note is that the aluminum is pumped into the mold from below. If the flow-rate of the molten aluminum is not increased as the volume of the fill cavity increases, and the flow-rate is not decreased when the volume decreases, many problems can occur.

Figure 1.1: Side profile of a V-block engine (upside-down)

In addition, Figure 1.2 identifies an area referred to as the "skirts" (outlined in yellow) of the engine block. The point at which the skirts branch from the bulk of the engine block

represents one of the thick to thin transitions mentioned. These volumetric transitions cause a problem when molten material is being pumped at a very high rate of flow, used to fill the very large cavity, then the volume of the cavity suddenly decreases creating a significant increase in back-pressure within the mold. This pressure can cause a variety of problems, such as the dislodging of some of the sand within the mold or even a sudden stop in metal flow altogether.
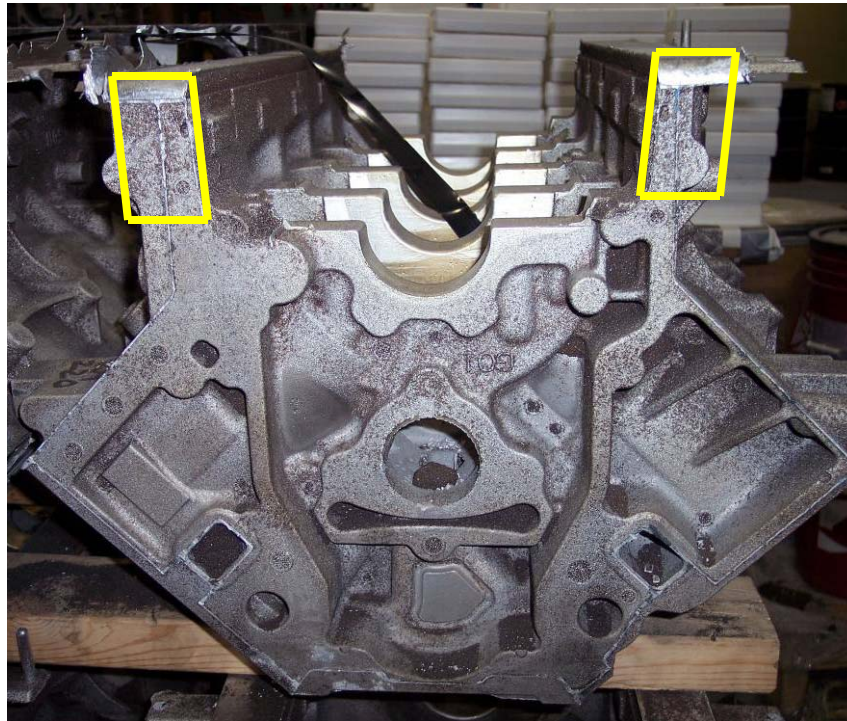
Figure 1.2: Side profile of a V-block engine with skirt areas highlighted

The best way to avoid problems such as these would be to adjust the flow rate of the material when thick to thin volume transitions occur. However, it is very difficult to know or predict where the molten material is within a sand cast at any given moment. For one thing, it is impossible to monitor the process visually since the cavity is completely encased in sand. Furthermore, parameters such as flow-rate, melt temperature and even atmospheric pressure are too inconsistent from pour to pour to allow engineers to predict the location of the melt within the cast as a function of time.

The goal of this project was to create a system that could determine the position of an aluminum molten-metal front though six (6) inches of resin-bonded sand. The system needs to be as accurate as possible and produce repeatable, consistent results. Ultimately, the system would be interfaced with the aluminum delivery system (an electromagnetic pump) to make adjustments to the metal flow-rate in real-time.

2 Background

This section will provide background information about eddy currents, specifically Faraday's Law, mutual inductance, skin depth, and impedance. It will also give insight into precision sand casting and how eddy currents are utilized in this project.

2.1 Eddy Currents

The scientific foundation for our project comes from the phenomena of induced eddy currents. An eddy current (also known as a Foucault current) is the circular flow of electric charge within a conductive medium that arises when it is subjected to a time-varying magnetic field. The circulation of eddy currents result in power losses dissipated within the conductive material in the form of heat. This power comes from the source of the time-varying magnetic field that is present, as its energy is coupled to the conductive medium. The coupling of the energy between a magnetic field and a conductive circuit path is known as mutual induction; the principle upon which the operation of a transformer is based. This phenomenon can be explained mathematically through Faraday's Law, and more generally by one of Maxwell's equations for time-varying fields.

2.1.1 Faraday's Law

On opposite sides of the Atlantic Ocean, two scientists were performing similar experiments with an identical hypothesis that since electric fields create magnetic fields, then magnetic fields should somehow create electric fields. In 1831, both Michael Faraday in London, England and Joseph Henry in Albany, NY proved their hypotheses to be true by discovering that magnetic fields can produce electric current in a closed conducting path, but only if the magnetic flux linking the surface area of the loop changes with time [1].

The two scientists were able to prove their results to be true with the help of a device called a galvanometer, which simply detects electric current in a circuit. A loop of wire was connected to the galvanometer and a conducting coil, wired to a battery, was placed nearby. The two scientists found that in the instant when the battery was connected and disconnected, to and from the battery, the galvanometer indicated the flow of current within the loop of wire. What

followed was the aforementioned finding that a changing magnetic field (and therefore, a changing magnetic flux) would cause an electric current to flow in a closed path [1].

Though both scientists arrived at the same discovery independently of one another at about the same time, the finding is attributed to Faraday and the resultant mathematical expression is known as Faraday's Law, Equation 2.1.

$$V_{emf} = -N\frac{d\vec{\Phi}}{dt}$$

Equation 2.1

The above equation states that the electromotive force, V_{emf}, induced in a closed conducting path (ie, a loop of wire) is equal to the negative time rate of change of the magnetic flux, multiplied by the number of closed paths (ie, number of wire loops). The expression in Equation 2.1 can also be related to the magnetic field directly by the definition of magnetic flux, Φ, being the integral of the dot-product between the magnetic field, **B**, and a given surface, **S**.

$$\Phi = \int_S \vec{B} \cdot d\vec{s}$$

Equation 2.2

If we substitute Equation 2.2 into Equation 2.1, we get an expression for the induced emf, V_{emf}, in terms of **B**.

$$V_{emf} = -N\frac{d}{dt}\int_S \vec{B} \cdot d\vec{s}$$

Equation 2.3

The process through which the rate of change of **B** through a given surface, S, creates an electromotive force in a conducting path is called electromagnetic induction. We can take the expression in Equation 2.3 a few steps further to derive the integral and differential forms of Faraday's law in Maxwell's Equations.

We know from electrostatics that the voltage potential at a given point, P, is equal to the integral of the electric field dotted with the path chosen from the point P to infinity.

$$V = \int_{P}^{\infty} \vec{E} \cdot d\vec{l}$$

If we expand this idea of summing the dot-product of **E** with d**l** to our loop of wire, we can state that the V_{emf} across a closed path or contour, C, is equal to the integral of the electric field along that contour.

$$V_{emf} = \oint_{C} \vec{E} \cdot d\vec{l}$$

We now have an expression for the V_{emf} across a closed loop in terms of the Electric field, **E**. If we substitute Equation 2.5 into Equation 2.3 and set the number of turns, N, equal to 1 (N=1), the resultant expression is the integral form of Faraday's Law in Maxwell's equation:

$$\oint_{C} \vec{E} \cdot d\vec{l} = -\frac{d}{dt} \int_{S} \vec{B} \cdot d\vec{s}$$

The significance of this expression is that the electric field, **E**, along a closed contour can be related to the negative time-rate of change of the integral of the magnetic field, **B**, through the surface, S, which is bounded by the contour, C. The implications of this are enormous with regards to eddy currents because the closed path of the electric field can be directly related to the conducting path of a current, I.

This relationship may be easier to recognize in the differential form of Equation 2.6. By applying Stokes' Theorem (Equation 2.7, classical form) to the left hand side of Equation 2.6, and then canceling the two surface integrals, the result is the form in Equation 2.8.

$$\int_\Sigma \nabla \times \vec{F} \cdot d\Sigma = \oint_{\partial\Sigma} \vec{F} \cdot d\vec{r}$$

<div align="right">**Equation 2.7**</div>

$$\nabla \times \vec{E} = -\frac{\partial \vec{B}}{\partial t}$$

<div align="right">**Equation 2.8**</div>

Equation 2.8 tells us that the curl, or circulation of the electric field is equal to the negative time-derivative of the magnetic field. Once again, since the electric field can be directly related to the current that flows in a conductor, Equation 2.8 describes the circular (eddy) flow of current due to a changing magnetic field [1].

2.1.2 Mutual Inductance

Once we are comfortable with how eddy currents are created within a piece of conductive material, we may begin to understand how this phenomenon can provide us with useful information. Once the eddy currents have been created via electromagnetic induction, the story does not stop there. Just as Faraday and Henry knew in the 19th century, an electric current produces a magnetic field. Therefore, the eddy currents that flow in the material must produce their own magnetic fields. These magnetic fields interact with the primary magnetic field that created the eddy currents in the first place, and by measuring the changes in the resistive and inductive reactance of the coil, we can gather information about the conducting material [2].

This interaction between the magnetic fields (and therefore the currents) in each of the conducting structures in the system is called Mutual Induction, whose quantitative value is denoted by the constant, M. The value of M is largely dependent upon the geometric arrangement of the two circuit structures. For example, if the two structures are close together, a large portion of their respective magnetic fluxes will be shared between the two circuits and the value of M will be relatively large. On the other hand, if the structures are far apart, there will be a small amount of flux being shared between the two and the value of M will be much smaller. In eddy current testing, this distance of separation between the conducting coil and the test material is called liftoff and as was just explained, an increase in liftoff results in a decrease in mutual inductance and vice-versa [2].

2.1.3 Skin Depth

The behavior of the eddy currents within the conductive medium is a very interesting topic and an item of great concern in many applications of eddy current testing (ECT). We have already established that eddy currents flow in closed loops in planes that are perpendicular to the magnetic flux that creates them. However, if we look at the cross-sectional current density of the conductive path, we find that eddy currents concentrate near the surface of the material closest to the source of magnetic flux, decreasing exponentially with depth as seen in Figure 2.1.
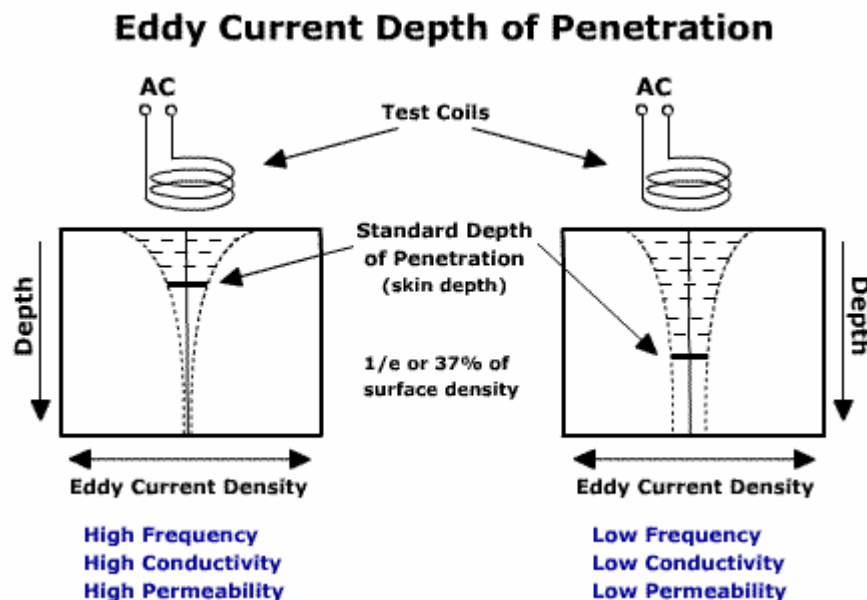
Figure 2.1: Eddy currents generated in a test material by a coil [3]

This is referred to as the skin effect and is directly related to the concept of mutual induction described previously. As the eddy currents flow, they produce a magnetic field that opposes the primary field. The currents closest to the surface have the largest effect on the primary field, thereby reducing the total amount of magnetic flux penetrating the material. Because the strength of the magnetic field is decreasing with depth into the material, the eddy currents being induced are therefore weaker, distinguished by a decreasing current density.

The skin effect is characterized by some specific system properties that affect the depth that eddy currents may penetrate a material. The depth of penetration decreases with increasing frequency, f, of the alternating magnetic field, as well as with increasing conductivity, σ, and magnetic permeability, μ, of the material. This inverse relationship can be seen in Equation 2.9

below, where δ represents the standard depth of penetration, or skin depth, which is equal to 37% (1/e) of the surface current density [3].

$$\delta = \frac{1}{\sqrt{\pi\mu\sigma \cdot f}}$$

f = Test frequency (Hz)

σ = Electrical conductivity (%IACS)

μ = Magnetic permeability (H/mm)

In many applications of ECT such as flaw detection, the skin depth is an extremely important design consideration. Cracks or flaws that are much larger or smaller than the skin depth, δ, may provide false flaw-locations or be undetectable due to a lack of resolution.

2.1.4 Impedance

As we established in the section on mutual inductance, we can gather information about the test material of interest by measuring changes in the resistive and inductive characteristics of the conducting coil. These characteristics constitute the electrical impedance, Z, of the coil which is defined as the total opposition of a circuit to an alternating current (measured in ohms, Ω). In general, the impedance may include three different characteristics: Resistance (R), Inductive Reactance (X_L) and Capacitive Reactance (X_C). For our discussion, we are primarily concerned with R and X_L, since the influence of X_C in a coil structure is often negligible.

Since R and X_L are 90° out of phase with one another, vector addition must be used to calculate the total impedance due to the individual constituents. In many systems designed for ECT, the impedance plane diagram is used to graphically detect changes in the R and X_L of a sensor system.
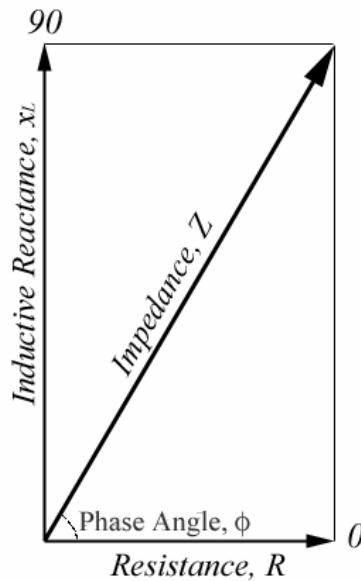
Figure 2.2: Complex Impedance Plane (1st quadrant only)[4]

The impedance plane shown in Figure 2.2 is based on vector addition. The amplitude of the resistive component is mapped to the horizontal axis (0°) and the amplitude of the inductive reactance to the vertical axis (90°). If these two vectors are summed together, the resultant vector is the total impedance, where the magnitude is related to the length of the vector and the phase angle will be between 0° and 90°. The geometric expressions for the magnitude and phase angle of the impedance vector are given below.

$$Z = \sqrt{X_L^2 + +R^2}$$

<div align="right">**Equation 2.10**</div>

$$Tan\phi = \frac{X_L}{R}$$

<div align="right">**Equation 2.11**</div>

Let us now discuss how the introduction of aluminum into the magnetic field of a coil would affect its impedance and therefore allow us to detect the presence of the material. If our sensor-circuit were balanced with only air in the surrounding region, the impedance of the coil would correspond to a specific point in the impedance plane, indicated as point A in Figure 2.3.

If a piece of aluminum is introduced to the coil's magnetic field, the resistive component of the impedance will increase while the inductive component will decrease. The result of these two changes is an associated change in the total impedance of the coil from point A to point B in Figure 2.3.
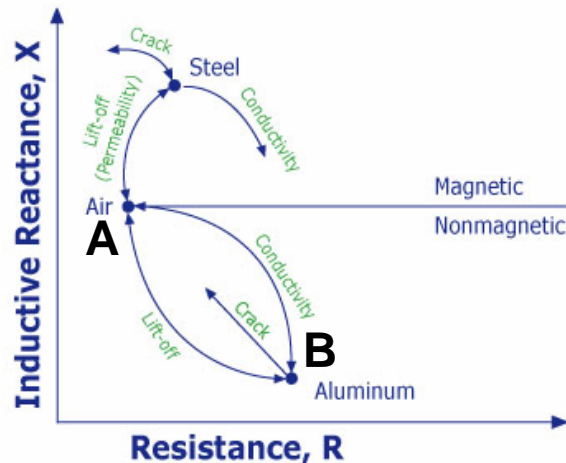
Figure 2.3: Impedance change from point A to point B when aluminum is introduced[5]

The reason that the resistive component increases is that energy which was stored in the magnetic field is being dissipated in the aluminum as the eddy currents circulate. The losses attributed to the resistive component of any coil structure are often referred to as the ohmic losses in a system.

Similarly, the decrease in the inductive component is associated with the net decrease in magnetic flux caused by the eddy currents due to mutual induction. If the test material were something magnetic like steel, the inductive component would increase since the steel would strengthen the magnetic field of the coil [5].

2.2 Precision Sand Casting

Precision sand casting (PSC) is a material forming process capable of producing castings of complex geometries with optimum mechanical properties, excellent dimensional precision and good surface finishes. As a result, PSC has been employed extensively by the aerospace and automotive industries in applications with significant structural demands. Examples of such

applications include various engine blocks, as well as the front mounting frames of turbojet engines. [6]

As capable as the PSC process already is, there is a persistent demand for improved casts in a variety of areas, including higher strength, increased dimensional accuracy, shorter lead times, etc. However, above all else is the goal to achieve consistency from part-to-part by the most cost-effective means possible. The consistency with which a process creates parts of minimum variability, both dimensionally and mechanically, depends upon the controls imposed in the manufacturing process. [6]

As the requirements demanded by industry raise the bar for PSC, there are a variety of challenges that metallurgists are faced with. Certain characteristics of a mold, such as thick to thin transitions, extensive horizontal or flat surfaces and sharp corners increase the likelihood of a defect due to the turbulent metal-flow that they can cause during fill. Therefore, it is critical that turbulent flow be minimized, and the best way to do this is by carefully distributing the metal at the appropriate flow rate throughout the mold. [6]

2.3 Eddy Current Application

For our purposes, eddy-current testing (ECT) was selected as the scientific basis for our system. ECT is often used to detect flaws or defects in a conductive material through electromagnetic induction. The system is initially calibrated according to what it would expect to see from an area free of defects, and it then uses this information for comparison with what it actually sees from a device-under-test (DUT). ECT can detect very small defects at or near the surface of a material with minimal part-preparation and the sensors do not need to contact the DUT. However, there are also some limitations of ECT, such as limited penetration into the material, error caused by surface roughness, etc [7], [8].

Our system will employ the same basic principles as ECT in that we will use a changing magnetic field to induce eddy currents in the molten aluminum. The difference is that instead of detecting flaws, we will be using the technology to determine the presence and flow rate of the aluminum as it fills the sand cast.

3 System Design

This section will detail the design and construction of the complete non-invasive metal detection system. The electromagnetic sensor, the oscillator circuit, and the data acquisition system will all be discussed.

3.1 Electromagnetic Sensor

The sensor in the non-invasive melt monitoring system is the c-shaped electromagnet pictured in Figure 3.1. The sensor, herein referred to as the c-core coil, is comprised of a ferrite core serving as the coil former and 120 turns of 16 AWG magnet wire. Figure 3.2 is a dimensioned drawing of the c-core coil, indicating the inner and outer diameters, as well as the height of the c-core coil design.

Figure 3.1: C-Core Electromagnet Coil
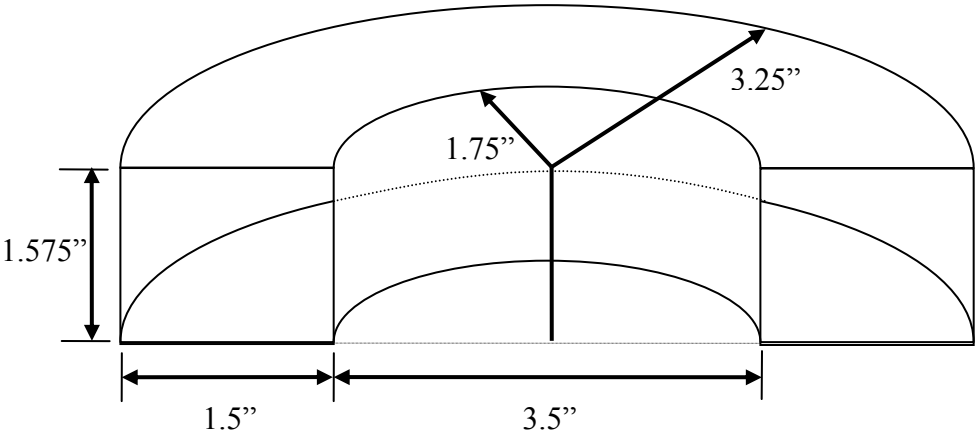
Figure 3.2: C-Core Electromagnetic Coil Dimensions

The design of this sensor evolved from a simple air-core solenoid to that pictured in Figure 3.1 as the result of two major design decisions. The first of these concerned the decision to create a "loaded" coil (meaning a coil whose core is comprised of a magnetic material) versus an "air-core" coil. The second concerned the shape of the electromagnet, specifically the decision between a cylindrical coil (solenoid) versus a c-shaped coil. Both of these design decisions were initially based on observations from actual experimentation and were validated through simulation in Maxwell 3D; a three-dimensional electromagnetic field simulation software package created by the Ansoft Corporation.

Figure 3.3: Air-Core Solenoid

Experimentation began with the air-core solenoid pictured in Figure 3.3. Using an LCR meter (the 4284A from Agilent Technologies) to measure the impedance of the coil (real and imaginary components), three different aluminum samples were moved across the aperture of the coil at a distance of four (4) inches from the coil. As the samples were brought into the magnetic field of the coil, the measured impedance of the coil was monitored and recorded to observed relative changes in the electrical characteristics of the coil due to the presence of the aluminum. For each sample, the air-core solenoid was driven at three different frequencies. Figure 3.4 illustrates this experimental procedure, while Figure 3.5 depicts a plot of the coil's impedance with respect to the position of the aluminum sample.

Inner Diameter of Coil (Aperture) = 2.7 cm (1.1 in)
Outer Diameter of Coil = 6.3 cm (2.5 in)
Length of Coil = 7 cm (2.6875 in)

Aluminum Samples

4 in

Distance from Coil Axis, *d* (cm)
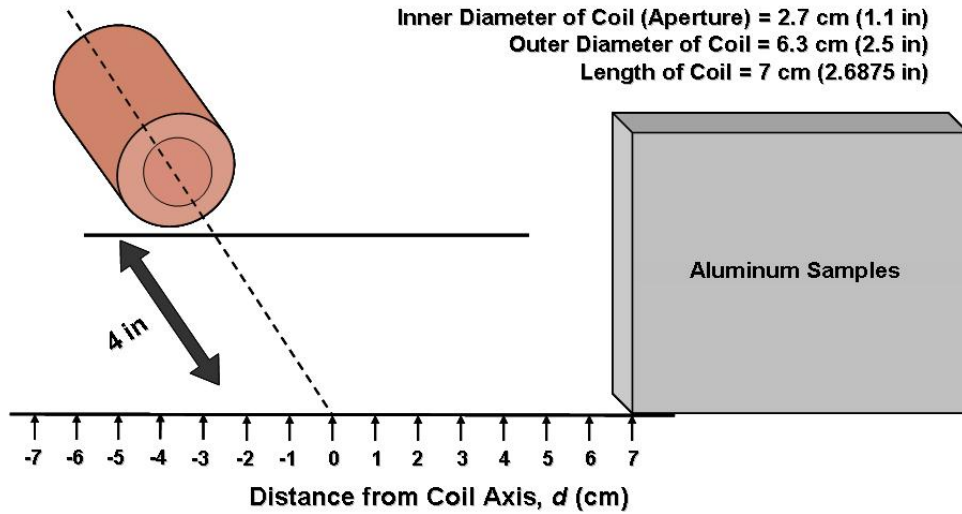
Figure 3.4: Experimental Setup with the Air-Core Solenoid

Plot depicting the decreasing impedance of the coil as the Aluminum samples
are moved into the B-field (from right to left)

Effective "Viewing Area" of Coil at 4 in (air gap)

Coil Impedance Magnitude, |Z| (ohms)
scaled up by 10^4

Distance from sample edge to coil axis, d (cm)

- Plate A: 350 Hz
- Plate A: 500 Hz
- Plate A: 1 kHz
- Bar A: 350 Hz
- Bar A: 500 Hz
- Bar A: 1 kHz
- Plate B: 350 Hz
- Plate B: 500 Hz
- Plate B: 1 kHz
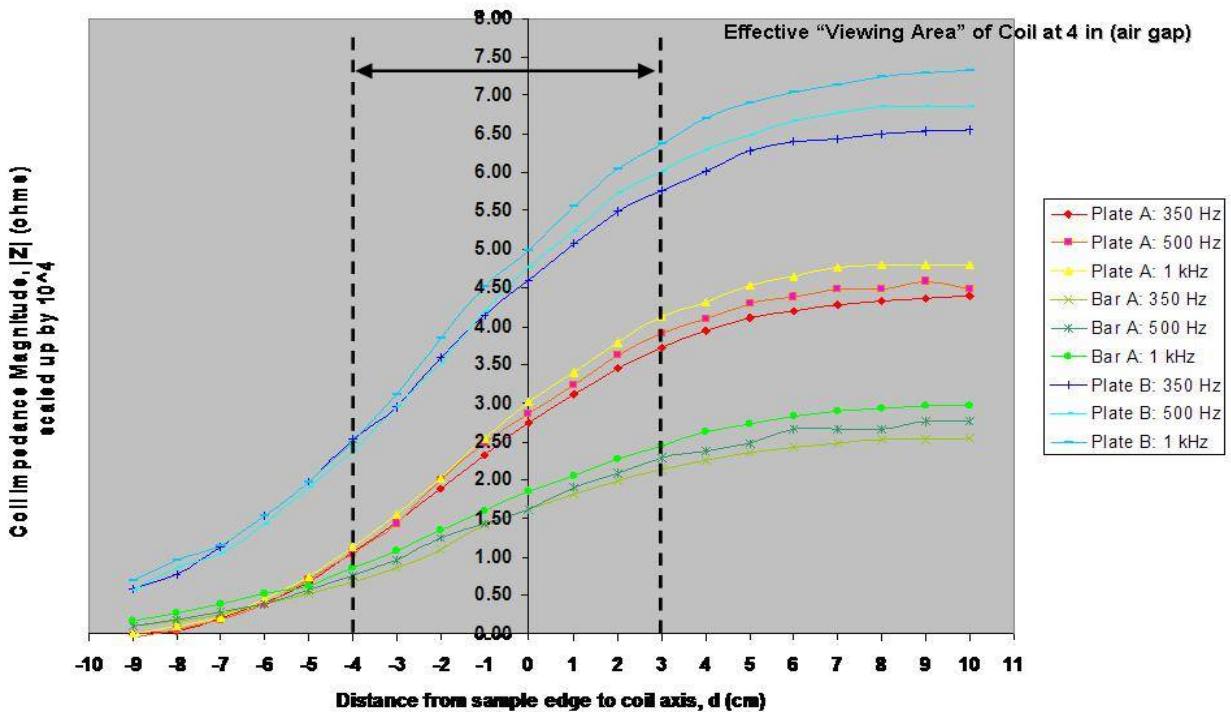
Figure 3.5: Coil Impedance as a function of aluminum position

The plot in Figure 3.5 shows a fairly linear characteristic between the dashed lines in the response of the coil's impedance as the amount of aluminum within its magnetic field increases. This linear response is quite desirable from a transducer/sensor in many measurement systems.

14

However, the scale of the impedance change is on the order of only a few milliohms. To accurately measure fluctuations like these on such a small order of magnitude, extremely precise and expensive equipment would be necessary. Based on the constraints of the project, regarding both the scale of design-implementation and cost, the purchased of such equipment was determined to be inappropriate. Therefore, the sensitivity of the coil impedance needed to be increased to facilitate measurement with less sophisticated equipment.

The decision was made to try "loading" the solenoid with a magnetic core. In the presence of an external applied magnetic field, the magnetic dipoles formed by the material's atomic structure align in the direction of the applied field. With most of the core's magnetic dipoles aligned in the same direction (it is nearly impossible to get every single dipole in alignment), the intensity of the externally applied field is increased by a multiplicative factor of μ (the value of μ is dependent upon the product of the material's relative permeability, μ_r, and the constant permeability of free space, μ_o). The equation which describes this amplification factor indicates that the magnetic flux density, B (in Tesla) is the product of the magnetic field intensity, H (A/m) with the total permeability, μ.

$$\vec{B} = \mu\vec{H}$$

<div align="right">**Equation 3.1**</div>

To validate this design decision, a 3D model of an air-core solenoid and a loaded-core solenoid were created in Maxwell 3D. In each simulation, a 36"x36"x1" aluminum plate was positioned six (6) inches away from the apertures of the simulated solenoids. Both coils were driven by an RMS current of 1 ampere at a frequency of 28 kHz.

The total induced current within the aluminum plate was chosen to be the scalar quantity by which the two coils would be compared. A larger total current corresponds to a stronger magnetic field inducing eddy currents through electromagnetic induction. Figure 3.6 and Figure 3.7 are screen-shots of the two simulations, including the coils and induced current density within the aluminum plates. Note the respective scales of the induced current density for each simulation.
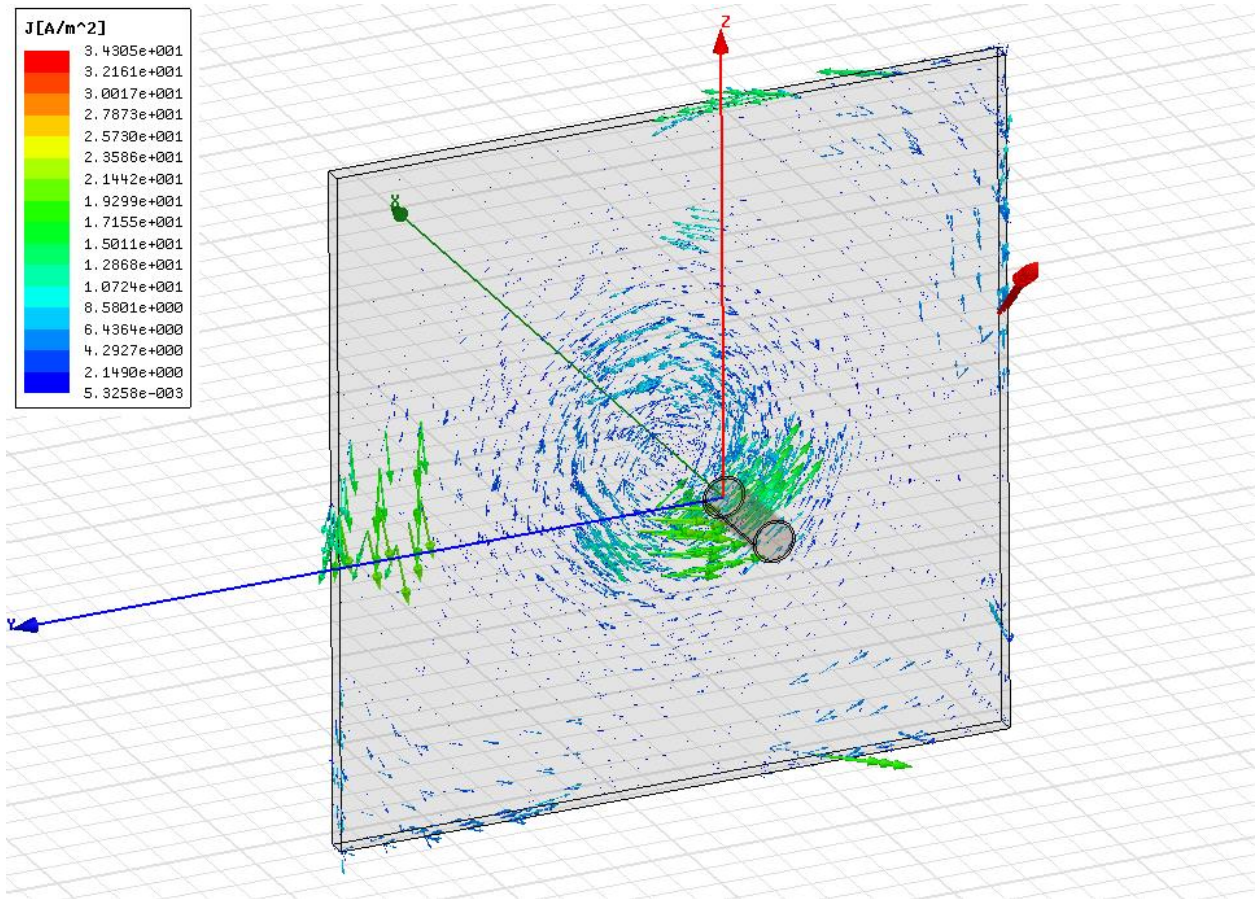
Figure 3.6: Air-Core Solenoid w/ Vector Plot of the Induced Current Density, J (A/m^2)
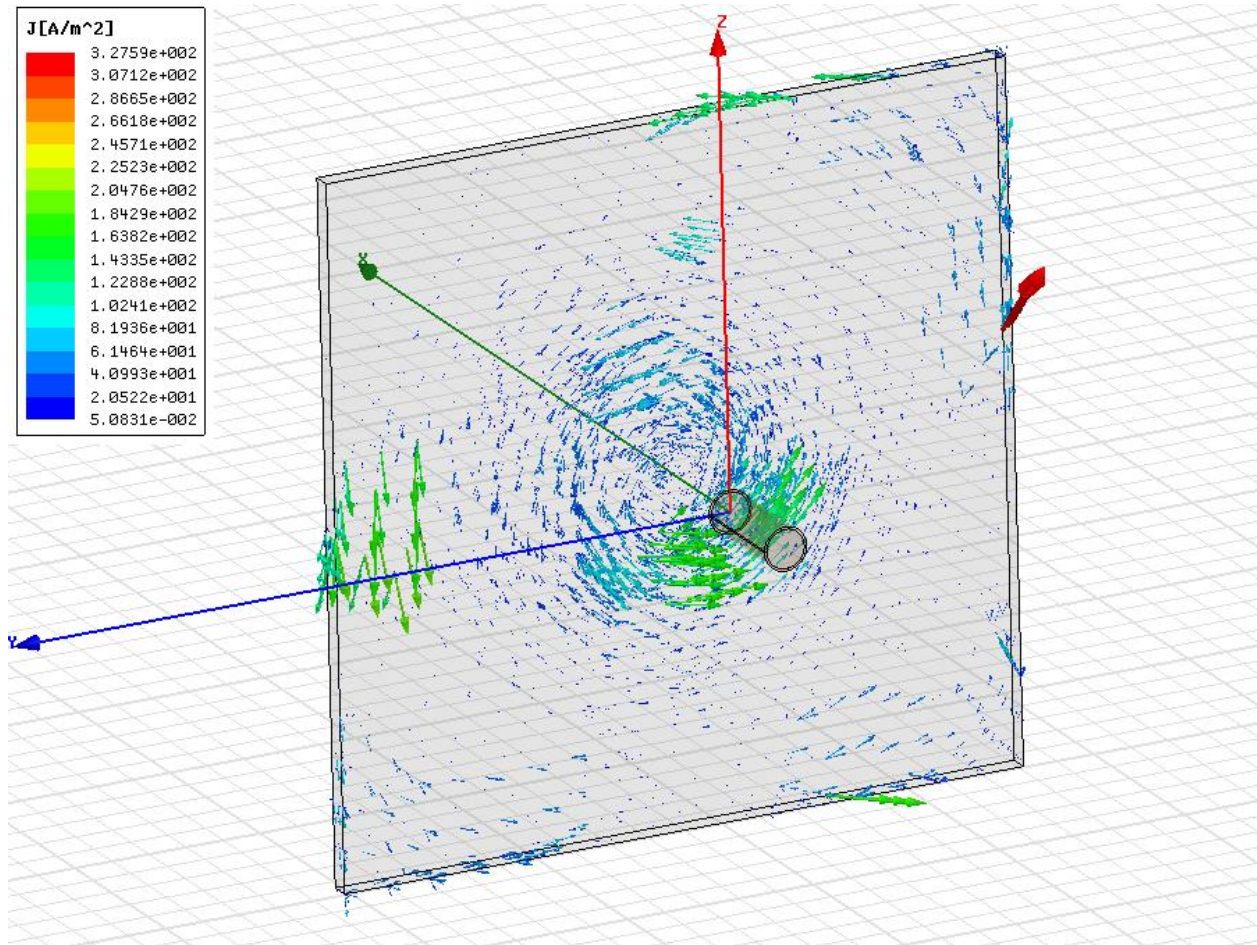
Figure 3.7: Loaded-Core Solenoid w/ Vector Plot of Induced Current Density, J (A/m^2)

The results from these simulations are in Table 3.1. Having integrated the current density over the volume of the aluminum plate, the larger total induced current occurs in the simulation of the loaded-core coil. This indicates that the magnetic field emanating from the loaded-core coil is indeed stronger than the magnetic field from the air-core coil. Therefore, a loaded-core coil will be more sensitive than an air-core coil to the presence of aluminum.

Table 3.1:Total Induced Current; air-core versus loaded-core

Simulation	Air-Core Solenoid	Loaded-Core Solenoid
Induced Current, Real	-1.404e^{-17} A	-1.681e^{-17} A
Induced Current, Imaginary	2.395e^{-21} A	7.832e^{-21} A
Induced Current, Magnitude and Phase	1.405e^{-17} A @ 179.99°	1.681e^{-17} A @ 179.973°

Through simulation, it was realized that the sensitivity of the coil could be increased further by focusing more of the magnetic field in the direction of the aluminum plate. Figure 3.8 and Figure 3.9 are plots of the magnetic field lines for a solenoidal coil and a c-shaped coil, respectively. In the case of the solenoid, we see that the field lines emanate from one end of the coil and loop back to the opposite end. The ends of the coil can be thought of as magnetic poles (north and south). In the solenoidal configuration, the total magnetic energy radiating from the coil is distributed along the path of these field lines. This means that approximately half of the total magnetic energy available at any given time from the solenoid structure is located in the region opposite the aluminum plate. This energy is essentially wasted since it is too far from the aluminum to induce any eddy currents.
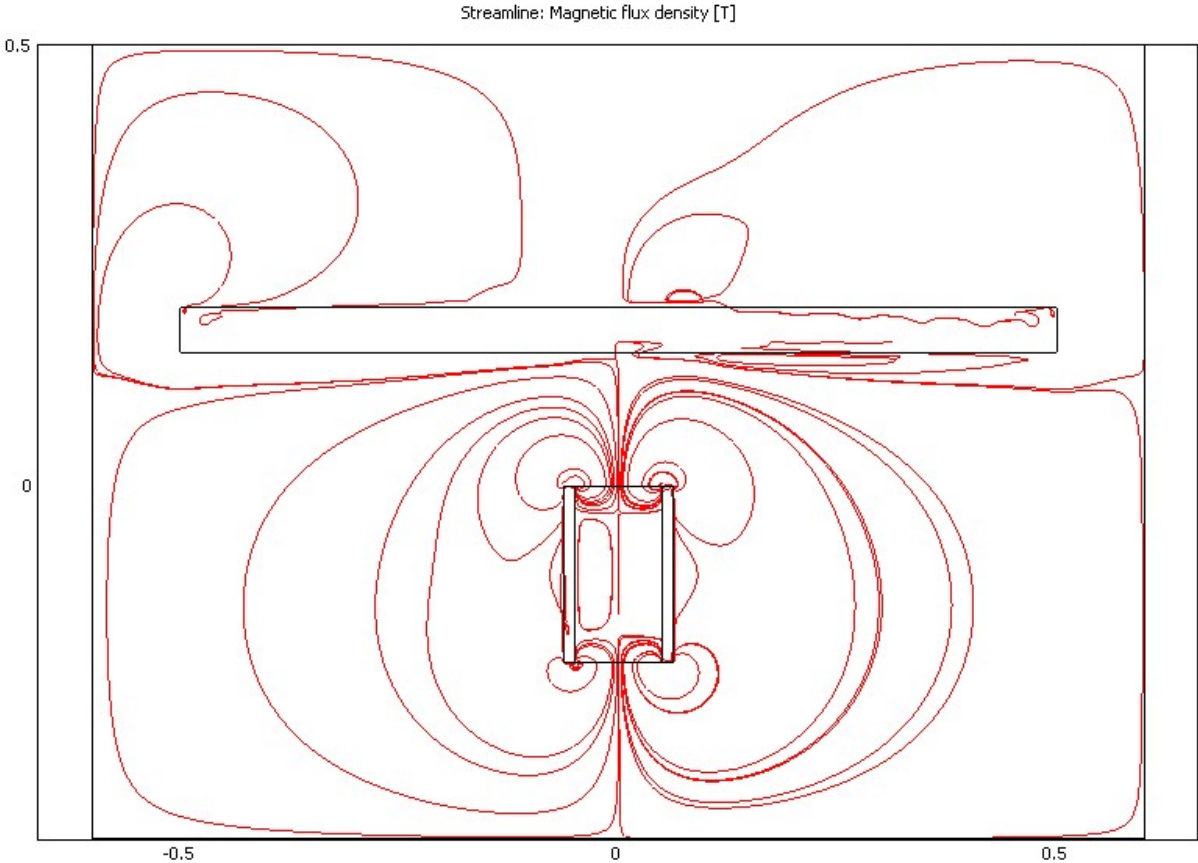
Figure 3.8: Loaded-core solenoid streamline plot of Magnetic Flux Density

Streamline: Magnetic flux density [T]
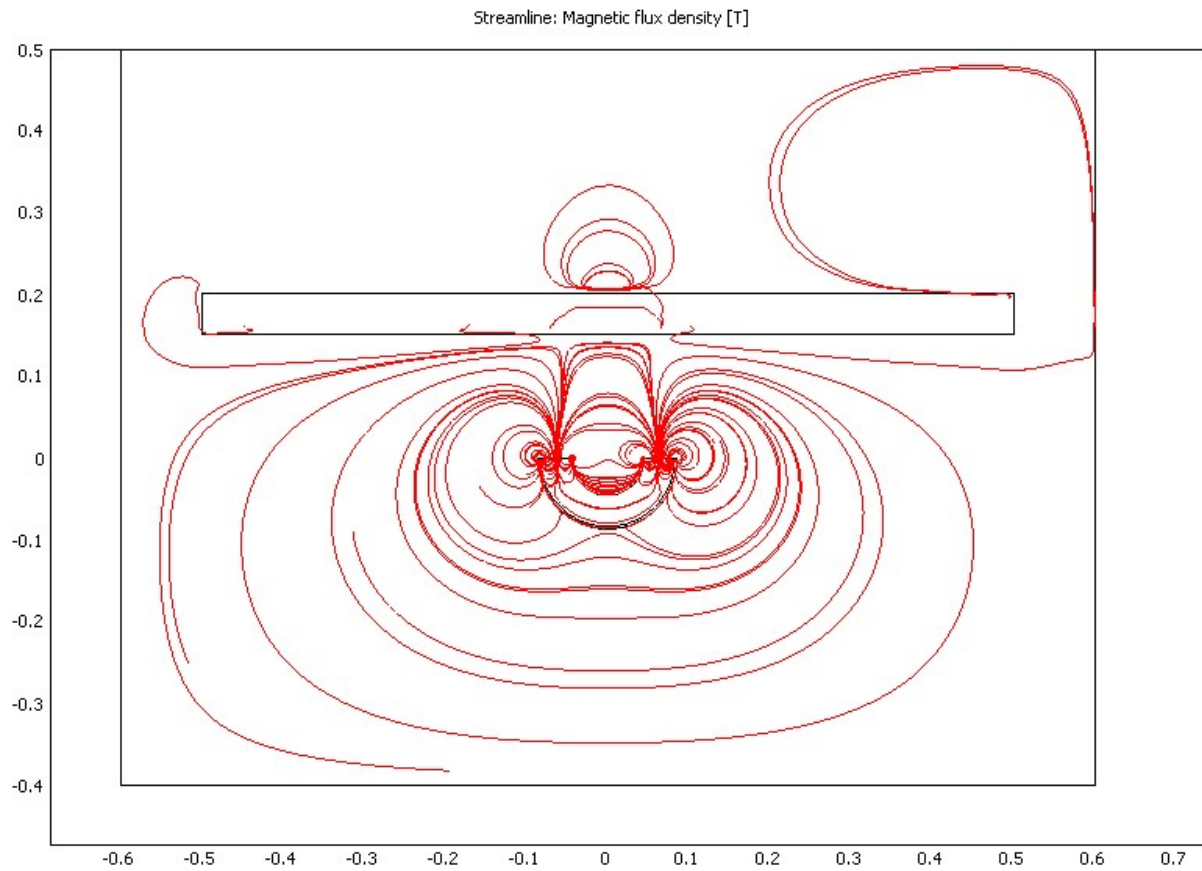
Figure 3.9: Loaded-core c-shaped coil streamline plot of Magnetic Flux Density

The better configuration is the c-shaped design in Figure 3.9. Due to the position of the coil's two poles, the majority of the magnetic energy is focused in the forward region, towards the aluminum plate, creating a much more sensitive response in the coil's impedance.

19
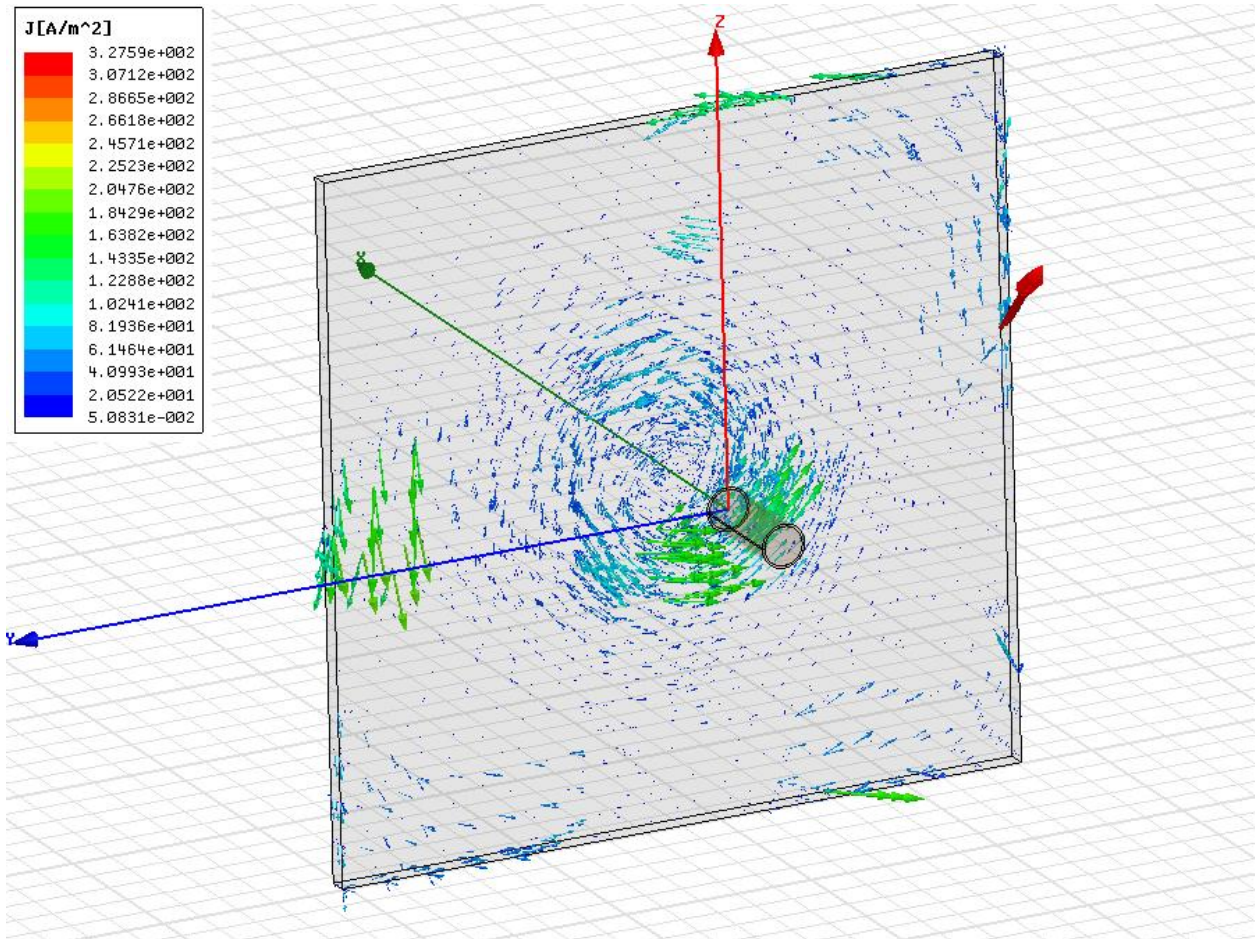
Figure 3.10: Loaded-Core Solenoid w/ Vector Plot of Induced Current Density, J (A/m^2)
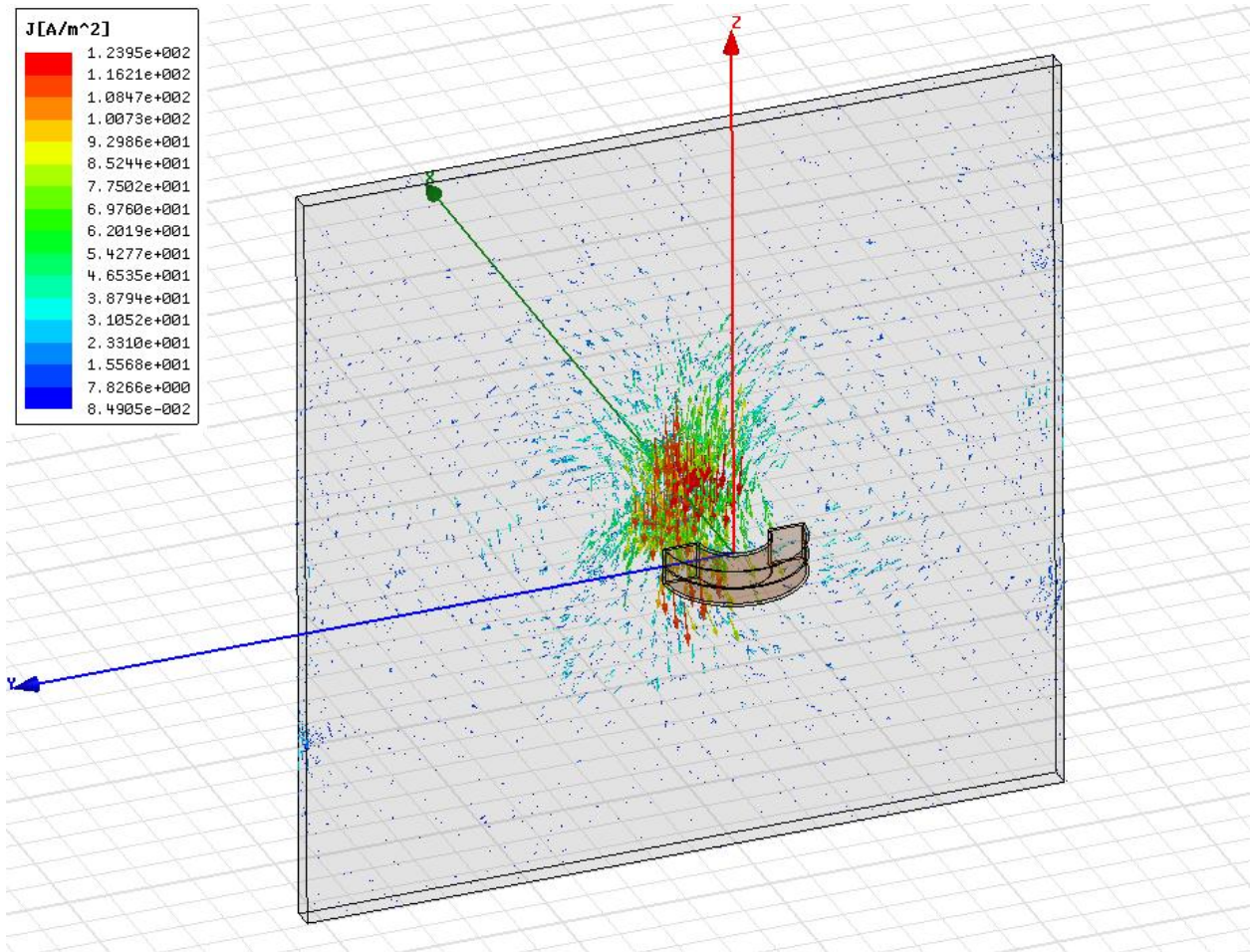
Figure 3.11: C-shaped, loaded-core w/ Vector Plot of Induced Current Density, J (A/m^2)

Once again, simulations were created in Maxwell 3D to compare the total induced current in a 36"x36"x1" aluminum plate due to both a solenoidal coil and a c-shaped coil (both with loaded-cores). Figure 3.10 and Figure 3.11 are screen-shots of these simulation setups and the resulting values of the total induced currents are summarized in Table 3.2. Since the c-shaped coil caused a larger induced current in the aluminum sample, it can be concluded that the c-shaped design is more sensitive that the solenoidal coil design.

Table 3.2:Total Induced Current; loaded solenoid versus loaded c-core

Simulation	Loaded-Core Solenoid	Loaded-Core, C-Shaped Coil
Induced Current, Real	-1.681e^{-17} A	-3.932e^{-17} A
Induced Current, Imaginary	7.832e^{-21} A	-4.754e^{-20} A
Induced Current, Magnitude and Phase	1.681e^{-17} A @ 179.973$^{°}$	3.932e^{-17} A @ -179.931$^{°}$

21

These two sets of simulations support the design decisions to create the c-shaped, ferrite-core electromagnet used in the non-invasive molten metal sensing system. Due to constraints place upon our budget and project timeline, the ferrite-core used in the actual sensor was salvaged from a toroidal core used in a previous project. As a result, we are uncertain as to the actual permeability of the ferrite-core, however, it is reasonable to assume a relative permeability, μ_r, between 500 and 1000.

3.2 Coil Support Structures

Throughout the project, different tests were performed with different versions of the circuit and the coil. In order to maintain a solid testing platform, the coil support structures had to be adapted to the different tests. This section details the design requirements and construction of the two different coil support structures.

3.2.1 Single Coil

The first time the system was tested, only one coil was used. A support structure had to be designed to hold this coil in place while the molten aluminum was being poured into a sand mold. The support structure had to be simple due to design time constraints, but also had to be flexible so that is could be positioned in a variety of positions. Using the limited resources available, a microphone stand was chosen as an idea platform to mount the coil to. Using a screw clamp retrofitted to the end of microphone stand, the coil could be held at different heights and also moved around in a number of other ways. Figure 3.12 shows a close-up of the screw clamp holding the coil. The top of the microphone stand can also be seen in the right side of the photo.

Figure 3.12: Single coil support structure close-up

This coil structure worked out very well during the first test with molten aluminum. Figure 3.13 shows a photo of the coil support structure with the coil next to the sand mold that will be poured. The advantages of using the microphone stand were very clear; the coil could be positioned almost anywhere and the microphone stand provided a mostly stable base.

Figure 3.13: Single coil support structure placed by sand mold

The disadvantages of using this coil support structure was that it was finicky to setup. The joints in the microphone stand had to be tightened using tools instead of just by hand due to the weight of the coil. The microphone stand also was prone to tipping over, a problem we solved by making sure one leg was directly underneath the coil at all times.

This design worked very well for the initial tests, but a more stable platform would need to be designed if this system were to be used repeatedly. Another issue that was pointed out after the tests was the impact of the metallic support structure on the performance of the coil. The coil in this design is held tightly by a metal clamp. The impact of this metal near the coil was something that needed to be looked into further for the future coil support structure.

3.2.2 Tri-Coil

The second and subsequent times the coil system was to be tested, a better coil support structure was needed. This new structure had to have the capability of supporting up to three coils at a time, so that a system with an array of coils could be tested. The coils that needed to be supported would also be different than the first coil support structure. The new coils were designed alongside the coil support structure. As mentioned in section 3.1.5, the coils were encased in epoxy to help provide thermal and movement insulation and also to allow the coils to be supported without metal surrounding the center (as was the case with the original coil support structure). T-nuts were inserted into the epoxy during manufacturing so that a metal plate could be attached to the back of the coil. This metal plate then attached to the coil support structure. Figure 3.14 is a picture of the coil with the metal back plate installed. The t-nuts are encased in the epoxy and bolts are screwed into them to hold the metal plate onto the coil.
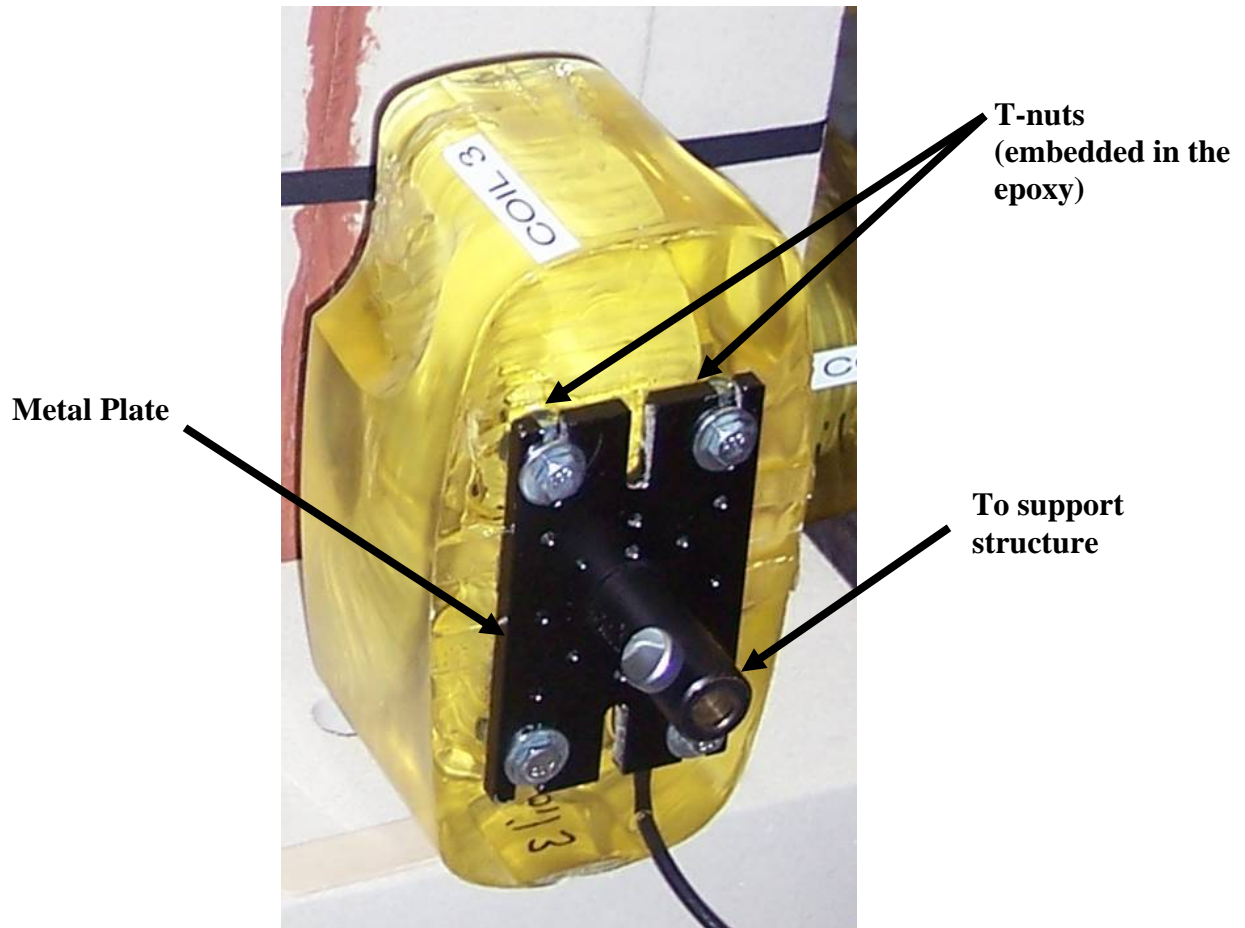
Figure 3.14: Metal plate attached to back of coil

Next a platform had to be designed to support three epoxy encased coils, each weighing close to ten pounds. One of the other design constraints was that the structure needed to allow for flexibility in the placement of the coils. This was solved by mounting the coils on a track so they could be raised and lowered to different heights. Figure 3.15 is an image of the track on the coil support structure which allows each coil to move independently in a vertical line. The white arrows show the axis of movement of the coils.
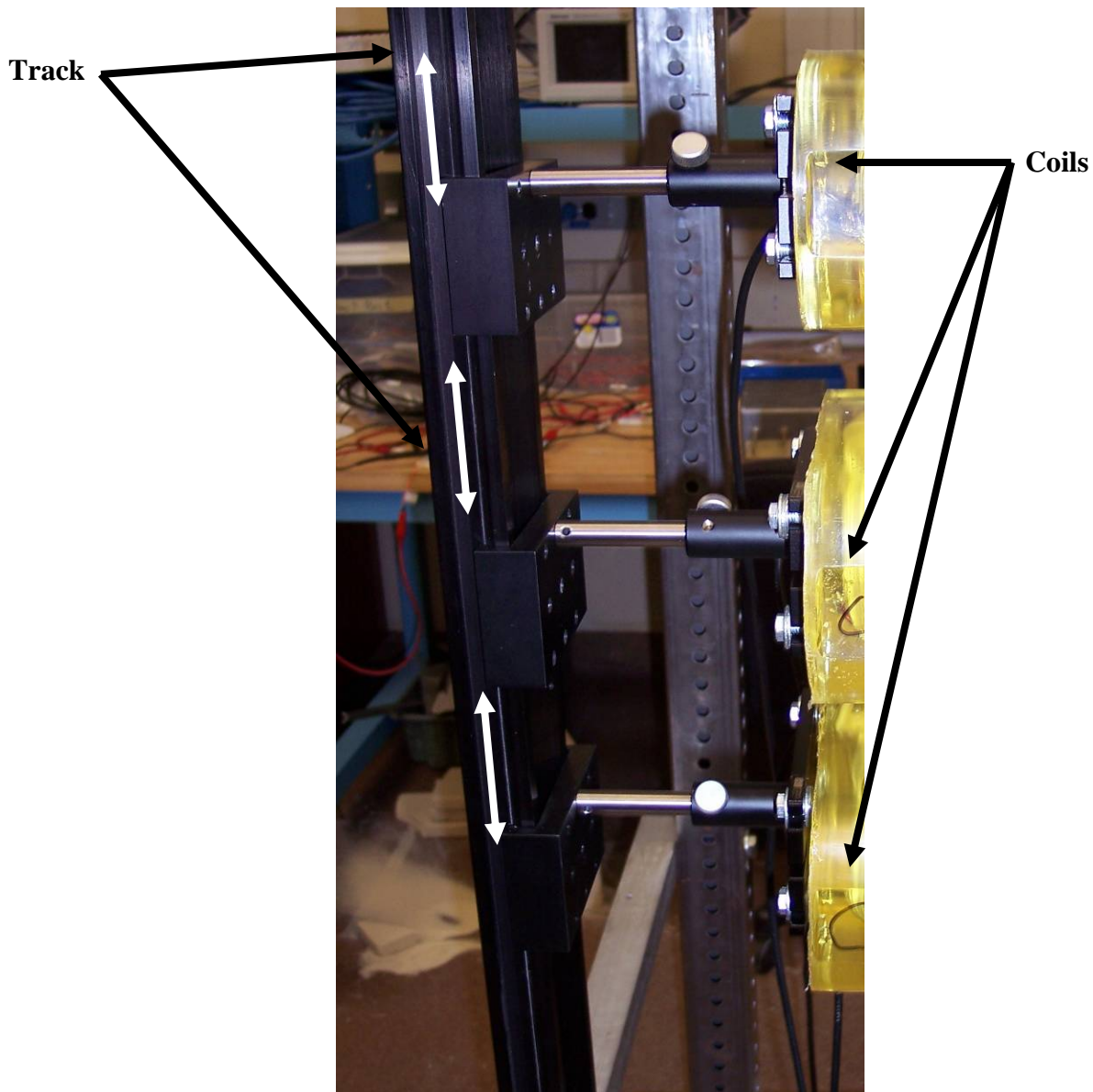
Figure 3.15: Track on coil support structure to allow vertical movement of coils

After a means to give the coils vertical flexibility was designed and constructed, a structure to hold the track was needed. This structure had to be strong, simple, and have the flexibility to be placed in a variety of different ways. Each sand mold that was used for testing was seated in a metal container, sitting atop a wooden pallet. The coil support structure needed to be wide enough to straddle the pallet. Pallets are typically 4ft square, so the coils support structure was designed with a width of 4'2" wide. This would allow placement outside of the pallet. The support structure was constructed from two 4', 2.5" square steel tubing with pre-drilled holes, one 4'7", 1.5" aluminum angle, two 3', 1.5" steel angle, and one 4'7", 2.5"

aluminum angle. Figure 3.16 is the side view of the coil support design and Figure 3.17 is the front view of the coil support design.
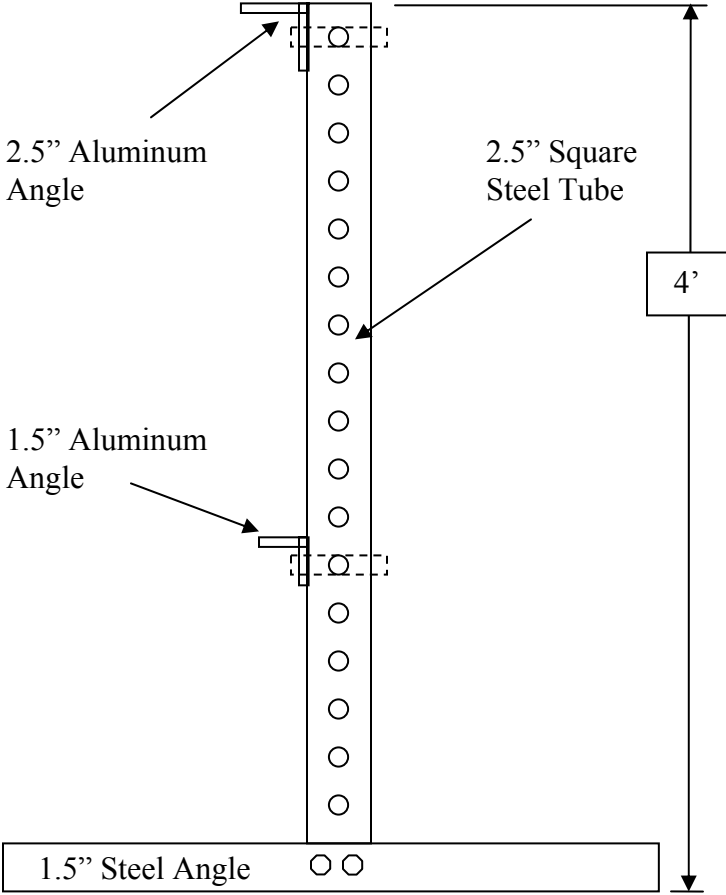
Figure 3.16: Side view of coil support structure drawing
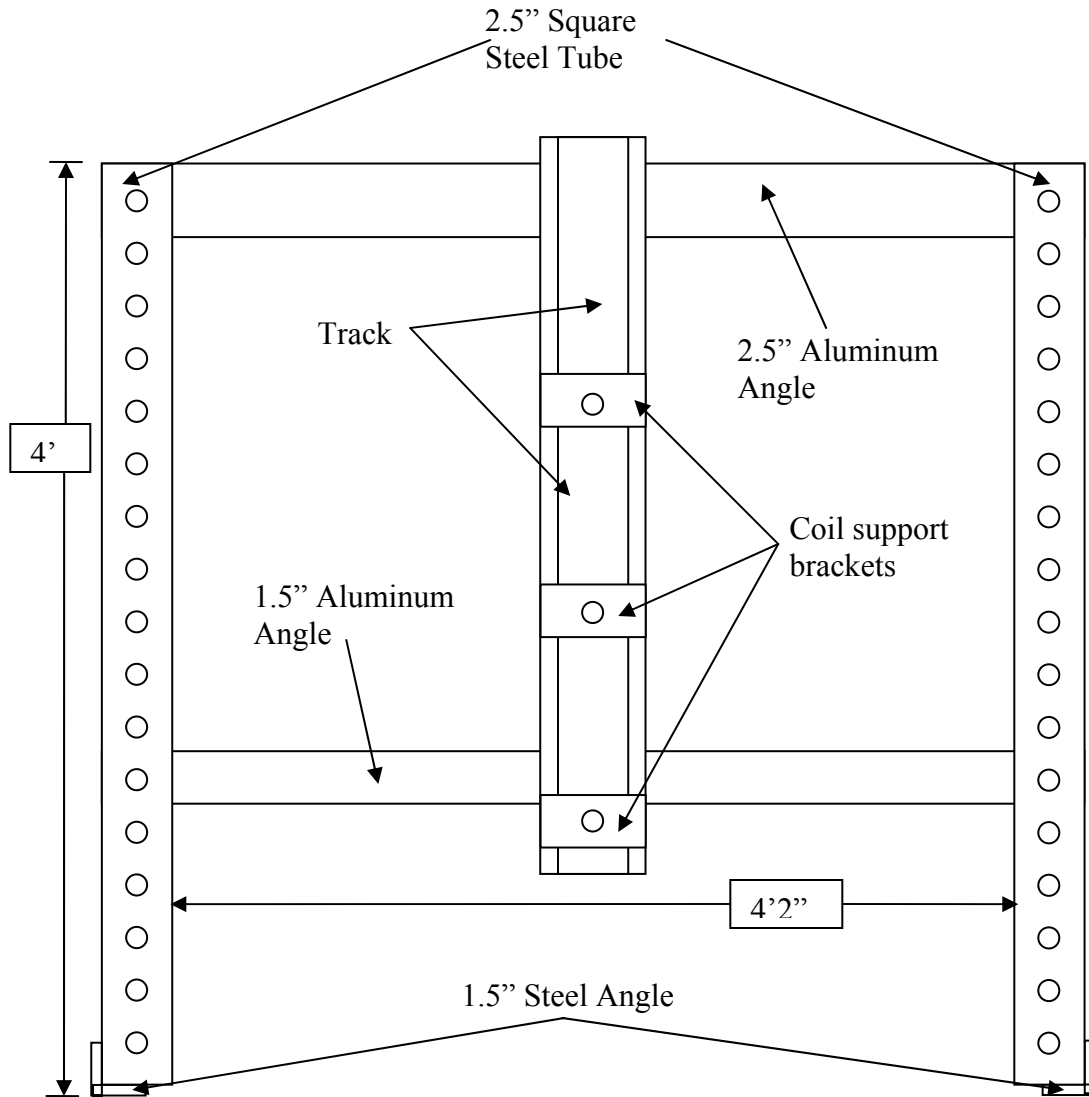
Figure 3.17: Front view of coil support structure drawing

After the coil support structure for three coils had been designed, construction began. The aluminum angle was drilled and bolted in place in addition to the steel angle. Then the track was bolted to the support structure and the coil support brackets were added to the track. Then the coils could be added to complete the testing platform. Figure 3.18 through Figure 3.20 show the completed tri-coil support structure from three different angles.

Figure 3.18: Completed tri-coil support structure - side view
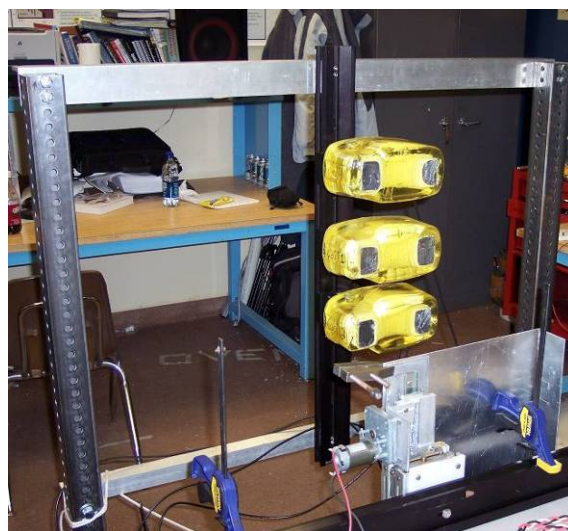
Figure 3.19: Completed tri-coil support structure - front view

Figure 3.20: Completed tri-coil support structure - rear view

The tri-coil support structure design performed very well in the tests. It was a very strong and stable base to hold the coils. It fit perfectly over the pallets, so there were no issues when it was put in place by the sand mold. The flexibility of vertical movement was extremely helpful and allowed a number of different placements of the coils for tests. The design had an added benefit that it wasn't designed for. When the coils were placed alongside the sand molds, sometimes the molds would be tilted. The rod that attached to the coil could be loosened and the coil slid forward, so we could guarantee that there wouldn't be any space between each coil and the sand mold. The only disadvantage to the coil support structure was its size. To move the structure, it had to be disassembled, which fortunately was an easy task due to the design. There were only six bolts that had to be removed and the structure would collapse flat for transport. Figure 3.21 is an image of the structure, complete with coils, during one of the tests. The coils flat against the sand mold, is the ideal placement for them and this design accomplished that goal.

Figure 3.21: Coil support structure in use for a test

3.3 Oscillator Circuit

An oscillator circuit is an electronic circuit which produces a repeating electronic signal, usually being a sinusoidal, square or saw-tooth waveform. There are two main types of oscillator circuits: Harmonic Oscillators and Relaxation Oscillators [9]. Using an inductive coil as a sensor, a RLC oscillator, a type of harmonic oscillator with a sinusoidal output, was created.

A RLC oscillator is an oscillating circuit consisting of a resistor (R), inductor (L), and a capacitor (C). The inductor and capacitor in this type of circuit can be either aligned in series or in parallel for oscillation. Figure 3.22 shows a RLC circuit with the inductor and capacitor in parallel. This parallel RLC circuit, also known as a "tank" circuit, was used as the basis for this project. (It should be noted that this is a simplified circuit model and does not take into consideration losses due to metal entering the field of the inductive coil.)
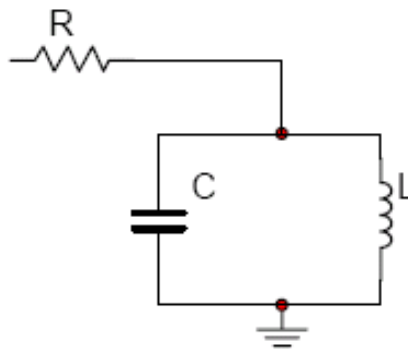
Figure 3.22: RLC Oscillator (Tank Circuit)

In this RLC circuit, electrical current alternates between the inductor and capacitor. As the capacitor discharges, current flows into the inductor creating a voltage which then charges the capacitor allowing it to discharge, repeating the cycle. This repeating exchange of energy is what creates an oscillation.

This tank circuit can be analyzed more closely to understand what is happening mathematically with the inductor and capacitor. The formulas for finding the impedances of an inductor and capacitor are basic knowledge for electronic circuit theory and can be seen in Equation 3.2 and Equation 3.3.

$$Z_L = j\omega L$$

Equation 3.2

$$Z_C = \frac{1}{j\omega C}$$

Equation 3.3

By setting the reactance of the inductor and the reactance of the capacitor equal, knowing that they will have the same angular frequency, we obtain Equation 3.4.

$$\frac{1}{\omega_o C} = \omega_o L$$

Equation 3.4

We can then multiply both sides by ω_o and perform basic algebra to solve for ω_o giving us Equation 3.5.

$$\omega_o = \frac{1}{\sqrt{L \cdot C}}$$

Equation 3.5

Equation 3.5 represents to the resonant angular frequency of this RLC tank circuit. When the reactance of the inductor and the impedance of the capacitor are equal, the total impedance of the circuit at resonance is equal to infinity. This can be found by using the formula for parallel impedances shown in Equation 3.6.

$$Z_{total} = \frac{1}{\dfrac{1}{Z_{P1}} + \dfrac{1}{Z_{P2}}}$$

Equation 3.6

Knowing that the values of the reactances of the inductor and capacitor are the same (denoted by variable x) and substituting this into Equation 3.6 we obtain the following:

$$Z_{total} = \cfrac{1}{\cfrac{1}{j\cfrac{1}{x}} + \cfrac{1}{j \cdot x}} = \cfrac{1}{\cfrac{1}{j} \cdot x + j \cdot x}$$

After simplifying this total impedance we find that at this resonance frequency the impedance of the system goes to infinity (Equation 3.8)

$$Z_{total} = \cfrac{1}{\cfrac{1}{j} \cdot x + j \cdot x} = \cfrac{1}{-j \cdot x + j \cdot x} = \cfrac{1}{0} = \infty$$

By applying a voltage at the input of this RLC circuit we can measure the output voltage to analyze how this system functions. This is shown in Figure 3.23.
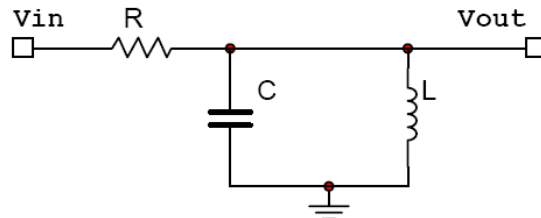
Figure 3.23: RLC - Input and Output Voltages

To simplify this circuit we can combine the impedances of the inductor and capacitor (Figure 3.24).
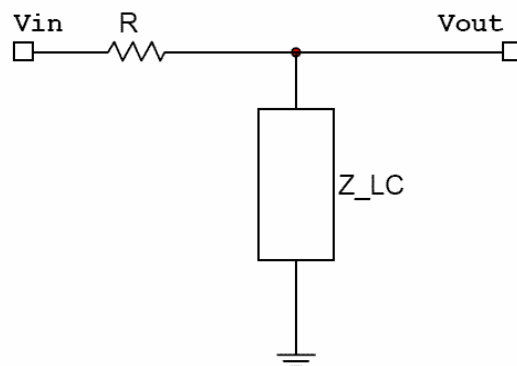
Figure 3.24: RLC – Combined Inductor and Capacitor Impedances

Equation 3.9 expresses the total impedance, Z_{LC}, after combining the individual impedances of L and C connected in parallel.

$$Z_{LC} = \frac{1}{j\omega C + \frac{1}{j\omega L}}$$

This simplified version of the RLC circuit can also be thought of as a voltage divider. We can substitute R and Z_{LC} into the basic voltage divider equation:

$$Vout = \frac{Z_{LC}}{Z_{LC} + R} \cdot Vin$$

We can now relate the output voltage (Vout) as a function of the input voltage (Vin).

$$\frac{Vout}{Vin} = \frac{Z_{LC}}{Z_{LC} + R}$$

By substituting Equation 3.9 into Equation 3.11 and performing basic algebra we obtain the following transfer function for this circuit:

$$H(j\omega) = \frac{Vout}{Vin} = \frac{1}{1 + R\left(j\omega C + \frac{1}{j\omega L}\right)}$$

Using MATLAB we can plot the magnitude response and the phase response of the transfer function found in Equation 3.12. The MATLAB script can be found in Appendix A. Figure 3.25 shows the magnitude and phase response of the RLC circuit with values for R, L,

and C being 1 kΩ, 1.648 mH, and 0.02 μF respectively. These values were chosen because this inductance value is the inductance of the c-core coil used in this project. The capacitor and resistor values were chosen arbitrarily when designing the oscillator described in Section 3.2.1.
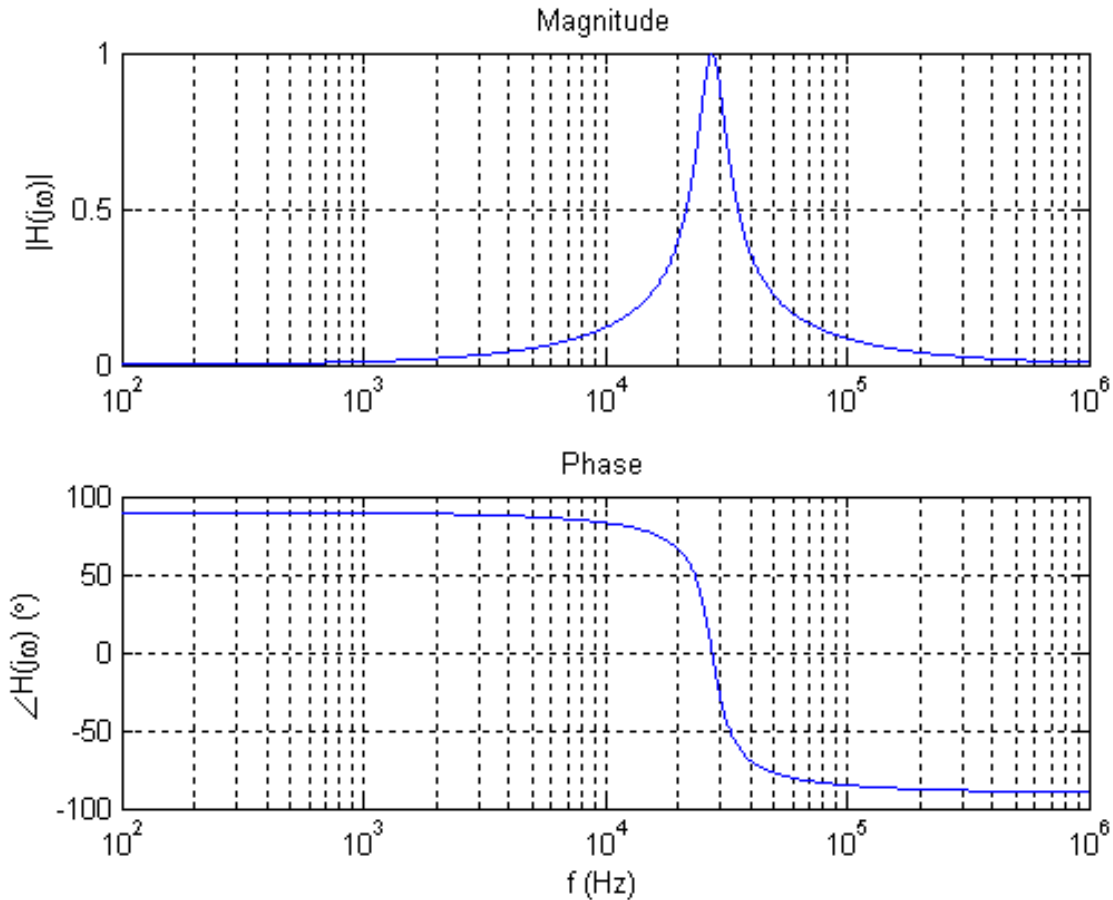
Figure 3.25: Magnitude and Phase Response of RLC Transfer Function

From the plots shown in Figure 3.25 it can be seen that at the resonant frequency the magnitude of *H(jω)* is equal to 1 and there is a 180° phase shift. By substituting these L and C values into Equation 3.5 we find that we achieve a resonant linear frequency of about 28 kHz. This resonant frequency matches that shown in the magnitude and phase plots.

With the information gathered from these plots and equations it can be observed that this circuit is most sensitive at its resonant frequency. This is the basis for using the c-core coil as an inductor in a RLC circuit. By using the coil in resonance we would be able to monitor molten aluminum with optimal sensitivity.

Finally for this RLC circuit to oscillate, it must be driven by a source. This could be accomplished using an op-amp with a feedback loop to provide gain to the RLC circuit. Ideally

a gain of 1 would be sufficient for continuous oscillation, but with non-ideal, real components with loses, this is not true. A gain slightly larger than 1 is required to overcome these loses and more loses introduced by metal entering the electromagnetic field of the coil. The following sections describe the circuits implemented with the RLC circuit.

3.3.1 Preliminary Test Circuit

The goal of the original test circuit was to provide the RLC circuit, previously discussed in Section 3.2, with a feedback loop driving it into oscillation. Not knowing the exact gain needed for oscillation, due to losses in the coil, created the need for a source of variable gain in the feedback loop. Figure 3.26 shows the circuit schematic for this original testing circuit.
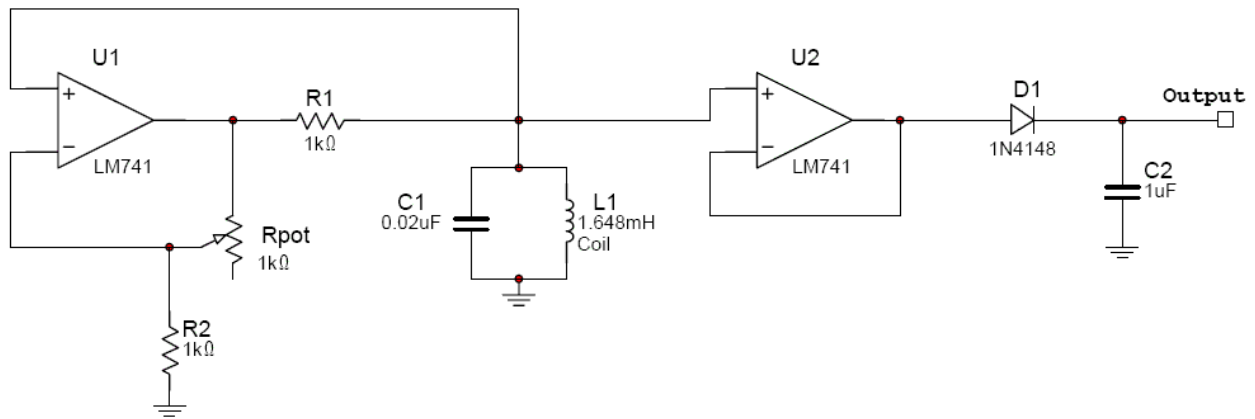
Figure 3.26: Preliminary Test Circuit Schematic

The first stage of this circuit is a RLC circuit connected to an LM741 op-amp (U1) oriented with a negative feedback gain. This gain was made variable by inserting a 1 kΩ potentiometer to connect the op-amp output to its inverting input. The gain of this feedback loop can be expressed by Equation 3.13.

$$Gain = 1 + \frac{R_{pot}}{R_2}$$

Equation 3.13

By substituting the values of R1 (1 kΩ) and R_{pot} into eq(1) we observe a range of gain from about 1 to 2. This potentiometer allowed for a quick gain adjustment, but not very repeatable results with a not so precise adjustment.

36

The second op-amp (U2) in this circuit was used in a voltage follower configuration acting as a buffer for the circuit. This prevented any issues of loading down the oscillator when attempting to monitor the circuit. The oscillation waveform was then rectified using a half-wave rectifier created with the 1N4148 diode. Finally, a capacitor (C2) was used to create a DC value output to be measured.

3.3.2 Automatic Gain Control (AGC)

The idea of modifying the original circuit and creating an automatic gain control circuit was introduced to help eliminate the physical gain adjustment and allow calibrated, repeatable measurements. The entire schematic for the AGC circuit is shown in Figure 3.27. These next sections break up the entire schematic into smaller pieces explaining how they together complete the automatic gain control circuit. Data sheets for the LM741, TL081, and CD4007 can be seen in Appendix H.
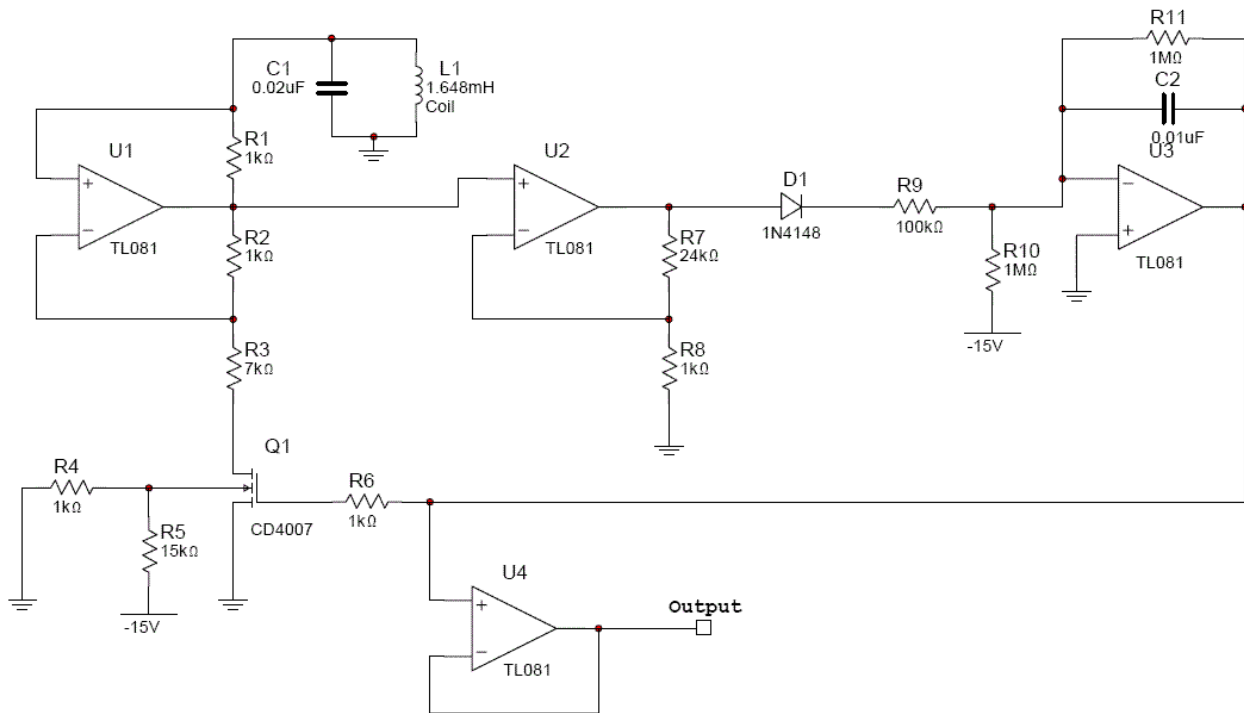
Figure 3.27: Automatic Gain Control Circuit Schematic

3.3.2.1 Stage 1: Oscillator with Variable Gain

The first part of the automatic gain control circuit that was designed was the oscillator with variable gain. The RLC tank circuit described in Section 3.2 was the core of the oscillator

just as in the original testing circuit. This oscillator also needed to be driven by a feedback loop with variable gain to compensate for losses due to metal entering into the field of the coil. The idea was to remove any physical changes to the system for adjusting gain and have it instead be "automatic".

Using the design of the oscillator and variable gain from the original test circuit, the RLC circuit was driven with an op-amp with negative feedback. Some alterations were introduced to the system though to create a voltage adjusted gain. Figure 3.28 shows this improved circuit with a voltage controlled gain.
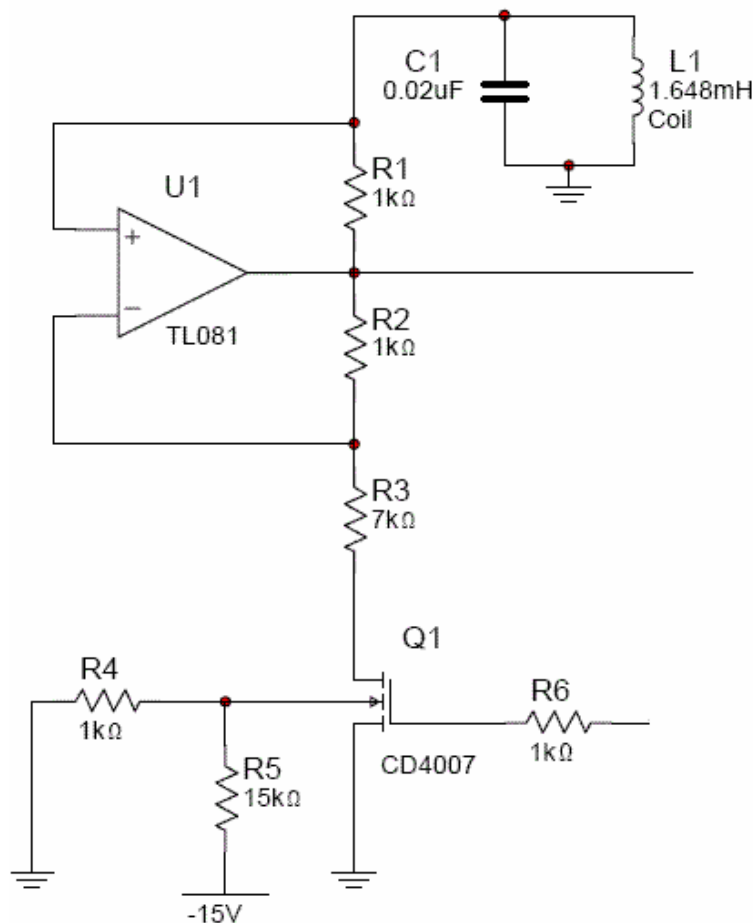
Figure 3.28: AGC – Oscillator with Variable Gain

There are very distinct changes in the automatic gain control circuit compared to that of the original test circuit. The first change introduced to the system was the op-amps chosen for the AGC. The LM741 op-amps were replaced by TL081 op-amps. It was realized with an oscilloscope that the original LM741 selection was operating very close to the 0.5 V/μs slew rate threshold. To resolve this issue the TL081 op-amp with a slew rate of 13 V/μs was chosen.

The second change to the circuit was controlling the gain of the feedback loop of the TL081 op-amp. The N-Channel CD4007 MOSFET replaced the potentiometer to create a new form of variable gain. A MOSFET can be used as a voltage controlled resistor when operating in the triode region by adjusting the voltage from the gate of the MOSFET to the source of the MOSFET (V_{GS}). The change in resistance is found across the drain to the source of the MOSFET (R_{DS}). The CD4007's resistance range was characterized by sweeping the voltage V_{GS} with a power supply and measuring R_{DS} with an ohmmeter. A plot of these measurements can be seen in Figure 3.29.
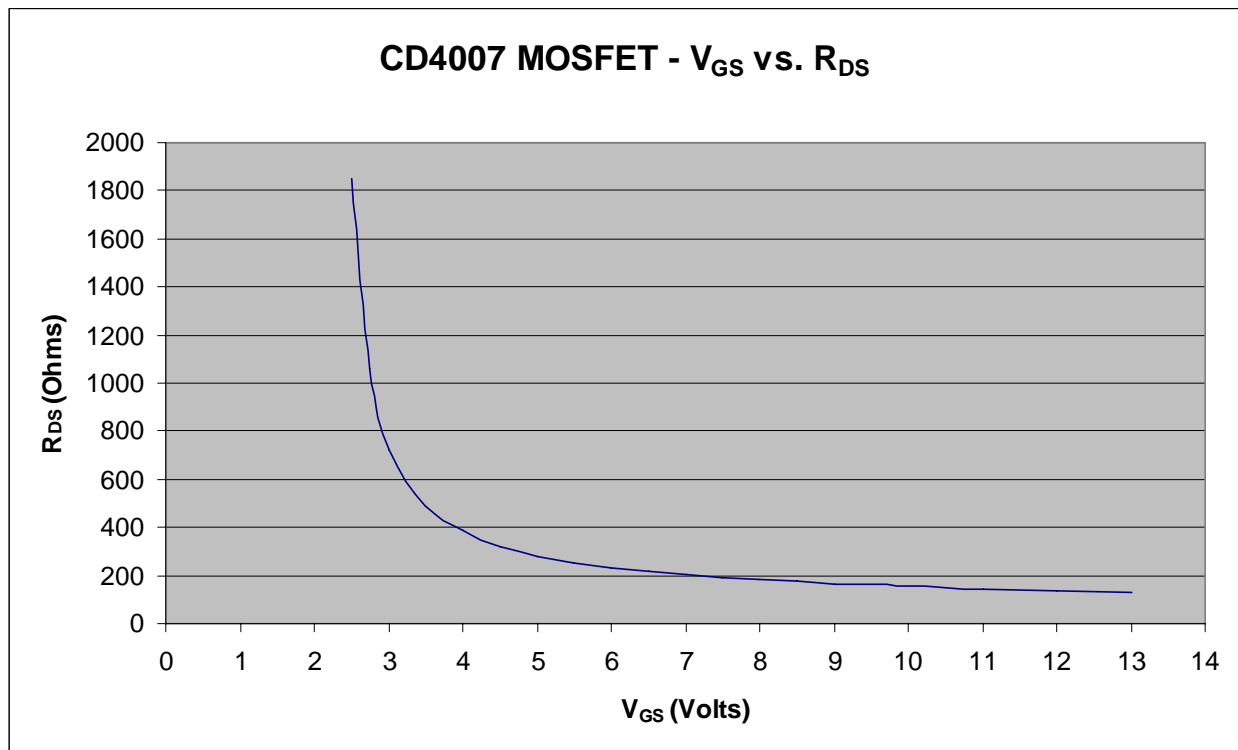
Figure 3.29: CD4007 MOSFET Characterized - V_{GS} vs. R_{DS}

The CD4007 was implemented in the circuit as show in Figure 3.28. Although the MOSFET replaced the potentiometer from the original circuit it, it was not possible to keep this in the same location. The MOSFET required the source to be directly connected to stable ground (0V) in order for the V_{GS} - R_{DS} relationship to function correctly. The constant resistance and variable resistance positions were swapped from that of the original circuit creating this new configuration. The MOSFET also required the body terminal to be connected a specific voltage to prevent the body to drain p-n junction from acting like a diode turning "off" and "on". Resistors R_4 and R_5 set this body voltage to a constant -1V. This prevented the p-n junction from

turning "off" and "on" because no voltage at the drain would be more negative than the -1V at the body.

With this new circuit setup a new expression representing the gain of the system was derived and is shown in Equation 3.14.

$$Gain = 1 + \frac{R_2}{R_3 + R_{DS}}$$

Equation 3.14

Because the gain of the circuit is dependent upon the resistance R_{DS} and R_{DS} is a function of the voltage V_{GS}, it is understood why this system was considered to have a voltage controlled gain. By connecting the gate of the CD4007 to a feedback loop, the gain would be automatically adjusted.

Knowing the gain expression from Equation 3.14 the resistance values for R_2, R_3, and R_{DS} needed to be chosen. The potentiometer of the original testing circuit was measured when oscillation occurred. From this measurement it was found that a gain of about 1.14 was required to keep the circuit in oscillation (without metal in the field of the coil). Figure 3.29 was then analyzed to select a voltage V_{GS} and its corresponding resistance $R_{DS.}$ R_2 and R_3 could be arbitrarily chosen so long as fulfilling the requirement of a gain of 1.14. A spreadsheet was used to create a list of values for these two resistances that would satisfy the required gain using Equation 3.14and also be able to provide enough gain to compensate for loss due to the coil. The values chosen for R_2 and R_3 were 1 kΩ and 7 kΩ respectively.

This first piece of the automatic gain control circuit was breadboarded and tested using a variable power supply. This was used to emulate the feedback loop voltage controlling the CD4007 MOSFET. These tests proved successful and the voltage controlled gain worked. The output oscillation amplitude increased with an increase in voltage V_{GS} and the amplitude decreased by reducing V_{GS}. By eliminating slew rate issues and removing the manually adjusted potentiometer, stage one was completed successfully.

3.3.2.2 Stage 2: Amplification and Rectification

The goal of the second stage of the automatic gain control circuit was to provide gain to the oscillation created from stage one and to also rectify the signal. This second stage schematic can be seen in Figure 3.30.
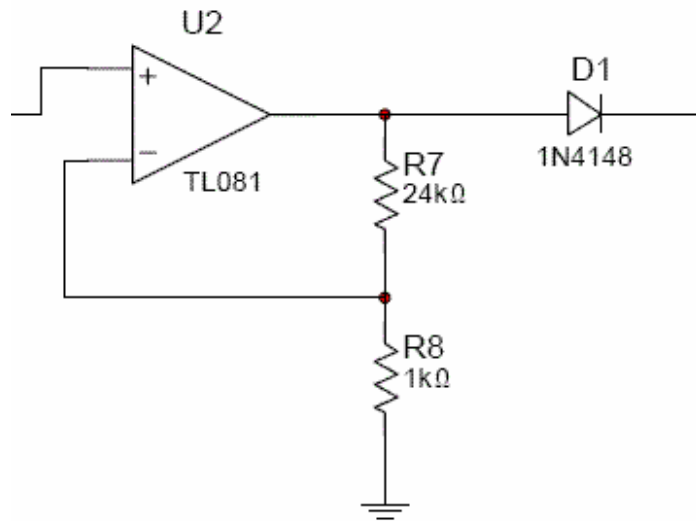
Figure 3.30: AGC – Amplification and Rectification

The amplification portion of this circuit used a TL081 op-amp. The input of the non-inverting terminal of op-amp U2 was the output oscillation from stage one. Op-amp U2 was setup in a non-inverting gain configuration. The gain expression describing this piece of the circuit is shown in Equation 3.15.

$$Gain = 1 + \frac{R_7}{R_8}$$

<div align="right">**Equation 3.15**</div>

By substituting the values of R_7 and R_8 into Equation 3.15 we get a gain of 25. This gain was designed to provide a peak waveform amplitude of 5V at the output of the op-amp. Not only did this op-amp provide gain to the waveform, it also acted as buffer preventing the oscillator in stage one from being loaded down.

The rectification portion of this circuit consisted of a 1N4148 diode. This diode essentially removed the negative portion of the signal resulting in a half-wave rectified signal. It also created a 0.7V drop across the diode bringing the peak of the waveform to approximately 4.3V.

3.3.2.3   Stage 3: Integration

The third stage of the automatic gain circuit consisted of an integrator circuit, which can be seen in Figure 3.31. The idea of the integrator was to sum an offset of the amplitude of the oscillation waveform due to of a lack of needed gain, such as when metal entered the coil's field of view. This integrated signal would then set the gate to source (V_{GS}) voltage of the MOSFET, thus controlling the resistance of the MOSFET and changing the gain of the original oscillator. This final step would complete the feedback loop of the circuit.
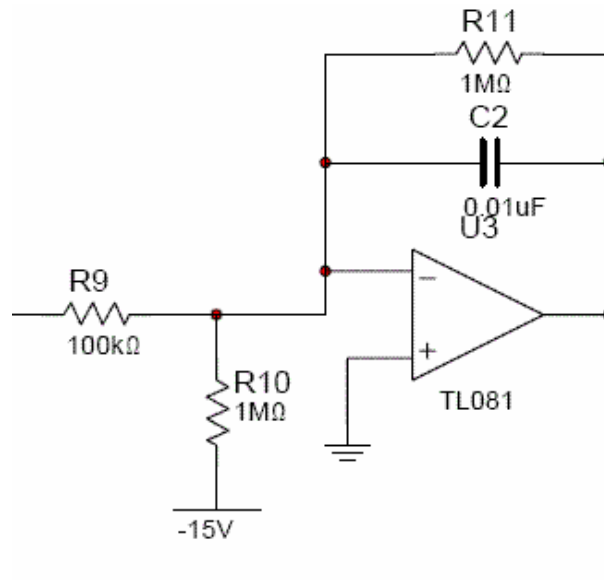
Figure 3.31: AGC - Integrator

The integrator was also accomplished using a TL081 op-amp (U_3). The TL081 was used in an integrator setup with a 0.01μF capacitor with a 1 MΩ resistor in parallel, connecting the inverting op-amp input to the output of the op-amp. The non-inverting input was connected to ground.

A 1 MΩ resistor (R_{10}) connected to the non-inverting input of the op-amp to the -15V rail. This constantly drew 15μA of current to the -15V rail. The 1 MΩ resistor controlled the process of integration because when the current flowing through R_{10} was equal to the current flowing through R_9 integration would cease. The current flowing through the resistor R_9 can be described as the average voltage of the rectified signal divided by the resistance R_9.

From basic calculus we know that the average value of a function is found by Equation 3.16.

$$Avg = \frac{1}{b-a} \int_a^b f(x)dx$$

<div align="right">**Equation 3.16**</div>

We can then substitute a sine wave into Equation 3.16 and integrate from 0 to π.

$$Avg = \frac{1}{(\pi - 0)} \int_0^\pi \sin(x)dx = \frac{2}{\pi}$$

<div align="right">**Equation 3.17**</div>

Solving this equation gives us the average value for half of a period of a sine wave. Because the sine wave was rectified in this circuit and the second half of the period had a constant value of 0, we must divided Equation 3.17 by 2 to compensate for this.

$$\frac{2}{\pi} \cdot \frac{1}{2} = \frac{1}{\pi} = 0.318$$

<div align="right">**Equation 3.18**</div>

This tells us that the average voltage of the rectified signal is equal to about 0.318 ($1/\pi$) times the peak voltage of the amplitude. In the case of this system, having about a 5V peak signal at the output of op-amp U_2 and a voltage drop across diode (D_1) multiplied by 0.318 gives a current flow of about 15µA, stopping the integration process. If the amplitude of the waveform were to drop, the current flowing through resistor R_9 would decrease and the integrator would start integrating this change. The output of this integrator would then supply this voltage change to the CD4007 MOSFET. This would control the gain and keep the waveform at a constant amplitude. This output would also be the monitored "error" signal to which analysis of the system would be based.

3.3.2.4 Output: Buffer

The final piece of the automatic gain control circuit allowed the output signal to be able to be monitored without disrupting the system. This output was tapped off of the output of the

integrator. A buffer was constructed using the voltage follower configuration with another TL081 op-amp. Figure 3.32 shows a schematic of the output buffer circuit.
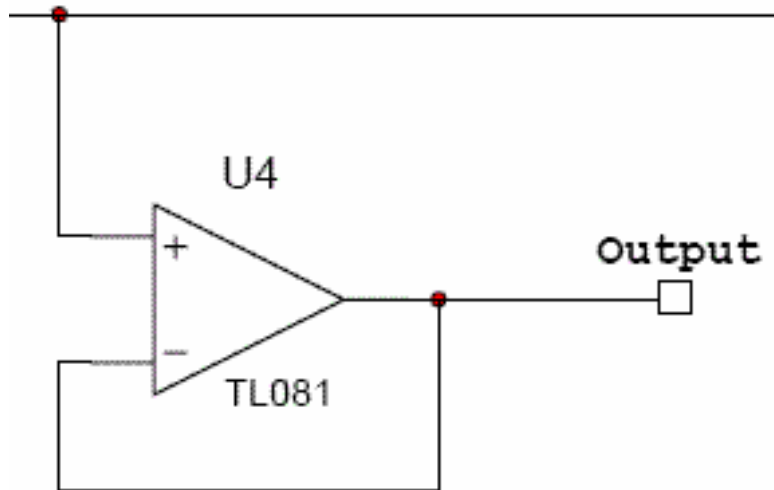
Figure 3.32: AGC - Output Buffer

This output was the "error" signal created by the control loop. The data in determining an increase in gain needed for metal entering the coil's field was found in this signal. This output was a varying DC value measured between 3V and 4V by a data acquisition system.

3.3.3 Circuit Packaging

In order to protect the circuitry, improve reliability, and increase the ease of connectivity, each circuit was soldered and packaged. Creating a packaged circuit was beneficial in creating a professional looking system.

3.3.3.1 Single Oscillator

The first version of the circuit had only one oscillator. This oscillator circuit was soldered onto a 2" by 4" circuit board to provide increased stability and reliability. After soldering, the circuit board was mounted inside of a black plastic 2.5" high, 3" wide, by 6" long project box on four standoffs. The box had three BNC connectors and 1 female XLR connector. The three BNC connectors were used to connect the circuit to the coil, the circuit to the Oscilloscope for monitoring, and a varying DC output that was read by LabVIEW. The XLR connector supplied ±15volts and ground, to provide power for the circuit. Figure 3.33 is an image of the partially

44

completed packaged circuit. The circuit board has been mounted and three out of four connectors are already mounted.
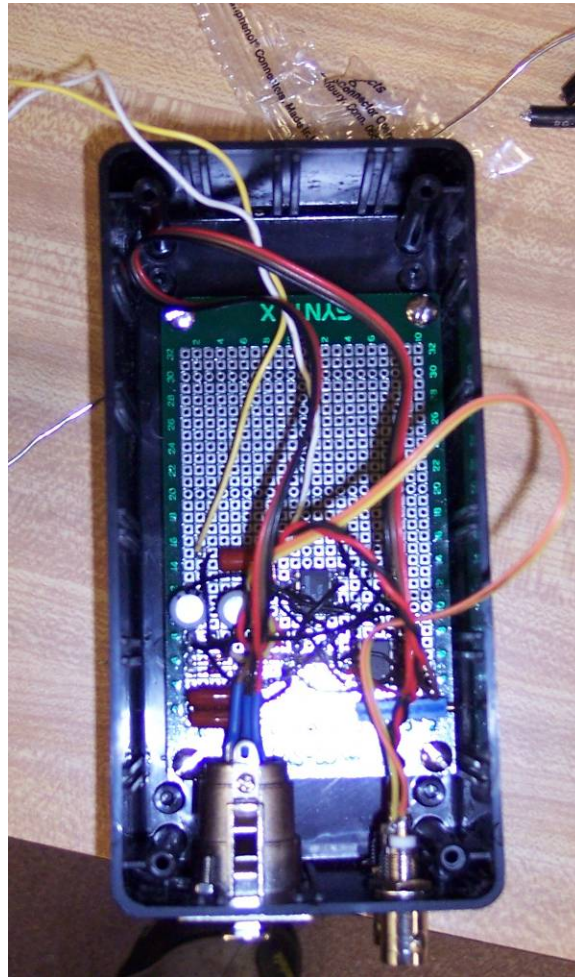
Figure 3.33: Partially completed single oscillator package

The packaging for the single oscillator worked out very well for testing. The BNC connectors allowed for a quick setup and take-down, in addition to very solid connections. The XLR connector for power, coupled with banana plugs, worked very well for supplying power to the circuit. During the numerous tests, there was never a problem with the operation of the packaged circuitry.

3.3.3.2 Three Oscillators

For the second test, three oscillator circuits were needed. It was decided to package these oscillators in the same fashion as the first oscillator. The components for each oscillator were soldered onto one 3" by 5" circuit board as seen in Figure 3.34.
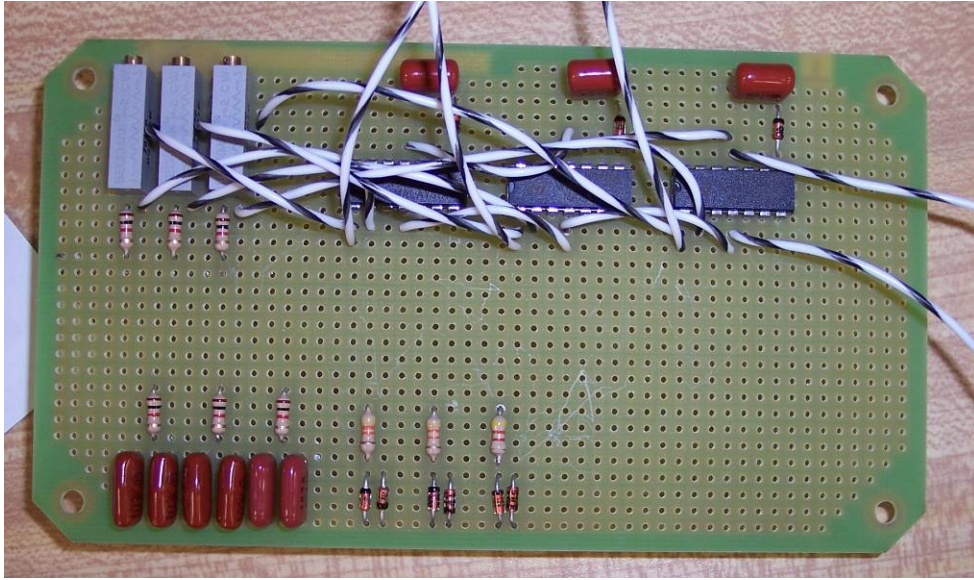
Figure 3.34: Three oscillator circuit board

The board was mounted on standoffs inside of a 5" by 7" metal project enclosure. A metal enclosure was chosen to help maintain a constant ground between all the BNC connectors and also provide a small amount of electrical shielding to the circuit. Figure 3.35 shows the completed circuit board mounted inside the metal enclosure.
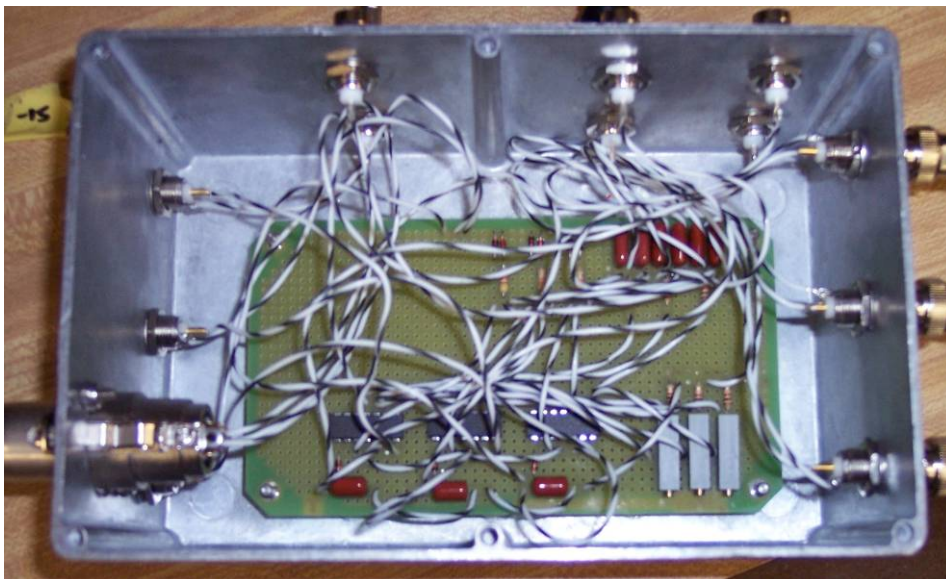
Figure 3.35: Circuit board inside metal enclosure

Due to having three oscillator circuits inside, a large number of BNC connecters were used. Three of the BNC connectors were for the coils, three for circuit calibration, three for LabView to monitor, and an additional three that were used to connect to a second group's data collection MQP. A XLR connector powered the circuits, similar to the enclosure for test 1. Figure 3.36 shows the completed package with all 13 outputs.
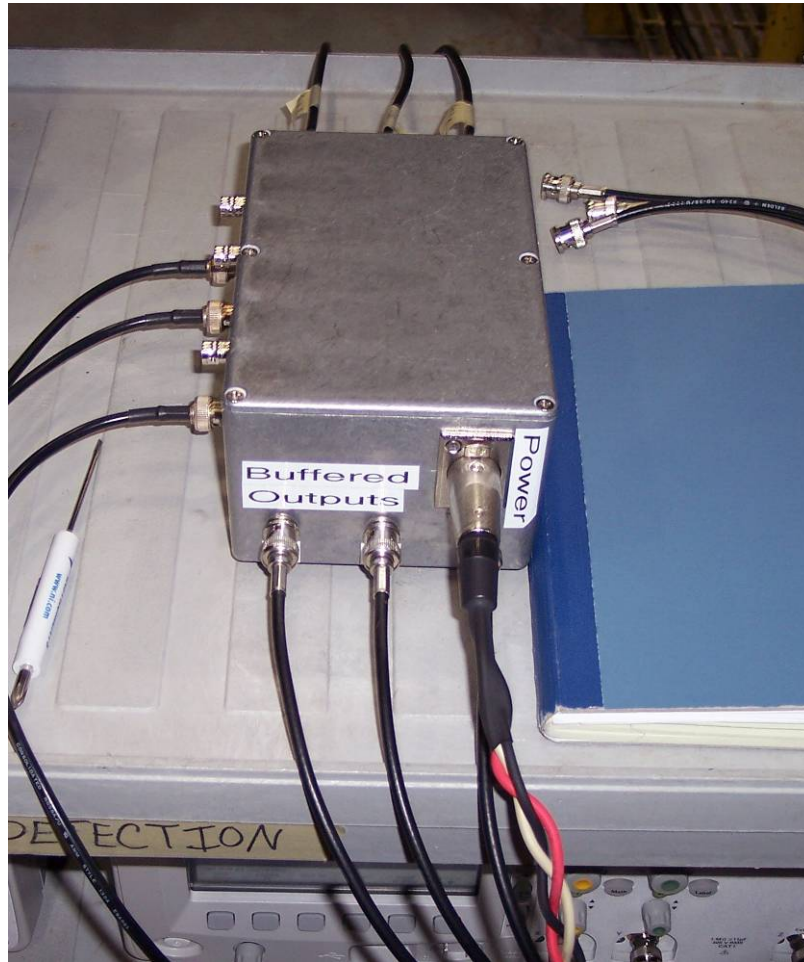
Figure 3.36: Completed three coil oscillator circuit package

The packaging for the three oscillator circuits worked out very well for testing. The BNC connectors again allowed for a quick setup and take-down, in addition to very solid, shielded connections. The XLR connector for power, coupled with banana plugs worked very well for supplying power to the circuit. During the numerous second rounds of tests, there was never a problem with the operation of the packaged circuitry.

3.3.3.3   Single Oscillator with AGC

The design of the packaging for the single AGC circuit was very similar to the previous packaged circuitry. The circuit would be mounted inside, with one BNC for the coil, one BNC to hook up an oscilloscope for testing and calibration, and another BNC to output the error signal to the Data Acquisition system. There would also be another XLR connector to power the circuit. Unfortunately, due to complications and time constraints, the AGC circuit was not packaged and was left on a breadboard. This turned out to be fine because the circuitry could be modified very easily for future modification done by MCT.

3.4 Data Acquisition

Two data acquisition (DAQ) systems were developed for this project.   Both systems were designed to sample and store the value of a DC voltage signal with respect to time and each system encompassed certain characteristics that were appropriate for specific stages in the molten aluminum testing.

3.4.1 LabView VI

The first system was composed of a software interface created using LabView 8.0 and the Agilent MSO6012A mixed signal oscilloscope as the analog-to-digital (A/D) signal conversion hardware. A customized set of instructions encompassing both hardware channel configuration and sampling protocol was created in the LabView development environment. These instructions constitute what LabView calls a Virtual Instrument (VI). The block-diagram for a single-oscilloscope VI setup can be referenced in Figure 3.37. A two-scope VI was also created for another molten aluminum experiment with multiple sensors and was essentially identical to the single-scope configuration. Therefore, the following description pertains specifically to the single-scope VI.
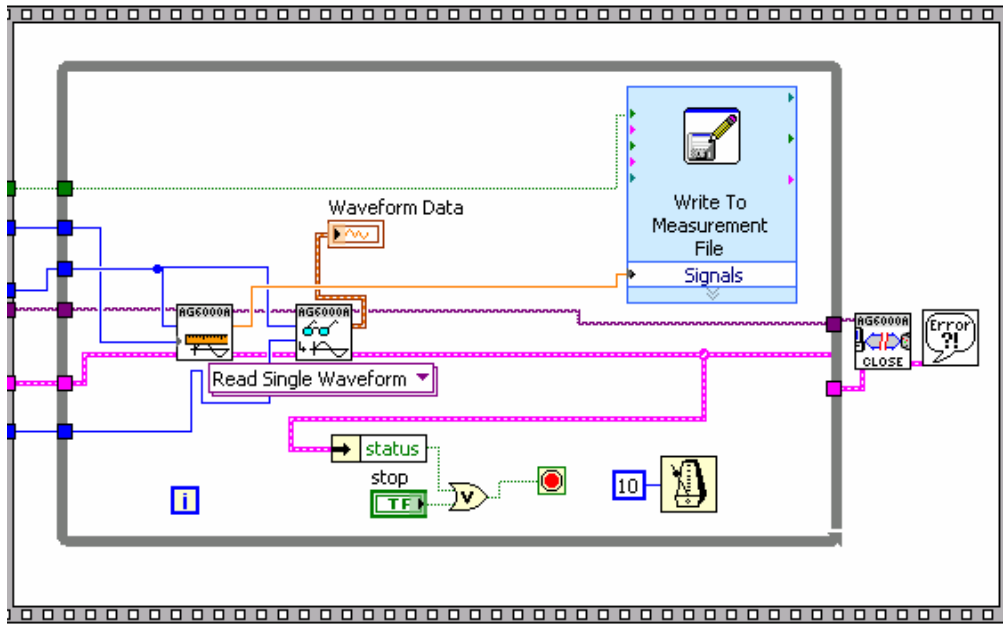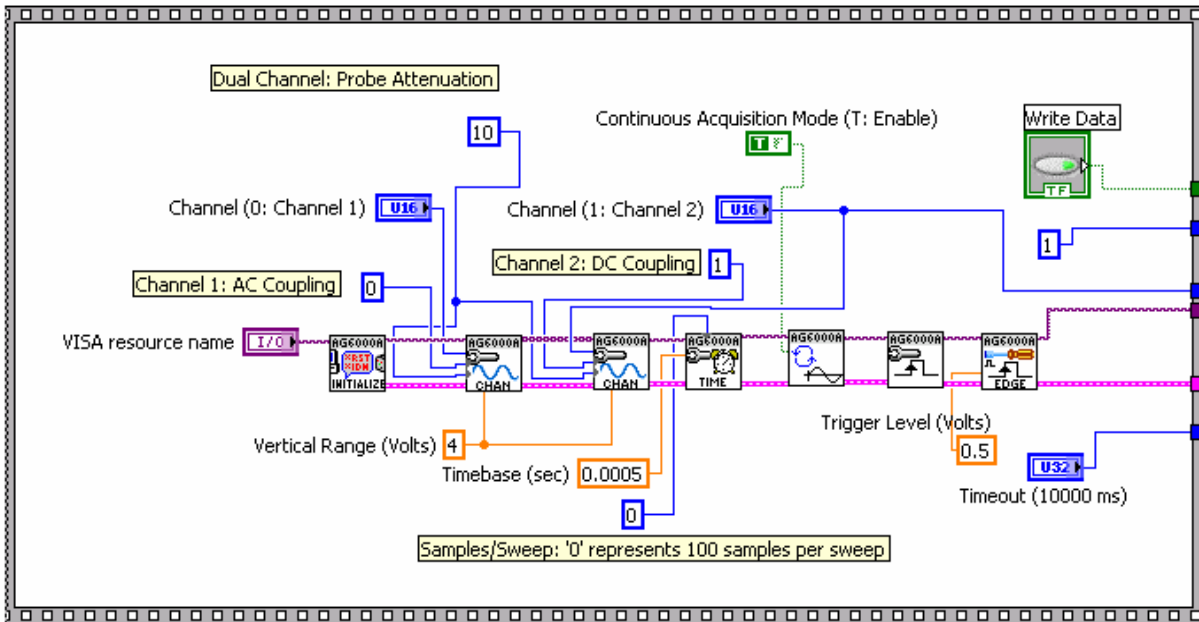
Figure 3.37: Block Diagram of Single-Oscilloscope Virtual Instrument (VI)

When LabView is instructed by the user to enter its run-mode, the program begins by executing the first frame of a flat-sequence. A flat-sequence is a collection of frames, inside of which the user may execute any sort of function, conditional loop, display update, etc. The

frames in the sequence execute in a specific order from left to right, only advancing to the next frame when all executables in the present frame have been successfully completed.

The first frame of the sequence seen in Figure 3.37 configures the Agilent MSO6012A to prepare for data acquisition. In this VI, the oscilloscope triggers off of the sinusoidal waveform measured across the electromagnet sensor. Therefore, channel one is set to AC coupling, while channel two is set to DC coupling since this channel will receive the DC output signal that will be recorded. The display of the oscilloscope is also controlled and configured by this frame, setting the vertical range to eight (8) volts and the timebase to 0.5 ms. Lastly, the oscilloscope is assigned to continuous acquisition mode and the trigger threshold value is set at 0.3 volts.

The second frame in the sequence executes the actual acquisition of the data and its storage to a pre-determined file location. Once the first frame has completed its functions, a while-loop is initiated and data is read from the appropriate channels on the oscilloscope. Once read, the DC voltage value is saved to a text file along with the relative sample time of the measurement. After storing this value, the while loop returns to the beginning and repeats the procedure. This loop will continue acquiring and storing data samples until the user tells the program to stop. In addition, the DC signal being read by the oscilloscope is displayed on the front-panel of the VI in a waveform plot, show below in Figure 3.38.
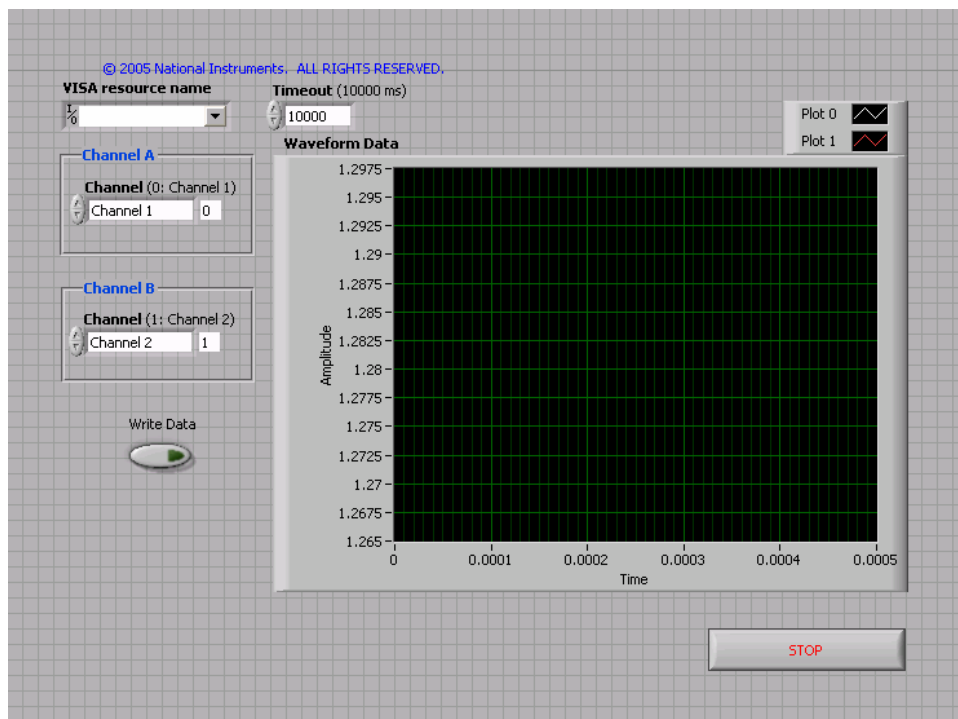
Figure 3.38: Front Panel of Single-Oscilloscope Virtual Instrument (VI)

One of the problems with the LabView and oscilloscope based system pertains to its maximum sample rate. Due to the limited capabilities of the MSO6012A as a hardware module, as well as the CPU resources required for the VI to write the data to a text file, this DAQ system can only record between 15-20 samples per second. While this sample rate will suffice for DC signal measurement, this system would be unable to accurately measure any signal with frequency content above a few hertz.

3.4.2 MATLAB DAQ with 1608FS

The second DAQ system consisted of an executable script developed using the MATLAB Data Acquisition Toolbox (DAT) and the Measurement Computing 1608FS hardware module as an A/D converter. This executable script, called an m-file can be referenced in Appendix B. It is immediately clear that the primary difference between this DAQ system and the aforementioned one is that where the LabView VI was constructed through a graphical block-diagram, the MATLAB m-file is a list of programming code in syntax appropriate for its compiler.

The m-file creates an analog-input object associated with the 1608FS hardware module with which data may be acquired from any of its eight (8) analog inputs. The sample rate and duration of the acquisition (in seconds) are set via the variables 'SampleRate' and 'duration', respectively. Also, the acquisition is set to begin once the voltage value on a separate channel exceeds a predetermined threshold value. In practice, this trigger channel will receive a voltage signal from a thermocouple placed inside the runner of a sand mold and will start the MATLAB script once it contacts the molten aluminum.

From the start of the acquisition to its completion, the data is read from the channels of interest and stored to a buffer within the computer. Once the acquisition is complete, the data is then extracted from this buffer and can be saved for further processing.

Compared to the LabView system described previously, the MATLAB system has the ability to sample an incoming signal at much higher rates due to the capabilities of the 1608FS hardware module. However, because the MATLAB system stores the incoming data values to a buffer during the acquisition process, the values are inaccessible for real-time display or processing. The data values in the LabView system are immediately accessible and would be capable of real-time processing in an actual implementation.

4 System Testing

In order to test the metal detection system, a number of different tests were performed to validate the system's performance and operational characteristics. The first test that the system underwent was a bench test, in the lab, where a piece of solid aluminum was used to simulate the molten aluminum. After the system was validated in the lab, the system was tested, on three different dates, at Metal Casting Technologies in Milford, NH to determine the performance and characteristics with molten aluminum. During each of the three days of testing, multiple designs and design modifications were tested.

4.1 Solid Aluminum Bench Test

To validate the function of the system before testing was done with molten aluminum, a sheet of 1/8" solid aluminum was used as a test material. Solid aluminum was used because it is as practically close to molten aluminum that could be used in the lab environment. To test the system, everything was set up as it would be for the first molten aluminum test. The setup consisted of the original bread boarded test circuit with a single coil. The circuit was connected to an Agilent MSO6012A Oscilloscope which was connected to a laptop running LabVIEW VI via USB.

In order to simulate an engine block filling with molten aluminum, a way of constantly moving a sheet of solid aluminum was needed. This was done by clamping the sheet of metal to a motorized track. The motor on the track was connected to a power supply and set to a constant DC voltage. The coil was mounted on the modified microphone stand support structure. The coil and sheet of aluminum were separated by a 6 inch gap while the metal was brought into the field of the coil at a constant rate.

The LabVIEW VI created for this test successfully collected data, and the data showed that the system was working as expected. The test was run to show proof of concept of the system with solid aluminum and to make sure the data acquisition system was working properly. The data from LabVIEW that resulted from the test is shown in Figure 4.1.
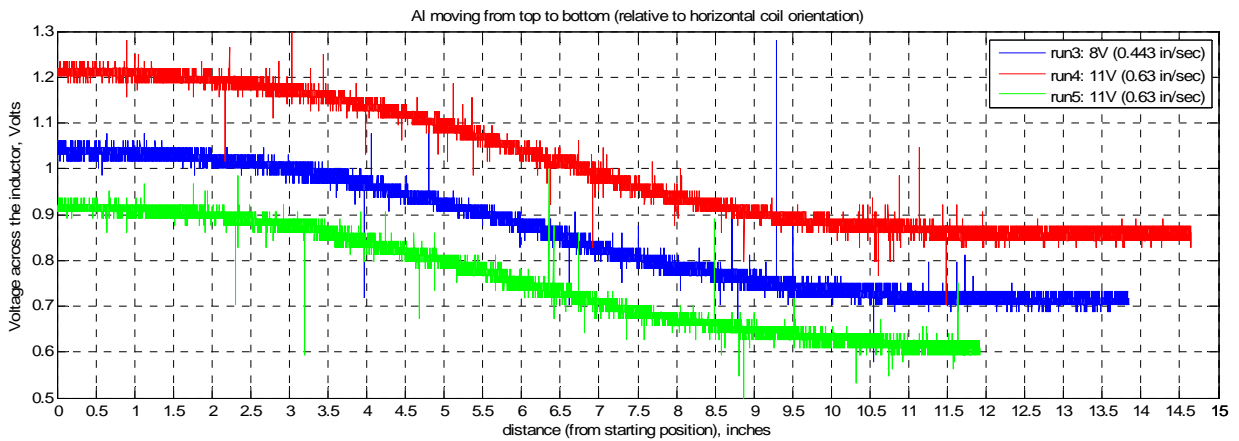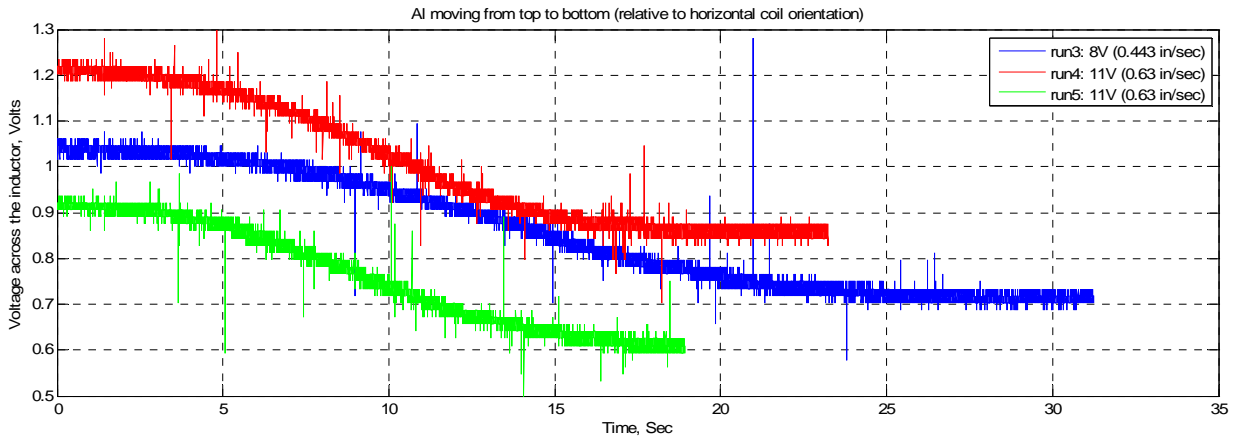
Figure 4.1: Resulting LabView data

Also, this test showed that the coil had about a 7 inch viewing area (3.5 inches above and 3.5 inches below the coil) at 6 inches away from the coil. A model of this viewing area can be seen in Figure 4.2.
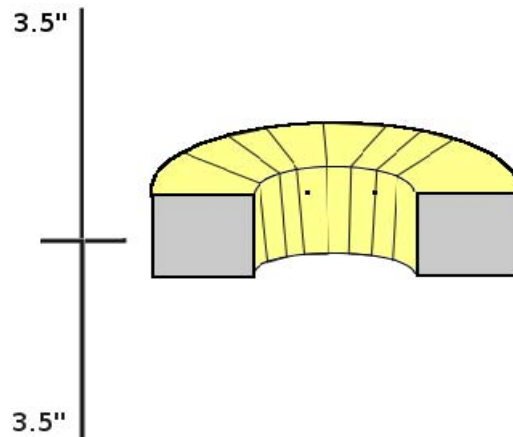
Figure 4.2: Coil Viewing Area

4.2 Molten Aluminum Testing

This section will look at the three tests that were performed using molten aluminum. The setup and results for each test will be detailed.

4.2.1 Test 1

The first molten aluminum testing was done at Metal Casting Technologies (MCT) in Milford, NH on November 10, 2006.

4.2.1.1   System Setup

The setup used for the first molten aluminum testing was done with a similar setup used for solid aluminum testing. The same oscilloscope (Agilent MSO6012A) was used in conjunction with a laptop running LabVIEW VI for collecting data. The circuit used was the single coil packaged circuit. The coil and scope were connected with BNC connectors to ensure secure connections. Figure 4.3 is an image of the equipment setup that was used for test #1. The laptop on the left is running the webcam while the laptop on the right is running the LabVIEW DAQ hooked up to the Oscilloscope.

Figure 4.3: Test 1 equipment setup

Three sand molds were prepared by MCT for this test. The molds were sand blocks with thermocouples inserted into the path of the flowing molten aluminum. Four inches of sand separated the coil mounted on the modified microphone stand from the molten aluminum flowing within the sand mold. The coil was aligned to a desired thermocouple for each test, which varied for each test. Figure 4.4 shows a model of the sand mold used. Molten aluminum was poured down the fiber downsprue and filled the sand model from the bottom, triggering the thermocouples as it filled.
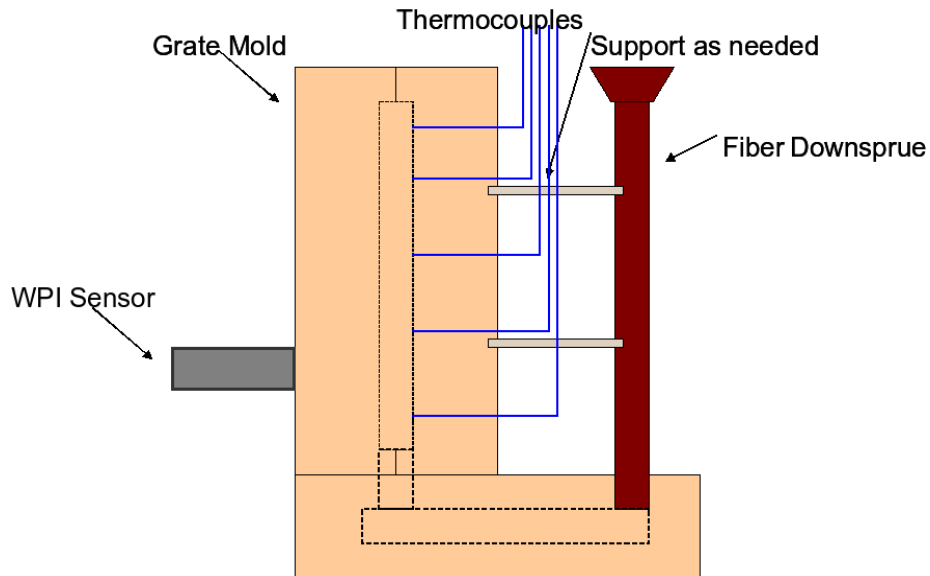
Figure 4.4: Test 1 system setup

A webcam was used to capture the screen of the oscilloscope to ensure data was collected during pours. This was used incase the LabVIEW data acquisition failed. Also, the entire pouring of the aluminum was videoed by MCT as documentation of the testing. Additional photos of the system setup can be seen in Appendix E.

4.2.1.2 Result of Visit

This test proved that the detection of molten aluminum through 4 inches of sand with an electromagnetic coil was possible. It was also determined that the heat of the molten aluminum would not affect the coil due to the rapid speed of the pour. The temperature at the coil was measured during the tests with a laser temperature sensor and found to be rising by only a few degrees Fahrenheit. This eliminated a problem that had raised some concern.

The test also demonstrated the ability of the data acquisition setup. The data collected was not synchronized with the thermocouple data as the two systems worked independently. An effort was made to synchronize the start of the systems and to time each of the three pours with a stop-watch. The reason for this was to try and couple the thermocouple data with the data output from LabVIEW. This however was not one of the goals of the tests and proved to be impossible without a system that was integrated (LabVIEW and the thermocouple system).

During test 1, three pours took place. All three pours were set up similarly. Appendix C and Appendix D show the setups for pours one and two. Pour three was discarded due to errors. Figure 4.5 shows a graph of the results from the first pour. The red line is the output from the

LabVIEW DAQ and the blue line is the output from the thermocouple DAQ. An attempt was made to match the data in time as best as possible, but it was impossible to match it perfectly. The graph is a best estimation of the synchronization between the thermocouples and the LabVIEW DAQ. The thermocouple data is shown normalized and the LabVIEW data is normalized, shifted, and flipped.
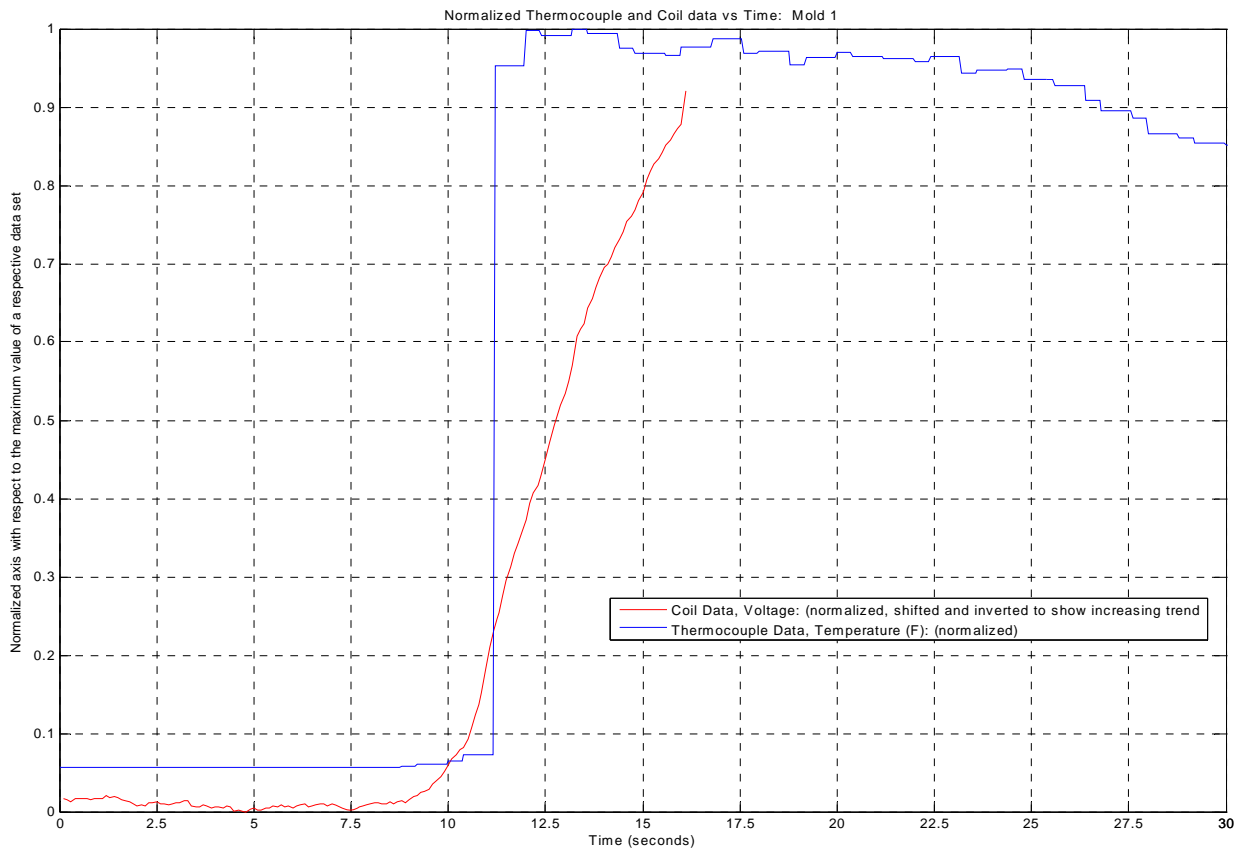
Figure 4.5: Test 1, pour 1 thermocouple data and LabVIEW data graph

The second pour resulted in similar results as the first pour, which helped verify that the system was working and showed proof of concept. Figure 4.6 shows a graph of the results from the second pour. The blue line is the output from the LabVIEW DAQ and the pink line is the output from the thermocouple DAQ. Again the two data sets have been paired together using a best estimation. The thermocouple data is shown again normalized and the LabVIEW data is again normalized, shifted, and flipped.
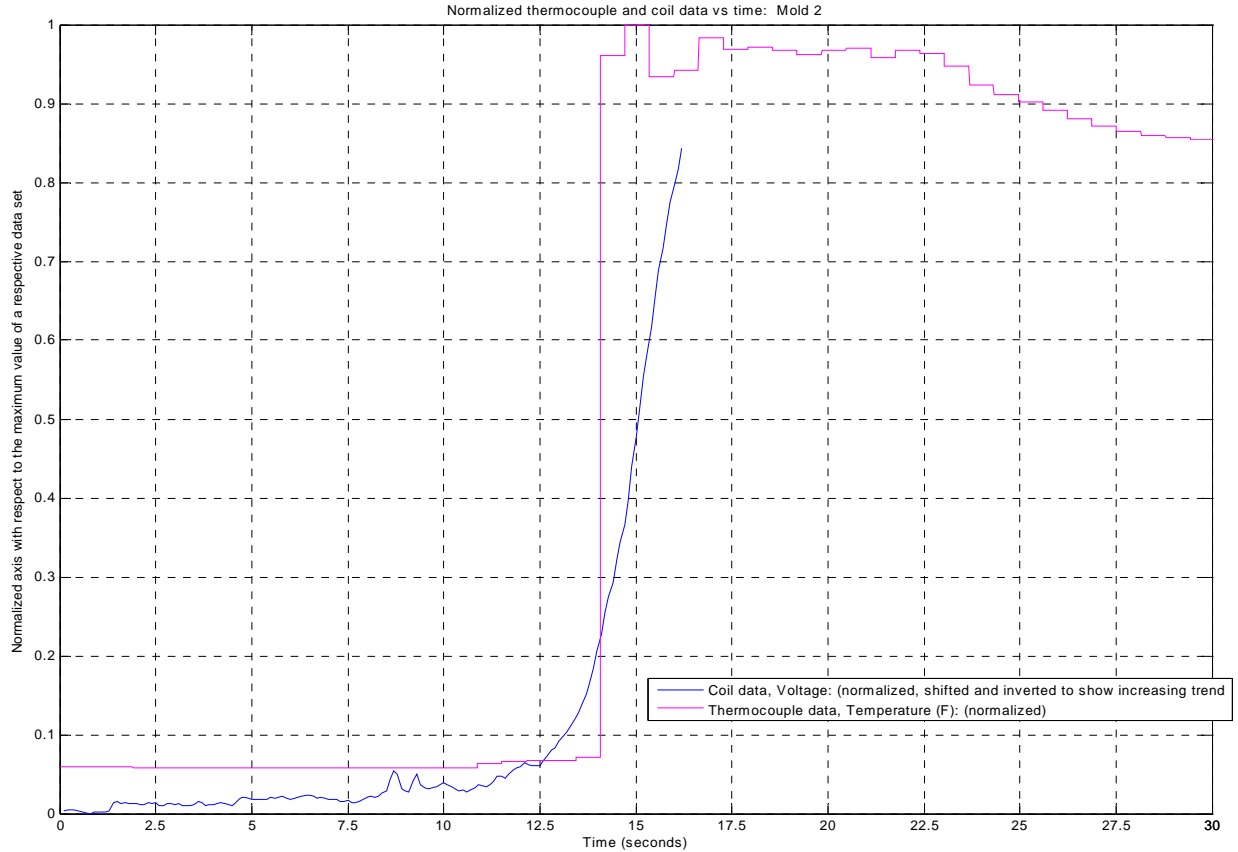
Figure 4.6: Test 1, pour 2 thermocouple data and LabVIEW data graph

Even though the data collected was not useful to correlate or characterize the system, the results from the overall test were important. This test demonstrated proof of concept and it was determined that the project would go under further development and require more testing. The conclusions from this test determined that a number of things needed to be improved and enhanced. The future tests would include bringing the coil away from the metal another 2 inches so it would be six inches from molten aluminum, introducing a multiple coil array, and creating better, more stable oscillator circuits with automatic gain control.

4.2.2 Test 2

The second molten aluminum testing was done at Metal Casting Technologies (MCT) in Milford, NH on December 8, 2006.

4.2.2.1   System Setup

For the second set of tests with molten aluminum, a similar setup to the first set of tests was used. The difference between the first and second set of tests was the number of coils used. The purpose of the test was to see how the coils would interact with each other and/or interfere with each other. An array of three coils was used along with a single circuit package with three oscillators. Two Agilent MSO6012A oscilloscopes were interfaced with a new VI in LabView. Figure 4.7 shows the setup of the circuit and data acquisition equipment.
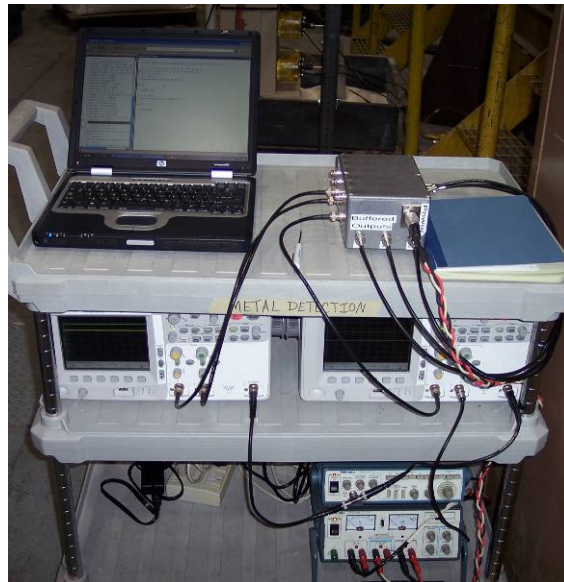
Figure 4.7: Test 2 circuit and data acquisition equipment setup

The new VI had the capability to capture data from the two oscilloscopes in addition to having an external start trigger. The trigger would be pressed at the same time as the trigger for the thermocouple data, so that the data could be aligned on a graph and the validity of the data checked. A new coil support structure was used to securely hold all coils in place for the tests as seen in Figure 4.8.
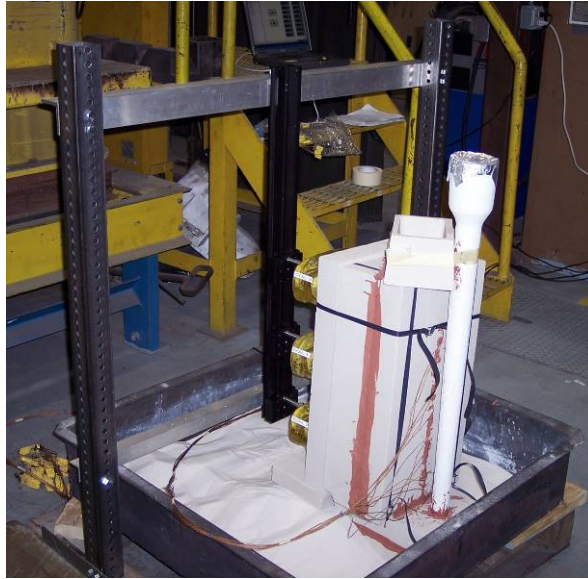
Figure 4.8: Coil support structure with coils and sand cast

Another difference with the setup of this test versus the first test was the addition of a data recording system developed by another MQP team as seen in Figure 4.9.

Figure 4.9: Data logger from other MQP group

Three sand molds similar to those created for test 1 were built by MCT for this set of tests. Each mold had a number of thermocouples to help validate the collected data from the coils. For these set of tests, six inches of sand will be used instead of four from test 1. The intended application of this technology will use six inches of sand. It was decided that the first pour would be setup with just the three coils, spaced seven inches apart, without the data logger attached. For the second test, the data logger was attached to the system. For the third test, the

data logger was removed and one coil was placed on the side of the sand cast as seen in Figure 4.10.
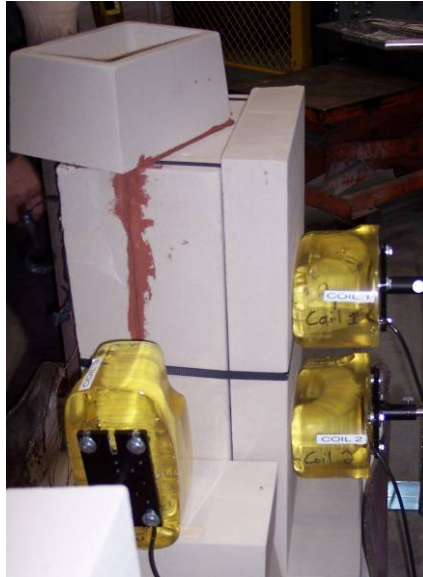
Figure 4.10: Coil located on front and side of sand cast

This was done to examine the effect of cross coupling with the coils and also to validate that the coil could see a smaller size face of metal. Additional pictures of the system setup can be seen in Appendix F.

4.2.2.2 Result of Visit

The results from the first pour into mold 1 were very promising. The samples output from LabView were taken and cleaned up and plotted in Matlab to obtain the results as seen in Figure 4.11.
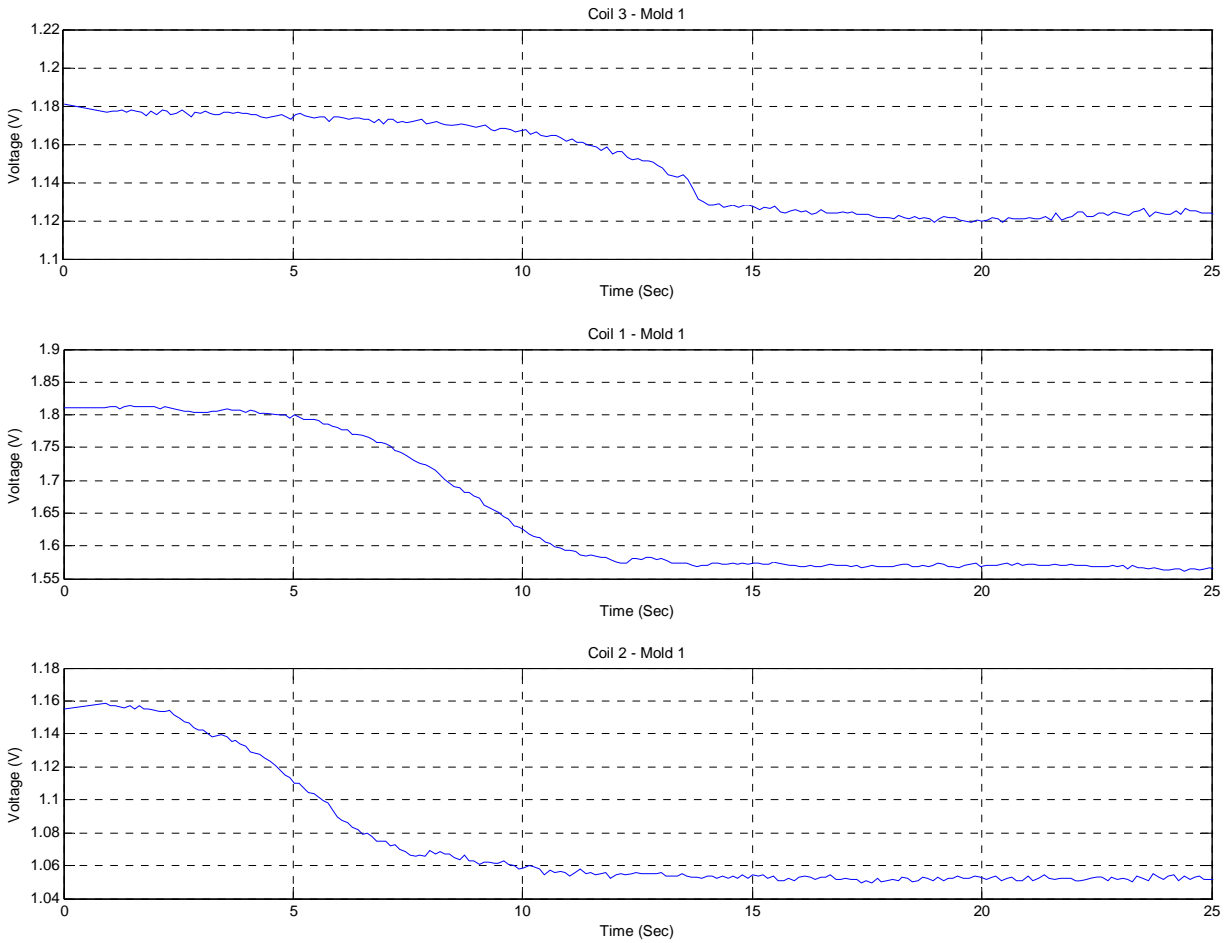
Figure 4.11: Test 2 mold 1 output

As seen in Figure 4.11, the voltage level of each coil dropped as metal was introduced into the field. The voltage level drops to the point at which the system cannot sustain oscillation, and then the output stays at a certain value. The output from each senor is almost identical, but shifted in time. This corresponds to the height of the metal within the mold. Coil 2 was the coil closest to the bottom of the mold and thus the first one to detect metal. As the level rose, it came into view of coil 1 and finally coil 3. The slope of the output determines the speed at which the metal is rising inside the mold. This is determined by how fast the metal is being poured into the mold by the foundry workers. Coil 3 detected a slight increase in speed of the metal inside the mold and thus the increase in speed by the foundry workers. Unfortunately during this test, there was an error with the thermocouples and no data was collected. In order to get a logical picture of the system output, the data was normalized and flipped within Matlab. Figure 4.12 shows a graph of the normalized and flipped output.
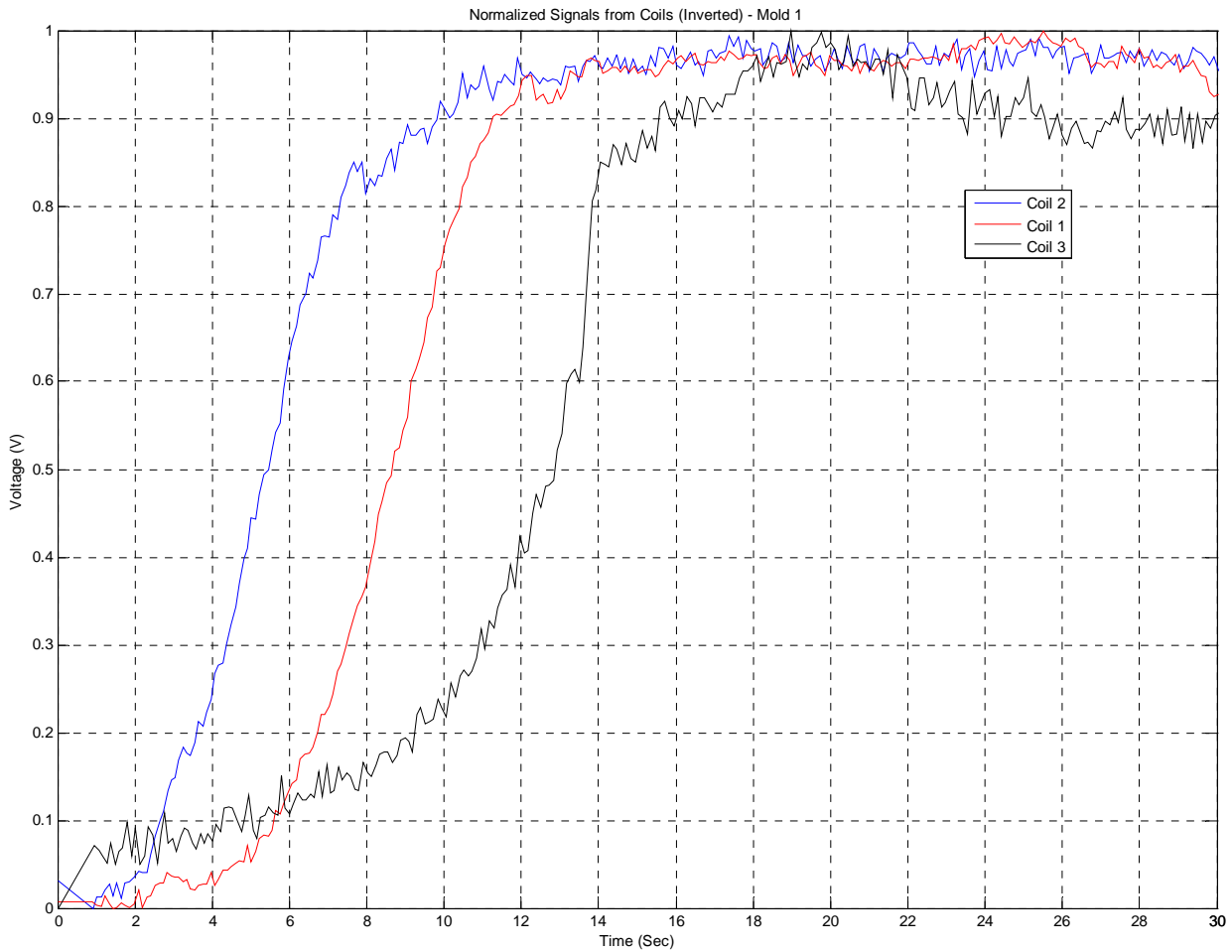
Figure 4.12: Test 2 mold 1 normalized output signals

This display is easier to intuitively understand. As time increases, each coil's voltage increases, corresponding to the increase in metal in its field of view. Each coil starts to detect the rise in molten aluminum as time progresses, indicated by the separation of the red, blue, and black lines.

When mold 2 was poured, the data logger from another MQP group was connected. This introduced noise into the signal, as seen in Figure 4.13.
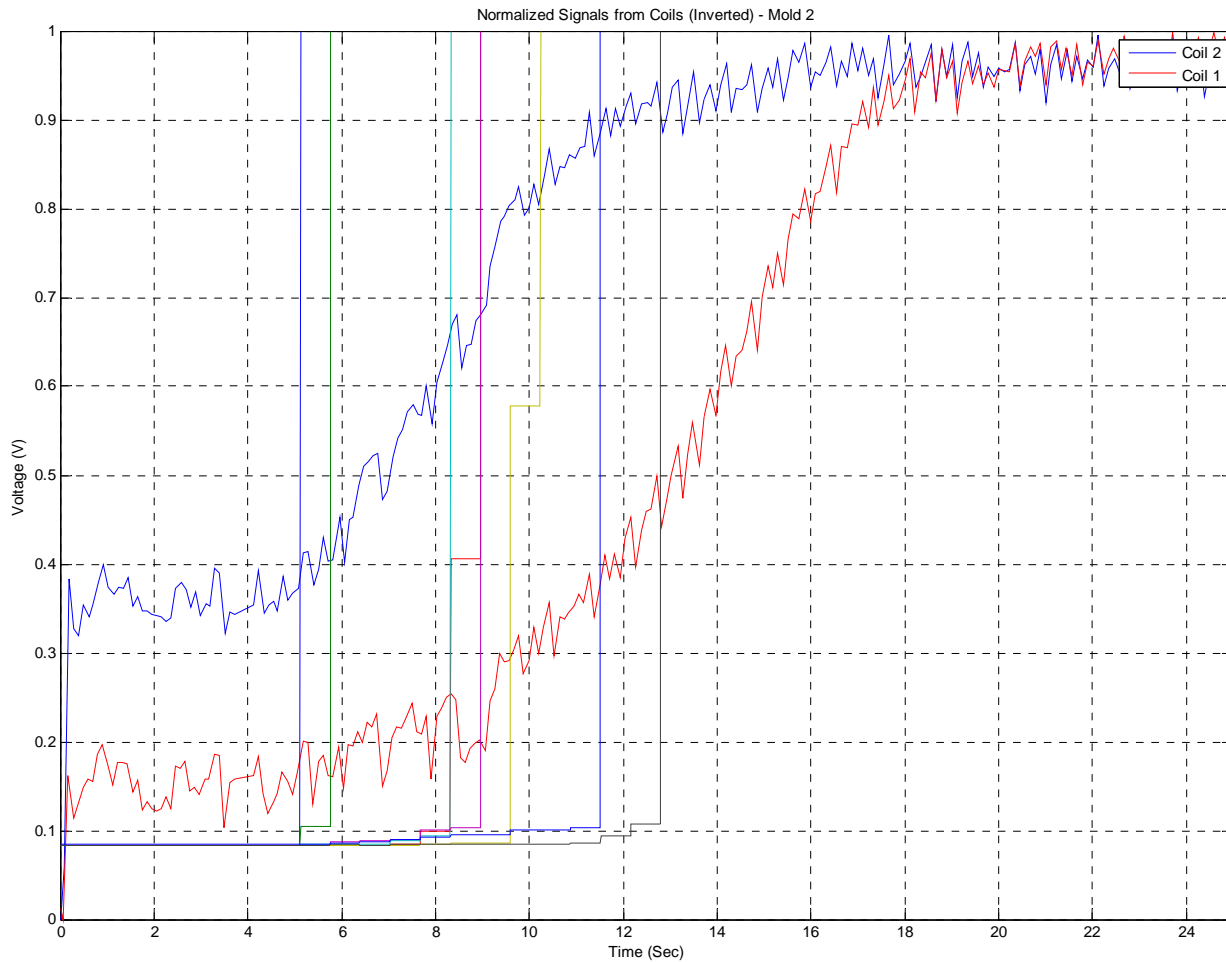
Figure 4.13: Test 2 mold 2 results

The results from mold 2 were not as good as the results from mold 1. Thermocouple data was gathered from the first eight thermocouples, but not from the remaining eight due to more thermocouple data acquisition failures. In this test, it can still be seen that the system detected the presence of molten aluminum in the field, but the output signal is not very clear, like mold 1. Also, only two sensors were used because of the limitations of the data logger.

The results from pour 3 were very similar to pour 1. For pour 3, the data logger was removed. The replication of results between pours helped verify that the system was working in a repeatable fashion.

4.2.3 Test 3

The third set of experiments with molten aluminum was conducted on March 5th, 2007 at Metal Casting Technologies, Inc. The purpose of the test was to evaluate the performance of the automatic gain control (AGC) circuit.

4.2.3.1 System Setup

For this set of experiments, a new grate mold was developed to eliminate several sources of error identified in prior tests. These sources of error were (1) an uneven metal-front, causing a discrepancy between the thermocouple-indicated position of the metal and its actual position, and (2) a lack of synchronization between the data acquisition (DAQ) systems used for the coil sensor and the thermocouples. Each of these issues were addressed to ensure that the conclusions derived from the experiments on the 5th would be as accurate as possible.
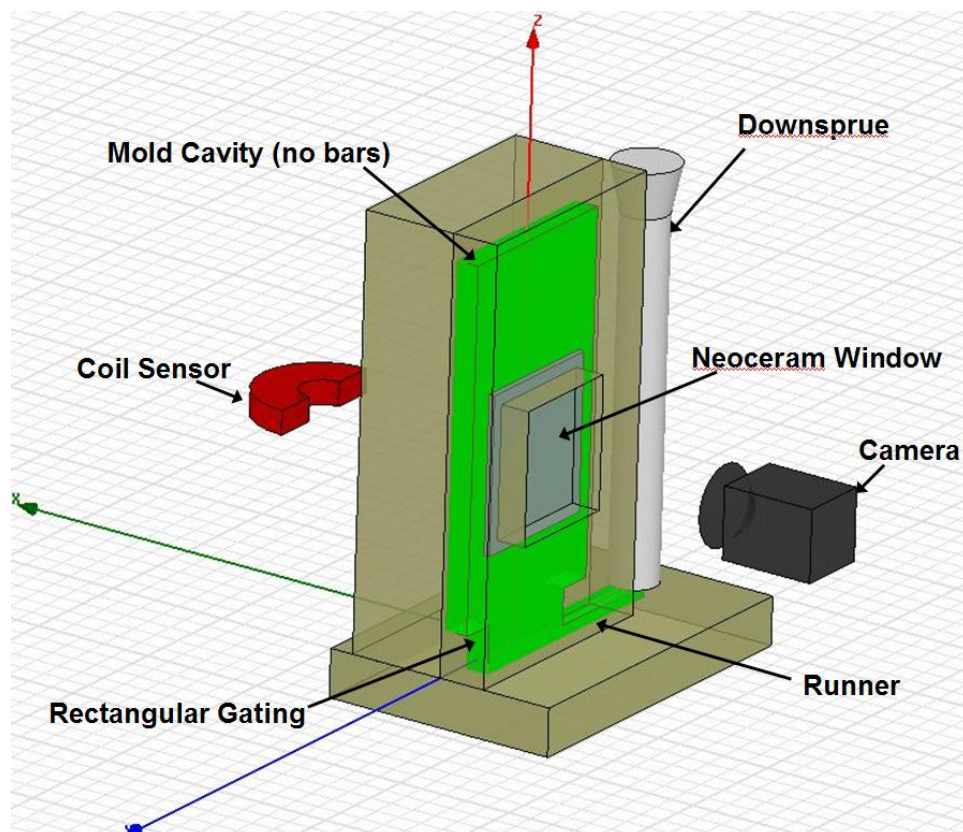
Figure 4.14: 3D Visualization of the new grate mold for Test 3

Figure 4.14 is a three-dimensional visualization of the new grate mold structure. One of the more apparent differences as compared to the previous setups is the piece of high-temperature ceramic glass, called Neoceram, placed within the mold. The dimensions of the glass are 10"x12"x3/16", providing a visible area of approximately 8"x10" (due to sand overlapping the edges of the glass). Neoceram has an extremely small thermal expansion coefficient ($-4e^{-7}$ /°C) and a high thermal shock resistance (800°C for a 100 x100x3 mm plate). Therefore, it is an ideal material to serve as a viewing window since it will be able to withstand the thermal shock of being in direct contact with 760°C molten aluminum. The reason for adding this viewing window was to use a high-speed camera to document the position of the metal front through video. Based on the intended placement of this camera (see Figure 4.14), the orientation of the downsprue and runner needed to be rotated by 90 degrees with respect to the mold.

To address the first source of error, changes were made to both the fill cavity of the mold, as well as the gating that delivers the metal from the runner to the mold. In the new molds, the columns of sand that originally created the bar-pattern in previous molds were removed. The reason for this was to ensure that there wouldn't be five separate columns of metal rising at different rates, and instead create a single metal front. In addition, the gating for the new molds was changed from a 1" hole at the center of the mold to a rectangular structure with the same horizontal dimension as the mold cavity. The purpose of this change was to eliminate the use of a single source with such a small cross-sectional area (1" hole) and instead have a "distributed" source with a much larger cross-section. A smaller cross-sectional source is more likely to create turbulent flow within the mold, so a wider gating structure helps eliminate the likelihood of this occurring.

The second challenge was to synchronize the two DAQ systems used for the sensor and thermocouples. The solution to this problem was to place a thermocouple in the gating of the mold to serve as a trigger/indicator. This thermocouple was connected to both DAQ systems so that each system would be able to monitor a common signal source. The result was a time-stamp by which the data from both systems could be synchronized to minimize error due to time-offset.

Figure 4.15 is an actual photo of the new grate mold used in the experiments of Test 3.
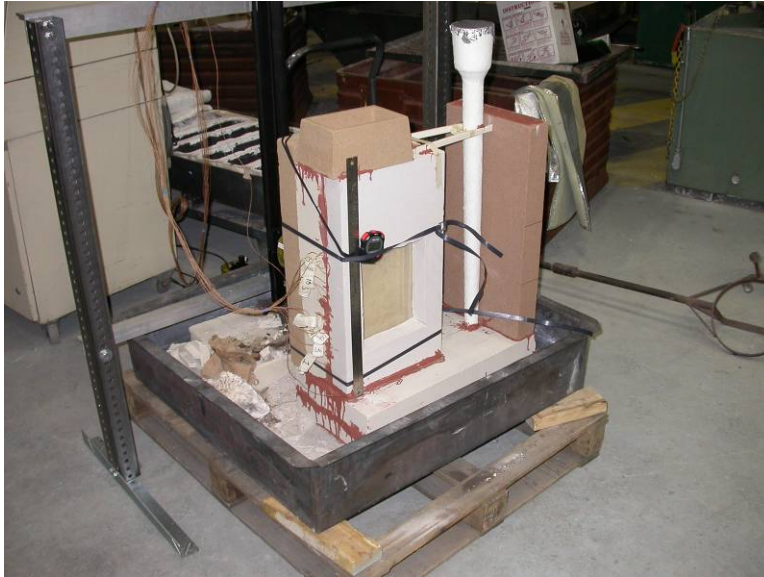
Figure 4.15: New Grate Mold for Test 3

The data acquisition system used to acquire the error signal from the AGC circuit is the MATLAB based DAQ system described in section 3.3.2. The MATLAB system is capable of much higher sampling rates and also streamlines the process of taking the raw sensor data and producing plots for post-processing. Additional pictures of the system setup can be seen in Appendix G.

4.2.3.2 Results

Two molds were filled with molten aluminum as part of test 3. The two error signals acquired from the AGC circuit for molds 1 and 2, respectively, are shown in Figure 4.16. The position of the coil sensor with respect to the bottom of the grate mold was changed between the two molds. For mold 1, the center of the sensor was positioned 6 inches from the bottom of the mold, while for mold 2, the sensor was position at 10 inches from the same reference point. This variation in sensor placement explains the horizontal shift between the two signals.
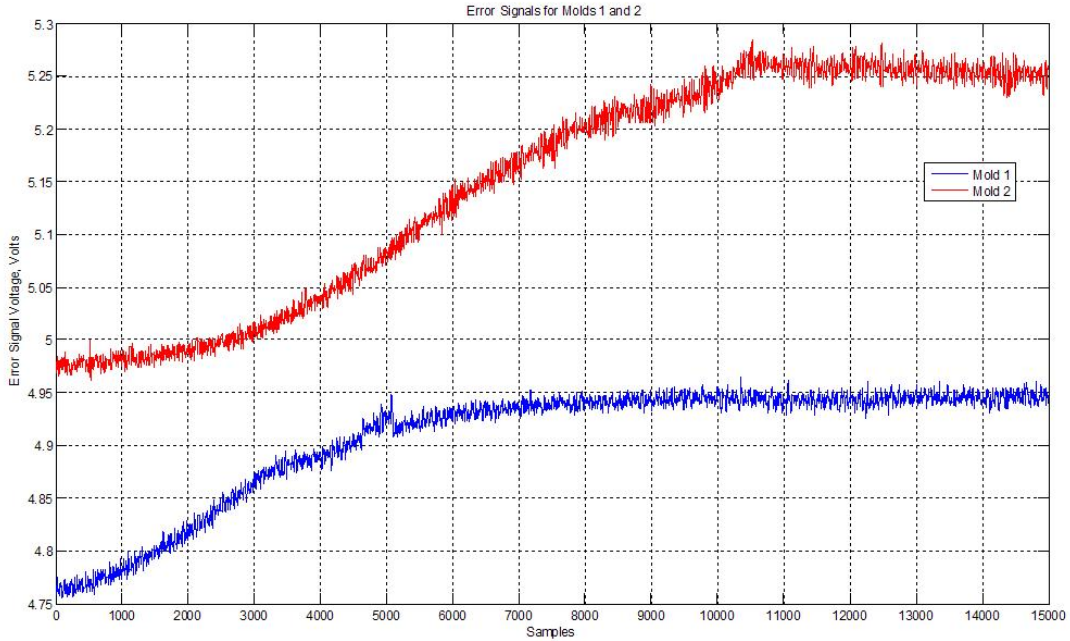
Figure 4.16: Error Signals output by the AGC circuit for Molds 1 and 2

Based on the 7 inch field-of-view for the coil sensor (as determined from the solid aluminum tests) and the total change in voltage for each error signal, the signal traces were scaled appropriately to describe the position of the molten metal front with respect to time. To validate the accuracy of this scaling and the performance of the AGC system overall, the thermocouple data from the second DAQ system was plotted with the scaled coil signal. Figure 4.17 is a plot of the scaled sensor signal and the thermocouple data from mold 1.
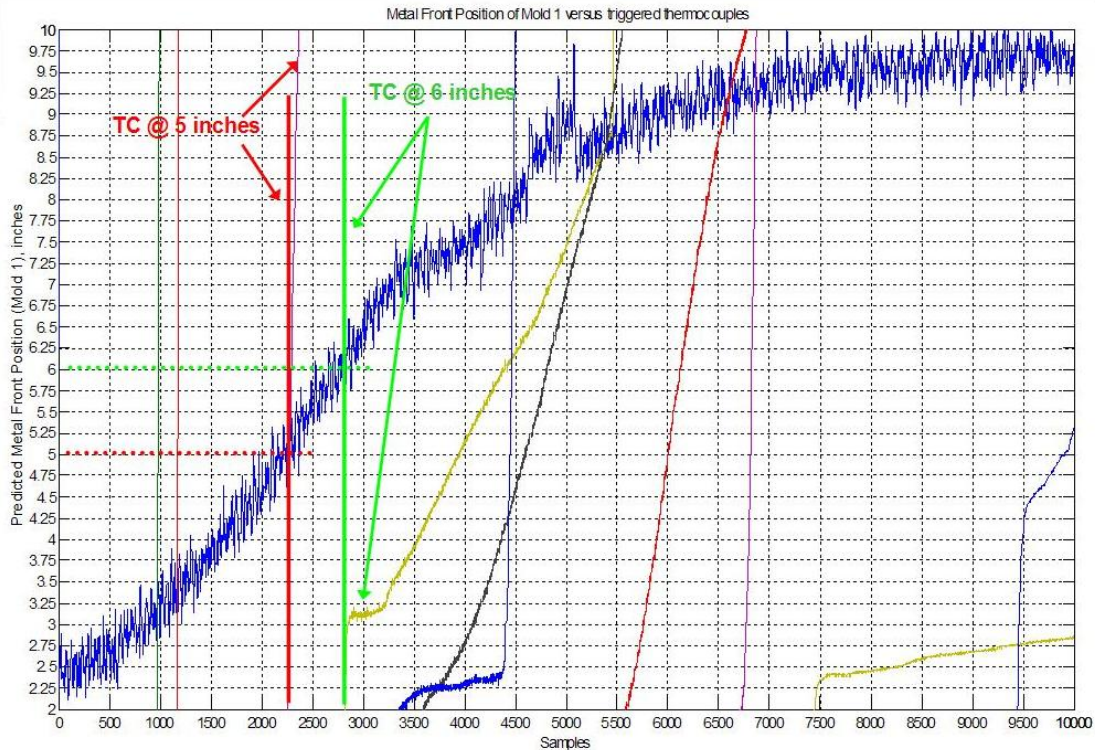
Figure 4.17: Sensor signal and thermocouple data illustrating the accuracy of the AGC system

Two thermocouple traces were chosen to evaluate the accuracy of the sensor system; the first at 5 inches and the second at 6 inches from the bottom of the grate mold. At the instant that the thermocouples were triggered by coming into contact with the molten aluminum, the metal front positions at those instances were compared with the physical locations of the thermocouples. As can be seen in Figure 4.17, the positions provided by the coil sensor compare extremely well with the physical positions of the thermocouples. The plot shows that the system was able to resolve the position of the metal front to within a ±0.25 inch margin of error. This error margin is due to the noise present on the sensor signal and it may be possible to eliminate some of this noise to further improve the resolution of the system.

The experiments conducted on March 5th highlighted a particular problem that must be addressed in order to display the metal front position in real time to a high degree of precision. Consider Figure 4.16 noting that the starting-voltage output by the AGC drifted by approximately 200 millivolts (mV) between the two experiments. While this variation in starting value can be eliminated by zeroing the signal, the problem is that the voltage drift changes the sensitivity of the system. For Mold 1, the change in voltage between no metal present and complete saturation is approximately 150 mV, while for Mold 2, the change in voltage was

almost 250 mV. It is absolutely critical that the sensitivity of the system remains constant from one pour to the next; otherwise it will be impossible to repeatedly predict the metal front position to any appropriate degree of accuracy.

5 Project Conclusions

5.1 Future Advancements

There are a number of advancements that need to be made to the project before it should be used in its intended setting. Within the two key elements of the project, the circuit and the coil, there are a number of advancements to be made. The many advancements for each piece of the project is detailed in the following sections, with the last section detailing how the entire system needs to be improved before use.

5.1.1 Circuit

The circuit could be further improved in a number of ways. The main problem with it currently is its temperature instability. The temperature instability is a result of using the MOSFET as a variable resistance. Also, the circuit needs to have a means to calibrate itself before each pour. The voltage level drifts slightly over time and with temperature variations. Another way the circuit could be improved is with a different type of oscillator that could be more sensitive to power loses. The current output is decent, but there could be a better signal to noise ratio. At this time, it is not known exactly what the output needs to be due to the lack of a design for a complete system with a pump integrated.

5.1.2 Coil

The electromagnet sensor could be further improved though various means of magnetic field-focusing. With the poles of the sensor oriented horizontally, the vertical field-of-view of the coil is seven (7) inches (±3.5 inches from the midpoint of the coil), illustrated below in Figure 5.1.
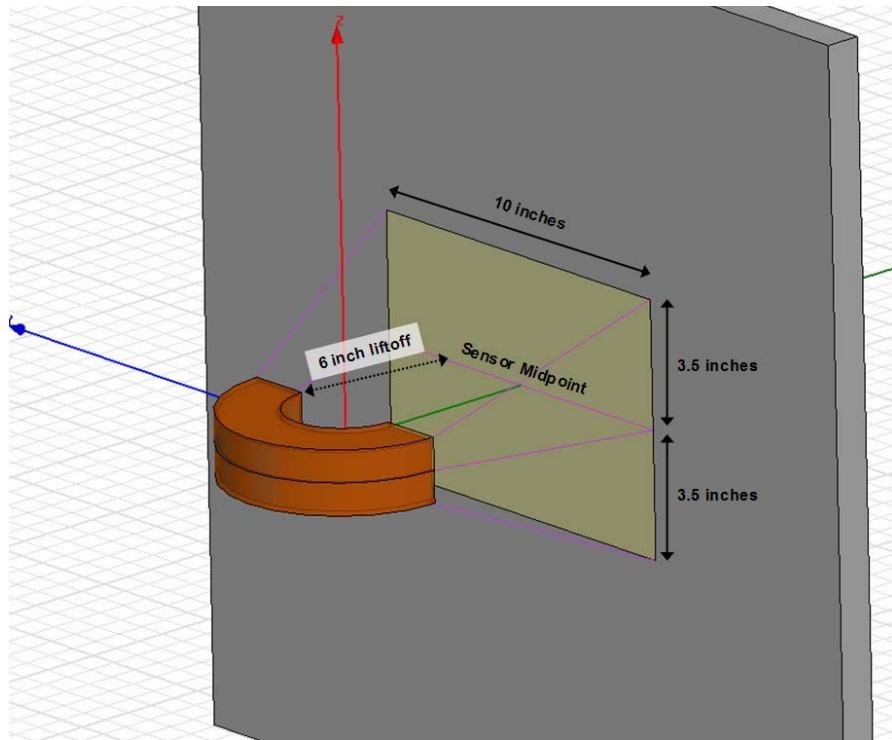
Figure 5.1: Screen-Shot of the C-Core Sensor, illustrating its Field-of-View (FOV)

This field-of-view may be too large for a specific application, such as an engine block, where increased resolution may be a priority. In such a case, an array of sensors forming a two dimensional matrix would be necessary, thereby requiring that both the field-of-view and physical size of the sensors be minimized. Such adjustments would be necessary to maximize the 2-D resolution of the system while minimizing the effects of cross-coupling between adjacent sensors.

To meet the design criteria for a smaller sensor, software packages such as COMSOL Multiphysics and Ansoft's Maxwell 3D could be used to determine the best possible design. By configuring what is called an optimetric simulation, the software could continually vary the design parameters of the sensor, including its physical dimensions and the shape of its poles, until the criteria for the new sensor are fully met. The power of a tool such as this is indescribable, saving countless hours and dollars on experimentation with various prototypes and magnetic materials.

The most interesting facet of the redesigned sensor would be the shape of its poles. If the poles of the new sensor could be shaped according to some contour, they would then behave like a magnetic lens by focusing the magnetic field lines in a particular direction. Such a technique

would make a huge impact by decreasing the overall size of the sensor while maintaining its ability to sense molten aluminum at a liftoff of six (6) inches.

5.1.3 Overall System

The primary means by which the overall performance of the non-invasive melt monitoring system could be improved concerns the data acquisition (DAQ) system. To this point, the DAQ systems employed have only been able to store data for post-processing after the mold has been filled. General Motors (GM) would like to know the position of the metal front in real-time (or as close to it as possible) so that adjustments could be made to the flow rate of the aluminum while the mold is filling. Ideally, these adjustments would be made automatically through a control interface to the aluminum pumping system. However, GM would be content with some sort of display that could be referenced by a technician to adjust the metal flow rate manually.

The DAQ systems used thus far have not been designed for continuous display of the incoming data, but could certainly be reconfigured to do so. LabView would be a particularly ideal piece of software to create a real-time display due to its graphic-based design and front-panel display capabilities. If the oscilloscopes used previously were replaced by a dedicated DAQ hardware unit, like the 1608FS from Measurement Computing, LabView would be much more flexible concerning user access to incoming data streams. In fact, once the thermal-drift issue has been resolved and the response of the AGC error signal is consistent and repeatable, LabView would be able to scale the incoming data and display a strip chart of metal-front position with respect to time quite easily. Beyond this real-time display, it would not be very difficult to take the next step and generate an analog output signal which could be interfaced with the pumping system to close the control loop completely.

6 Works Cited

[1]   F.T. Ulaby, <u>Electromagnetics for Engineers</u>, New Jersey: Pearson Prentice Hall, 2005.

[2]   "Mutual Inductance (The Basis for Eddy Current Inspection)," [Online Document],
Available at HTTP : http://www.ndt-
ed.org/EducationResources/CommunityCollege/EddyCurrents/Physics/mutualinductance.htm
        Date Accessed: December 19, 2006

[3]   "Depth of Penetration & Current Density," [Online Document], Available at HTTP:
http://www.ndt-
ed.org/EducationResources/CommunityCollege/EddyCurrents/Physics/depthcurrentdensity.htm
        Date Accessed: December 19, 2006

[4]   "Impedance," [Online Document], Available at HTTP: http://www.ndt-
ed.org/EducationResources/CommunityCollege/EddyCurrents/Physics/impedance.htm
        Date Accessed: December 19, 2006

[5]   "Display - Complex Impedance Plane (eddy scope)," [Online Document], Available at
HTTP: http://www.ndt-
ed.org/EducationResources/CommunityCollege/EddyCurrents/Instrumentation/impedanceplane.
htm
        Date Accessed: December 19, 2006

[6]   J.V. Wert, "Precision Sand Casting," [Online Document], Available at HTTP:
http://www.moderncasting.com/MoreInfo/0206/MoreInfo0206.pdf
        Date Accessed: December 19, 2006

[7]   "Basic Principles of Eddy Current Inspection," [Online Document], Available at HTTP:
http://www.ndt-
ed.org/EducationResources/CommunityCollege/EddyCurrents/Introduction/IntroductiontoET.ht
m
        Date Accessed: December 19, 2006

[8]   "Present State of Eddy Current Inspection," [Online Document], Available at HTTP:
http://www.ndt-
ed.org/EducationResources/CommunityCollege/EddyCurrents/Introduction/presentstateofET.ht
m
        Date Accessed: December 19, 2006

[9]   "Electronic Oscillator," [Online Document], Available at HTTP:
http://en.wikipedia.org/wiki/Electronic_oscillator
        Date Accessed: December 19, 2006

7 Appendices

Appendix A – MATLAB Transfer Function Code

```
%Non-Invasive Metal Detection - MQP
%MATLAB CODE
%Transfer Function - RLC Oscillator
%Generate Magnitude and Phase Plots

%Clean Up MATLAB
close all;
clear all;
clc;

%Define Values
R   = 1e3;          %Resistor [Ohm]
C   = 0.02e-6;      %Capactor [F]
L   = 1.648e-3;     %Inductor [H]

%Set Linear Frequency
f   = 100:1:1000000;     %[Hz]

%Convert to Angular Frequency
w   = 2*pi*f;            %[rad/sec]

%Transfer Function [H(jw)] - RLC Circuit (Tank Circuit)
%H(jw)
H   = 1./(1 + R*(j*w*C + 1./(j*w*L)));

%Find Magnitude of H(jw)
mag_H = abs(H);

%Find Phase of H(jw)
phase_H = angle(H)*180/pi;


%Plot Magnitude
subplot(2,1,1);
semilogx(f,mag_H);
grid on;
ylabel('|H(j\omega)|');
title('Magnitude');

%Plot Phase
subplot(2,1,2);
semilogx(f,phase_H);
grid on;
xlabel('f (Hz)');
ylabel('\angleH(j\omega) (\circ)');
title('Phase');
```

Appendix B – MATLAB DAQ Code

```
% GM/MCT MQP-1: Non-Invasive Melt Monitoring
% B. M. Foley, H. E. Jensen, S. D. Hallinan
% February 21st, 2007
% This M-file uses the Data Acquisition Toolbox to acquire data from the
%1608FS hardware module by Measurement Computing and plot the acquired data immediately
```

Create and configure the Analog Input Object

```
AI = analoginput('mcc', 0);
chans = addchannel(AI, 0:7, 1:8, 'analog channels');
duration = 20;
SampleRate = 1000;
set(AI, 'TriggerType', 'Software');
set(AI, 'TriggerCondition', 'Rising');
set(AI, 'TriggerChannel', chans(8));
set(AI, 'TriggerConditionValue', 2.5);
set(AI, 'SampleRate', SampleRate);
set(AI, 'SamplesPerTrigger', duration*SampleRate);
```

Create "real-time" display plot

```
figure
subplot(2,1,1)
set(gcf,'doublebuffer','on') %Reduce plot flicker
P = plot(zeros(10,1));
T = title([sprintf('Peekdata calls: '), num2str(0)]);
xlabel('Samples'), axis([0 10 -0.5 2]), grid on
```

Start the acquisition

```
start(AI);
i = 1;
while AI.SamplesAcquired < AI.SamplesPerTrigger
        while AI.SamplesAcquired < 10*i
        end
        data = peekdata(AI,10);
        set(P,'ydata',data(:,1));
        set(T,'String',[sprintf('Peekdata calls: '),num2str(i)]);
        drawnow
        i = i + 1;
end
```

Remove data from the buffer and Plot

```
data = getdata(AI);
subplot(2,1,2)
plot(data(:,1))
axis([0 length(data) -0.5 2]);
grid on
save data

delete(AI);
clear AI;
```

Appendix C – Test 1 Pour Setup 1

Thermocouples

Grate Mold

Support as needed

Fiber Downsprue

WPI Sensor

8.5 in

7.0 in
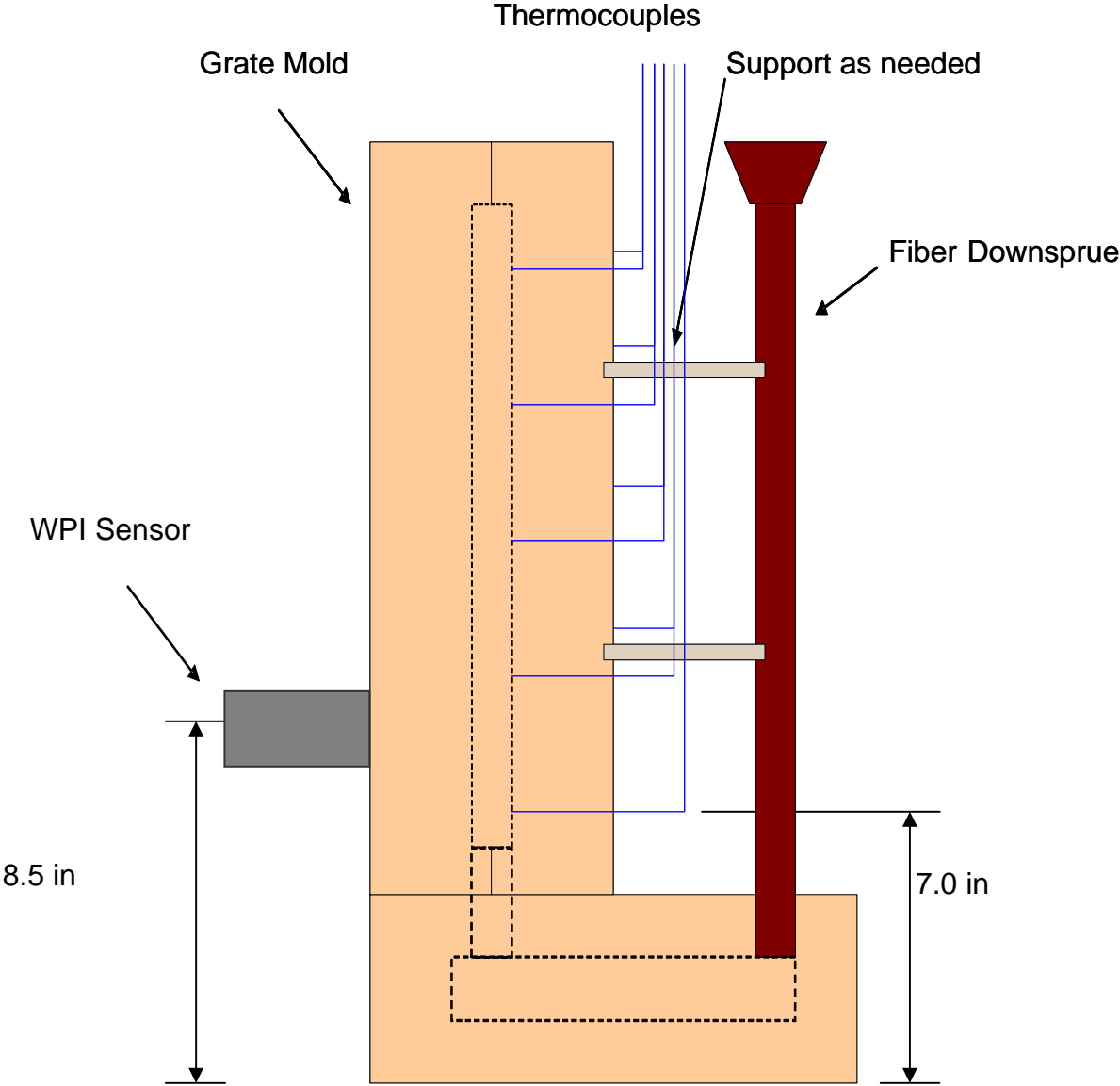
Appendix D – Test 1 Pour Setup 2
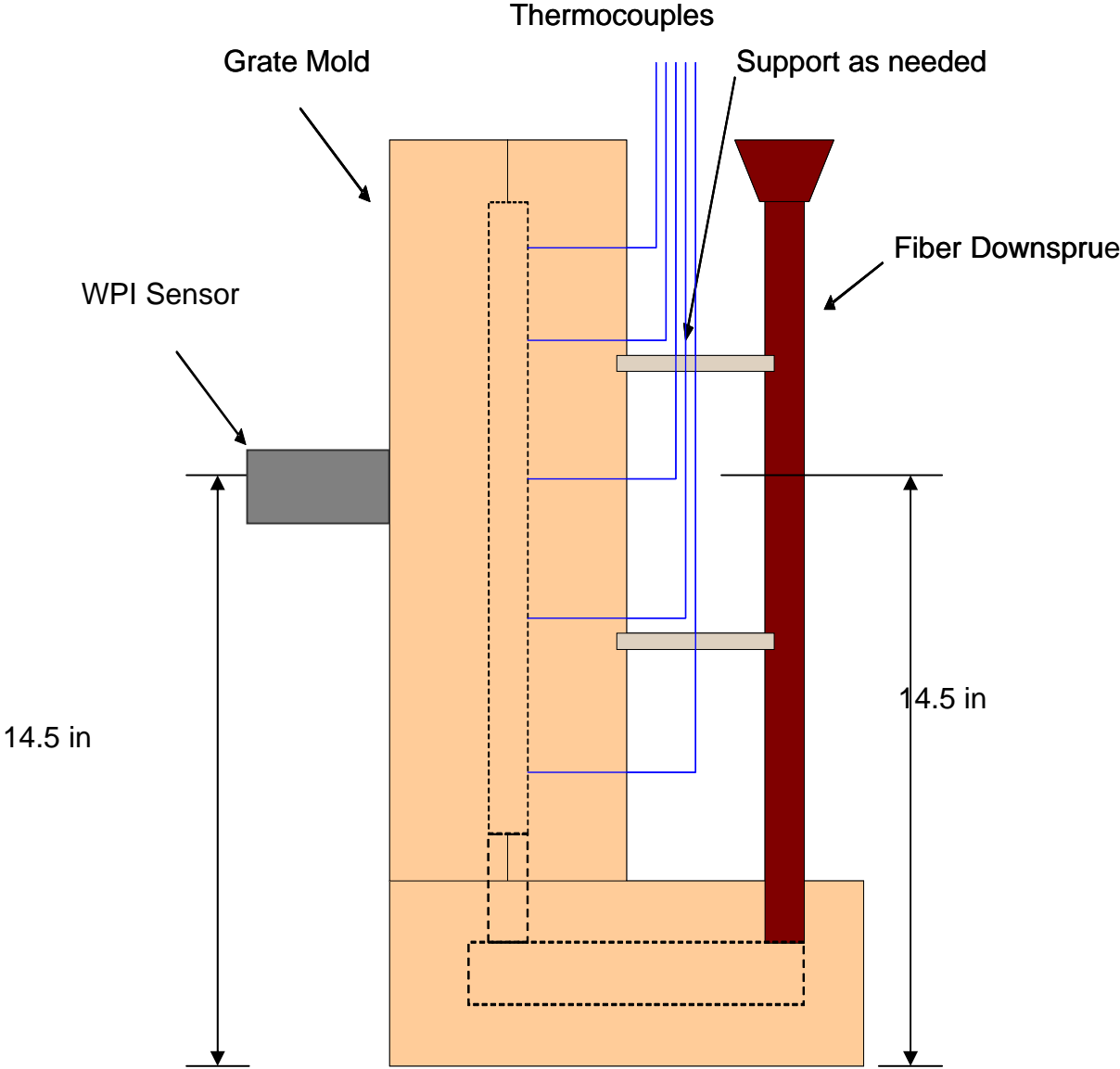
Appendix E - Additional Photos from Test 1

Mold after being filled with molten aluminum

Professor Sergey Makarov and Professor Reinhold Ludwig investigate the sand mold before the first pour

Inside details of sand mold close-up
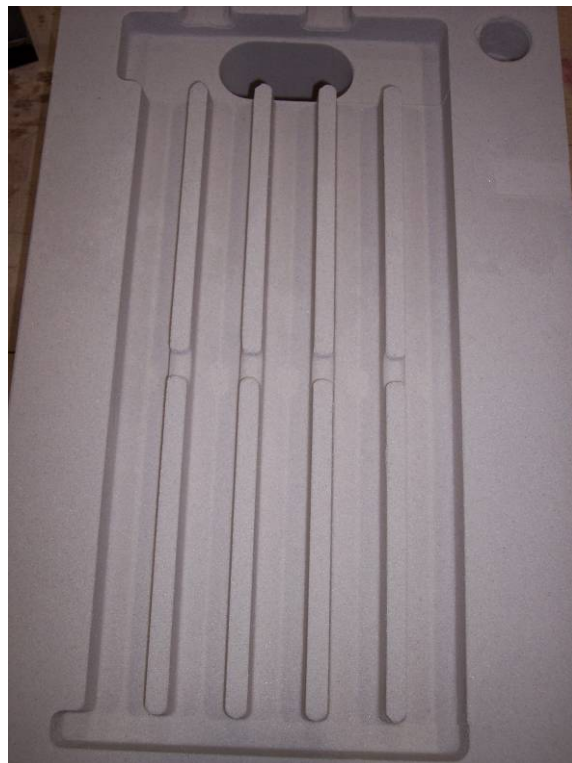
Inside details of sand mold – complete picture
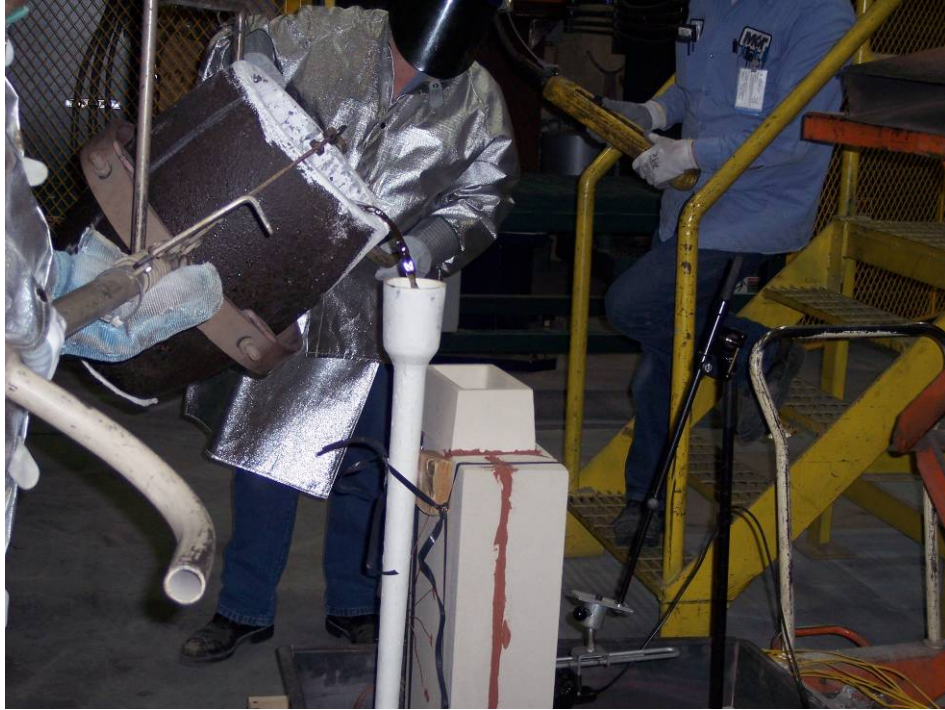
Foundry workers pouring molten aluminum into the first sand mold

View of down-sprue after aluminum has been poured

Appendix F - Additional Photos from Test 2

Professor Sergey Makarov testing the temperature of the molten aluminum with his finger

MCT foundry worker demonstrating the "stickiness" of molten aluminum

Foundry workers pouring molten aluminum into sand cast used for testing

Sean Hallinan ready to press the button to synchronize the thermocouple system and the coil system

Scott's hands trying to make the thermocouple system work correctly

Appendix G - Additional Photos from Test 3

View of sand mold set up and ready to be poured

View of sand mold with glass window to view the molten aluminum

Close-up view of glass window on the sand mold
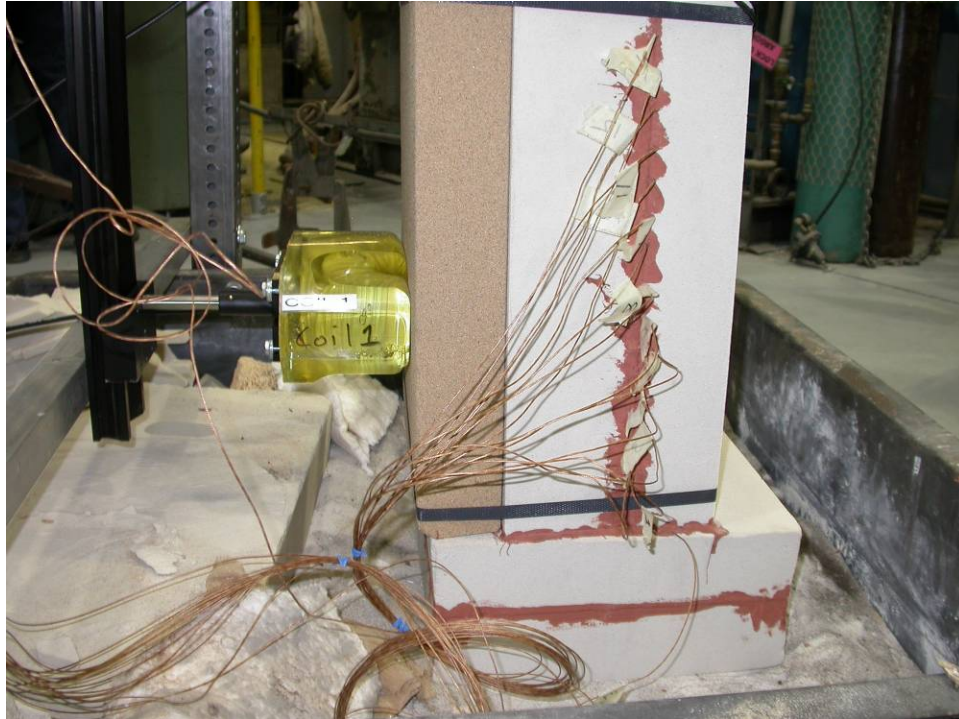
Close-up of coil and thermocouples embedded into the sand mold

Circuitry and DAQ system used for testing

Appendix H – Component Data Sheets

1. LM741

National Semiconductor

August 2000

LM741
Operational Amplifier

General Description

The LM741 series are general purpose operational amplifiers which feature improved performance over industry standards like the LM709. They are direct, plug-in replacements for the 709C, LM201, MC1439 and 748 in most applications.

The amplifiers offer many features which make their application nearly foolproof: overload protection on the input and output, no latch-up when the common mode range is exceeded, as well as freedom from oscillations.

The LM741C is identical to the LM741/LM741A except that the LM741C has their performance guaranteed over a 0°C to +70°C temperature range, instead of −55°C to +125°C.

Features

Connection Diagrams

Metal Can Package

NC
OFFSET NULL ①
INVERTING INPUT ②
NON-INVERTING INPUT ③
④ V⁻
⑤ OFFSET NULL
⑥ OUTPUT
⑦ V⁺
⑧ NC
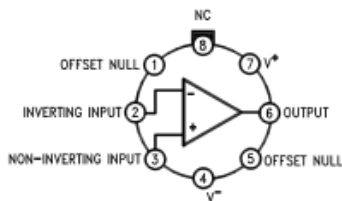
00934102

Note 1: LM741H is available per JM38510/10101

Order Number LM741H, LM741H/883 (Note 1), LM741AH/883 or LM741CH
See NS Package Number H08C

Dual-In-Line or S.O. Package

OFFSET NULL — 1   8 — NC
INVERTING INPUT — 2   7 — V⁺
NON-INVERTING INPUT — 3   6 — OUTPUT
V⁻ — 4   5 — OFFSET NULL
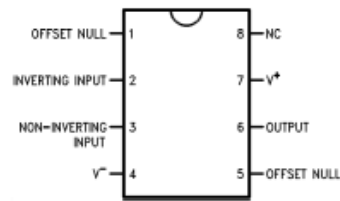
00934103

Order Number LM741J, LM741J/883, LM741CN
See NS Package Number J08A, M08A or N08E

Ceramic Flatpak

NC — 1   10 — NC
+OFFSET NULL — 2   9 — NC
−INPUT — 3   8 — V+
+INPUT — 4   7 — OUTPUT
V− — 5   6 — −OFFSET NULL
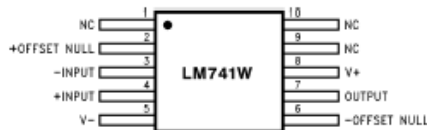
LM741W

00934106

Order Number LM741W/883
See NS Package Number W10A

Typical Application

Offset Nulling Circuit

LM741
OUTPUT
10 kΩ
V−

00934107

89
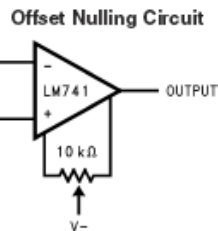
Absolute Maximum Ratings (Note 2)

If Military/Aerospace specified devices are required, please contact the National Semiconductor Sales Office/ Distributors for availability and specifications.

(Note 7)

	LM741A	LM741	LM741C
Supply Voltage	±22V	±22V	±18V
Power Dissipation (Note 3)	500 mW	500 mW	500 mW
Differential Input Voltage	±30V	±30V	±30V
Input Voltage (Note 4)	±15V	±15V	±15V
Output Short Circuit Duration	Continuous	Continuous	Continuous
Operating Temperature Range	−55°C to +125°C	−55°C to +125°C	0°C to +70°C
Storage Temperature Range	−65°C to +150°C	−65°C to +150°C	−65°C to +150°C
Junction Temperature	150°C	150°C	100°C
Soldering Information			
N-Package (10 seconds)	260°C	260°C	260°C
J- or H-Package (10 seconds)	300°C	300°C	300°C
M-Package			
Vapor Phase (60 seconds)	215°C	215°C	215°C
Infrared (15 seconds)	215°C	215°C	215°C

See AN-450 "Surface Mounting Methods and Their Effect on Product Reliability" for other methods of soldering

surface mount devices.

ESD Tolerance (Note 8)	400V	400V	400V

Electrical Characteristics (Note 5)

Parameter	Conditions	LM741A			LM741			LM741C			Units
		Min	Typ	Max	Min	Typ	Max	Min	Typ	Max	
Input Offset Voltage	$T_A = 25°C$										
	$R_S \leq 10\ k\Omega$					1.0	5.0		2.0	6.0	mV
	$R_S \leq 50\Omega$		0.8	3.0							mV
	$T_{AMIN} \leq T_A \leq T_{AMAX}$										
	$R_S \leq 50\Omega$			4.0							mV
	$R_S \leq 10\ k\Omega$						6.0			7.5	mV
Average Input Offset Voltage Drift				15							μV/°C
Input Offset Voltage Adjustment Range	$T_A = 25°C$, $V_S = ±20V$	±10				±15			±15		mV
Input Offset Current	$T_A = 25°C$		3.0	30		20	200		20	200	nA
	$T_{AMIN} \leq T_A \leq T_{AMAX}$			70		85	500			300	nA
Average Input Offset Current Drift				0.5							nA/°C
Input Bias Current	$T_A = 25°C$		30	80		80	500		80	500	nA
	$T_{AMIN} \leq T_A \leq T_{AMAX}$			0.210			1.5			0.8	μA
Input Resistance	$T_A = 25°C$, $V_S = ±20V$	1.0	6.0		0.3	2.0		0.3	2.0		MΩ
	$T_{AMIN} \leq T_A \leq T_{AMAX}$, $V_S = ±20V$	0.5									MΩ
Input Voltage Range	$T_A = 25°C$							±12	±13		V
	$T_{AMIN} \leq T_A \leq T_{AMAX}$				±12	±13					V

90

Electrical Characteristics (Note 5) (Continued)

Parameter	Conditions	LM741A			LM741			LM741C			Units
		Min	Typ	Max	Min	Typ	Max	Min	Typ	Max	
Large Signal Voltage Gain	$T_A = 25°C$, $R_L \geq 2$ kΩ										
	$V_S = \pm20V$, $V_O = \pm15V$	50									V/mV
	$V_S = \pm15V$, $V_O = \pm10V$				50	200		20	200		V/mV
	$T_{AMIN} \leq T_A \leq T_{AMAX}$,										
	$R_L \geq 2$ kΩ,										
	$V_S = \pm20V$, $V_O = \pm15V$	32									V/mV
	$V_S = \pm15V$, $V_O = \pm10V$				25			15			V/mV
	$V_S = \pm5V$, $V_O = \pm2V$	10									V/mV
Output Voltage Swing	$V_S = \pm20V$										
	$R_L \geq 10$ kΩ	±16									V
	$R_L \geq 2$ kΩ	±15									V
	$V_S = \pm15V$										
	$R_L \geq 10$ kΩ				±12	±14		±12	±14		V
	$R_L \geq 2$ kΩ				±10	±13		±10	±13		V
Output Short Circuit Current	$T_A = 25°C$	10	25	35		25			25		mA
	$T_{AMIN} \leq T_A \leq T_{AMAX}$	10		40							mA
Common-Mode Rejection Ratio	$T_{AMIN} \leq T_A \leq T_{AMAX}$										
	$R_S \leq 10$ kΩ, $V_{CM} = \pm12V$				70	90		70	90		dB
	$R_S \leq 50\Omega$, $V_{CM} = \pm12V$	80	95								dB
Supply Voltage Rejection Ratio	$T_{AMIN} \leq T_A \leq T_{AMAX}$,										
	$V_S = \pm20V$ to $V_S = \pm5V$										
	$R_S \leq 50\Omega$	86	96								dB
	$R_S \leq 10$ kΩ				77	96		77	96		dB
Transient Response	$T_A = 25°C$, Unity Gain										
Rise Time			0.25	0.8		0.3			0.3		μs
Overshoot			6.0	20		5			5		%
Bandwidth (Note 6)	$T_A = 25°C$	0.437	1.5								MHz
Slew Rate	$T_A = 25°C$, Unity Gain	0.3	0.7			0.5			0.5		V/μs
Supply Current	$T_A = 25°C$					1.7	2.8		1.7	2.8	mA
Power Consumption	$T_A = 25°C$										
	$V_S = \pm20V$		80	150							mW
	$V_S = \pm15V$					50	85		50	85	mW
LM741A	$V_S = \pm20V$										
	$T_A = T_{AMIN}$			165							mW
	$T_A = T_{AMAX}$			135							mW
LM741	$V_S = \pm15V$										
	$T_A = T_{AMIN}$					60	100				mW
	$T_A = T_{AMAX}$					45	75				mW

Note 2: "Absolute Maximum Ratings" indicate limits beyond which damage to the device may occur. Operating Ratings indicate conditions for which the device is functional, but do not guarantee specific performance limits.

Electrical Characteristics (Note 5) (Continued)

Note 3: For operation at elevated temperatures, these devices must be derated based on thermal resistance, and T_j max. (listed under "Absolute Maximum Ratings"). $T_j = T_A + (\theta_{jA} P_D)$.

Thermal Resistance	Cerdip (J)	DIP (N)	HO8 (H)	SO-8 (M)
θ_{jA} (Junction to Ambient)	100°C/W	100°C/W	170°C/W	195°C/W
θ_{jC} (Junction to Case)	N/A	N/A	25°C/W	N/A

Note 4: For supply voltages less than ±15V, the absolute maximum input voltage is equal to the supply voltage.

Note 5: Unless otherwise specified, these specifications apply for $V_S = \pm15V$, $-55°C \leq T_A \leq +125°C$ (LM741/LM741A). For the LM741C/LM741E, these specifications are limited to $0°C \leq T_A \leq +70°C$.

Note 6: Calculated value from: BW (MHz) = 0.35/Rise Time(µs).

Note 7: For military specifications see RETS741X for LM741 and RETS741AX for LM741A.

Note 8: Human body model, 1.5 kΩ in series with 100 pF.

Schematic Diagram
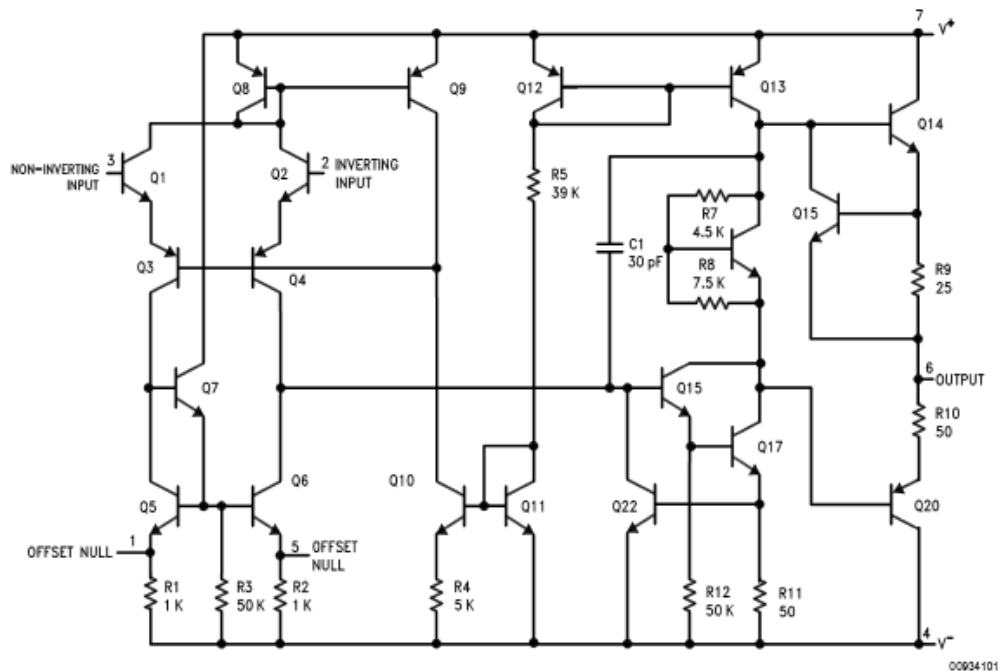
00934101

2. TL081

TL080, TL081, TL082, TL084, TL081A, TL082A, TL084A
TL081B, TL082B, TL084B, TL082Y, TL084Y
JFET-INPUT OPERATIONAL AMPLIFIERS

24 DEVICES COVER COMMERCIAL, INDUSTRIAL, AND MILITARY TEMPERATURE RANGES

- Low-Power Consumption
- Wide Common-Mode and Differential Voltage Ranges
- Low Input Bias and Offset Currents
- Output Short-Circuit Protection
- Low Total Harmonic Distortion . . . 0.003% Typ

- High Input Impedance . . . JFET-Input Stage
- Internal Frequency Compensation (Except TL080, TL080A)
- Latch-Up-Free Operation
- High Slew Rate . . . 13 V/µs Typ
- Common-Mode Input Voltage Range Includes V_{CC+}

TL080
D, P, OR PW PACKAGE
(TOP VIEW)

N1/COMP	1	8	COMP
IN–	2	7	V_{CC+}
IN+	3	6	OUT
V_{CC-}	4	5	OFFSET N2

TL081, TL081A, TL081B
D, JG, P, OR PW PACKAGE
(TOP VIEW)

OFFSET N1	1	8	NC
IN–	2	7	V_{CC+}
IN+	3	6	OUT
V_{CC-}	4	5	OFFSET N2

TL082, TL082A, TL082B
D, JG, P, OR PW PACKAGE
(TOP VIEW)

1 OUT	1	8	V_{CC+}
1 IN–	2	7	2 OUT
1 IN+	3	6	2 IN–
V_{CC-}	4	5	2 IN+

TL081M . . . FK PACKAGE
(TOP VIEW)

Pins (top): NC, OFFSET N1, NC, NC, NC (3 2 1 20 19)
NC (4)	(18) NC
IN– (5)	(17) V_{CC+}
NC (6)	(16) NC
IN+ (7)	(15) OUT
NC (8)	(14) NC
Pins (bottom): (9 10 11 12 13) NC, V_{CC-}, NC, OFFSET N2, NC

TL082M . . . FK PACKAGE
(TOP VIEW)

Pins (top): NC, 1 OUT, NC, V_{CC+}, NC (3 2 1 20 19)
NC (4)	(18) NC
1 IN– (5)	(17) 2 OUT
NC (6)	(16) NC
1 IN+ (7)	(15) 2 IN–
NC (8)	(14) NC
Pins (bottom): (9 10 11 12 13) NC, V_{CC-}, NC, 2 IN+, NC

TL084, TL084A, TL084B
D, J, N, OR PW PACKAGE
(TOP VIEW)

1 OUT	1	14	4 OUT
1 IN–	2	13	4 IN–
1 IN+	3	12	4 IN+
V_{CC+}	4	11	V_{CC-}
2 IN+	5	10	3 IN+
2 IN–	6	9	3 IN–
2 OUT	7	8	3 OUT

TL084M . . . FK PACKAGE
(TOP VIEW)

Pins (top): 1 IN–, 1 OUT, NC, 4 OUT, 4 IN– (3 2 1 20 19)
1 IN+ (4)	(18) 4 IN+
NC (5)	(17) NC
V_{CC+} (6)	(16) V_{CC-}
NC (7)	(15) NC
2 IN+ (8)	(14) 3 IN+
Pins (bottom): (9 10 11 12 13) 2 IN–, 2 OUT, NC, 3 OUT, 3 IN–

NC–No internal connection

TEXAS INSTRUMENTS

1

TL080, TL081, TL082, TL084, TL081A, TL082A, TL084A
TL081B, TL082B, TL084B, TL082Y, TL084Y
JFET-INPUT OPERATIONAL AMPLIFIERS

symbols

TL080

TL081

TL082 (each amplifier)
TL084 (each amplifier)

description

The TL08_ JFET-input operational amplifier family is designed to offer a wider selection than any previously developed operational amplifier family. Each of these JFET-input operational amplifiers incorporates well-matched, high-voltage JFET and bipolar transistors in a monolithic integrated circuit. The devices feature high slew rates, low input bias and offset currents, and low offset voltage temperature coefficient. Offset adjustment and external compensation options are available within the TL08_ family.

Device types with a C suffix are characterized for operation from 0°C to 70°C, those with an I suffix are characterized for operation from −40°C to 85°C, and those with an M suffix are characterized for operation over the full military temperature range of −55°C to 125°C.

AVAILABLE OPTIONS

T_A	V_{IO} MAX at 25°C	PACKAGE								CHIP FORM (Y)
		SMALL OUTLINE (D008)	SMALL OUTLINE (D014)	CHIP CARRIER (FK)	CERAMIC DIP (J)	CERAMIC DIP (JG)	PLASTIC DIP (N)	PLASTIC DIP (P)	TSSOP (PW)	
0°C to 70°C	15 mV	TL080CD	—	—	—	—	—	TL080CP	TL080CPW	—
	15 mV	TL081CD						TL081CP	TL081CPW	
	6 mV	TL081ACD						TL081ACP		
	3 mV	TL081BCD						TL081BCP		
	15 mV	TL082CD	—	—	—	—	—	TL082CP	TL082CPW	TL082Y
	6 mV	TL082ACD						TL082ACP		
	3 mV	TL082BCD						TL082BCP		
	15 mV		TL084CD	—	—	—	TL084CN	—	TL084CPW	TL084Y
	6 mV		TL084ACD				TL084ACN			
	3 mV		TL084BCD				TL084BCN			
−40°C to 85°C	6 mV	TL081ID		—	—	—		TL081IP	—	—
	6 mV	TL082ID						TL082IP		
	6 mV	TL084ID	TL094ID				TL084IN			
−55°C to 125°C	6 mV			TL081MFK		TL081MJG	—	—	—	—
	6 mV	—	—	TL082MFK		TL082MJG				
	9 mV			TL084MFK	TL084MJ					

The D package is available taped and reeled. Add R suffix to device type, (e.g., TL080CDR).

2

94

schematic (each amplifier)
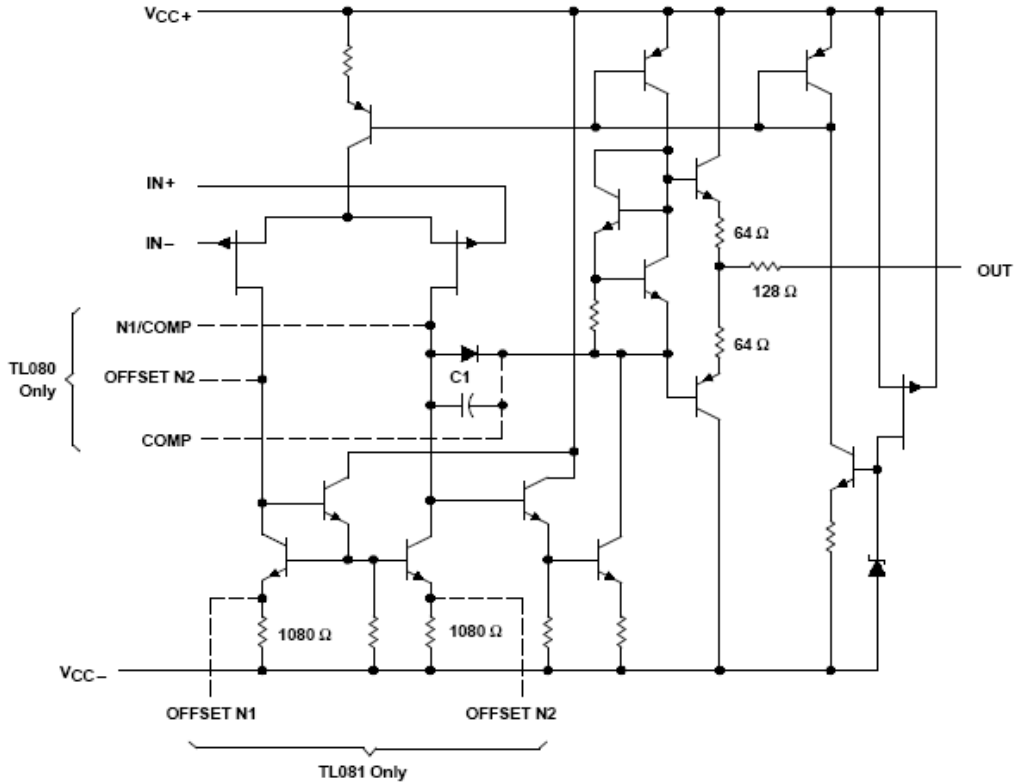
C1 = 18 pF on TL081, TL082, and TL084 only (including their suffix versions).
Component values shown are nominal.

chip information

These chips, when properly assembled, display characteristics similar to the TL084. Thermal compression or ultrasonic bonding may be used on the doped aluminum bonding pads. Chips may be mounted with conductive epoxy or a gold-silicon preform.

BONDING PAD ASSIGNMENTS

CHIP THICKNESS: 15 TYPICAL

BONDING PADS: 4 × 4 MINIMUM

$T_J$max = 150°C

TOLERANCES ARE ±10%

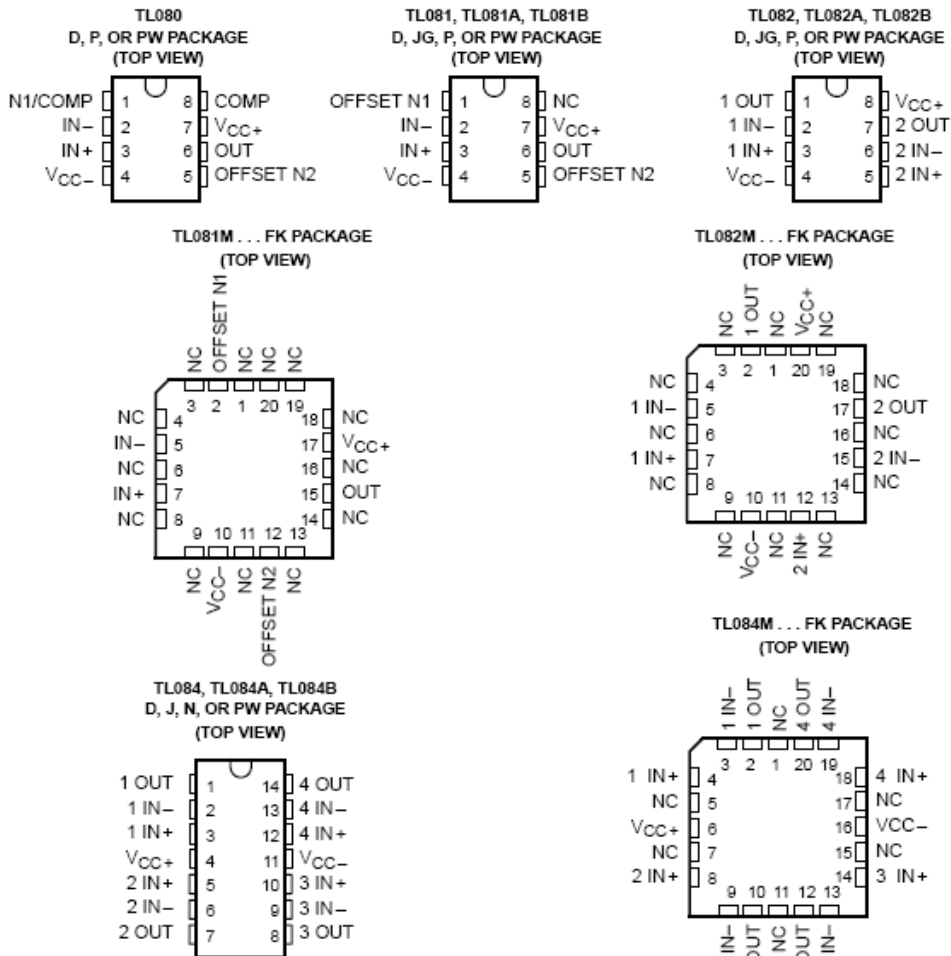ALL DIMENSIONS ARE IN MILS

PIN (11) INTERNALLY CONNECTED
TO BACKSIDE OF CHIP
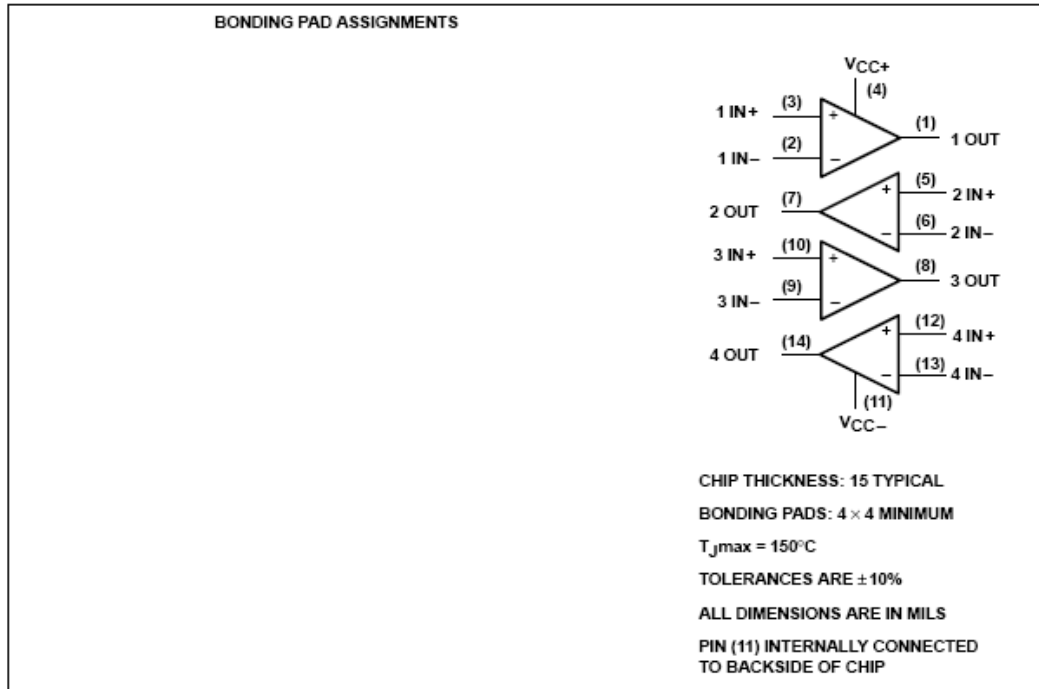
TL080, TL081, TL082, TL084, TL081A, TL082A, TL084A
TL081B, TL082B, TL084B
JFET-INPUT OPERATIONAL AMPLIFIERS
SLOS081A–D2297, FEBRUARY 1977–REVISED NOVEMBER 1992

absolute maximum ratings over operating free-air temperature range (unless otherwise noted)

		TL08_C TL08_AC TL08_BC	TL08_I	TL08_M	UNIT
Supply voltage, $V_{CC}+$ (see Note 1)		18	18	18	V
Supply voltage $V_{CC}-$ (see Note 1)		−18	−18	−18	V
Differential input voltage (see Note 2)		±30	±30	±30	V
Input voltage (see Notes 1 and 3)		±15	±15	±15	V
Duration of output short circuit (see Note 4)		unlimited	unlimited	unlimited	
Continuous total dissipation		See Dissipation Rating Table			
Operating free-air temperature range		0 to 70	−40 to 85	−55 to 125	°C
Storage temperature range		−65 to 150	−65 to 150	−65 to 150	°C
Case temperature for 60 seconds	FK package			260	°C
Lead temperature 1,6 mm (1/16 inch) from case for 60 seconds	J or JG package			300	°C
Lead temperature 1,6 mm (1/16 inch) from case for 10 seconds	D, N, P, or PW package	260	260		°C

NOTES: 1. All voltage values, except differential voltages, are with respect to the midpoint between $V_{CC}+$ and $V_{CC}-$.
2. Differential voltages are at the noninverting input terminal with respect to the inverting input terminal.
3. The magnitude of the input voltage must never exceed the magnitude of the supply voltage or 15 V, whichever is less.
4. The output may be shorted to ground or to either supply. Temperature and/or supply voltages must be limited to ensure that the dissipation rating is not exceeded.

DISSIPATION RATING TABLE

PACKAGE	$T_A \leq 25°C$ POWER RATING	DERATING FACTOR	DERATE ABOVE T_A	$T_A = 70°C$ POWER RATING	$T_A = 85°C$ POWER RATING	$T_A = 125°C$ POWER RATING
D (8 Pin)	680 mW	5.8 mW/°C	32°C	464 mW	377 mW	N/A
D (14 Pin)	680 mW	7.6 mW/°C	60°C	608 mW	494 mW	N/A
FK	680 mW	11.0 mW/°C	88°C	680 mW	680 mW	275 mW
J	680 mW	11.0 mW/°C	88°C	680 mW	680 mW	275 mW
JG	680 mW	8.4 mW/°C	69°C	672 mW	546 mW	210 mW
N	680 mW	9.2 mW/°C	76°C	680 mW	598 mW	N/A
P	680 mW	8.0 mW/°C	65°C	640 mW	520 mW	N/A
PW (8 Pin)	525 mW	4.2 mW/°C	25°C	336 mW	N/A	N/A
PW (14 Pin)	700 mW	5.6 mW/°C	25°C	448 mW	N/A	N/A

6

97

electrical characteristics, $V_{CC\pm}$ = ±15 V (unless otherwise noted)

PARAMETER		TEST CONDITIONS†	TL080C TL081C TL082C TL084C			TL081AC TL082AC TL084AC			TL081BC TL082BC TL084BC			TL081 TL082I TL084I			UNIT
			MIN	TYP	MAX	MIN	TYP	MAX	MIN	TYP	MAX	MIN	TYP	MAX	
V_{IO}	Input offset voltage	$V_O = 0$, $R_S = 50\ \Omega$, $T_A = 25°C$		3	15		3	6		2	3		3	6	mV
		$R_S = 50\ \Omega$, T_A = full range			20			7.5			5			9	
α_{VIO}	Temperature coefficient of input offset voltage	$V_O = 0$, $R_S = 50\ \Omega$, T_A = full range		18			18			18			18		μV/°C
I_{IO}	Input offset current‡	$V_O = 0$, $T_A = 25°C$		5	200		5	100		5	100		5	100	pA
		T_A = full range			2			2			2			10	nA
I_{IB}	Input bias current‡	$V_O = 0$, $T_A = 25°C$		30	400		30	200		30	200		30	200	pA
		T_A = full range			10			7			7			20	nA
V_{ICR}	Common-mode input voltage range	$T_A = 25°C$	±11	-12 to 15		±11	-12 to 15		±11	-12 to 15		±11	-12 to 15		V
V_{OM}	Maximum peak output voltage swing	$R_L = 10\ k\Omega$, $T_A = 25°C$	±12	±13.5		±12	±13.5		±12	±13.5		±12	±13.5		V
		$R_L \geq 10\ k\Omega$, T_A = full range	±12			±12			±12			±12			
		$R_L \geq 2\ k\Omega$	±10	±12		±10	±12		±10	±12		±10	±12		
A_{VD}	Large-signal differential voltage amplification	$V_O = \pm10\ V$, $R_L \geq 2\ k\Omega$, $T_A = 25°C$	25	200		50	200		50	200		50	200		V/mV
		$V_O = \pm10\ V$, $R_L \geq 2\ k\Omega$, T_A = full range	15			25			25			25			
B_1	Unity-gain bandwidth	$T_A = 25°C$		3			3			3			3		MHz
r_i	Input resistance	$T_A = 25°C$		10^{12}			10^{12}			10^{12}			10^{12}		Ω
CMRR	Common-mode rejection ratio	$V_{IC} = V_{ICR}$ min, $V_O = 0$, $R_S = 50\ \Omega$, $T_A = 25°C$	70	86		80	86		80	86		80	86		dB
k_{SVR}	Supply voltage rejection ratio ($\Delta V_{CC\pm} / \Delta V_{IO}$)	$V_{CC\pm} = \pm15\ V$ to $\pm9\ V$, $V_O = 0$, $R_S = 50\ \Omega$, $T_A = 25°C$	70	86		80	86		80	86		80	86		dB
I_{CC}	Supply current (per amplifier)	No load, $V_O = 0$, $T_A = 25°C$		1.4	2.8		1.4	2.8		1.4	2.8		1.4	2.8	mA
V_{O1}/V_{O2}	Crosstalk attenuation	$A_{VD} = 100$, $T_A = 25°C$		120			120			120			120		dB

† All characteristics are measured under open-loop conditions with zero common-mode voltage unless otherwise specified. Full range for T_A is 0°C to 70°C for TL08_C, TL08_AC, TL08_BC and –40°C to 85°C for TL08_I.

‡ Input bias currents of a FET-input operational amplifier are normal junction reverse currents, which are temperature sensitive as shown in Figure 18. Pulse techniques must be used that will maintain the junction temperature as close to the ambient temperature as possible.

3. CD4007

FAIRCHILD

SEMICONDUCTOR™

October 1987
Revised January 1999

CD4007C
Dual Complementary Pair Plus Inverter

General Description

The CD4007C consists of three complementary pairs of N- and P-channel enhancement mode MOS transistors suitable for series/shunt applications. All inputs are protected from static discharge by diode clamps to V_{DD} and V_{SS}.

For proper operation the voltages at all pins must be constrained to be between $V_{SS} - 0.3V$ and $V_{DD} + 0.3V$ at all times.

Features

- Wide supply voltage range: 3.0V to 15V
- High noise immunity: 0.45 V_{CC} (typ.)

Ordering Code:

Order Number	Package Number	Package Description
CD4007CM	M14A	14-Lead Small Outline Integrated Circuit (SOIC), JEDEC MS-120, 0.150" Narrow
CD4007CN	N14A	14-Lead Plastic Dual-In-Line Package (PDIP), JEDEC MS–001, 0.300" Wide

Devices also available in Tape and Reel. Specify by appending the suffix letter "X" to the ordering code.

Connection Diagram

Pin Assignments for DIP and SOIC
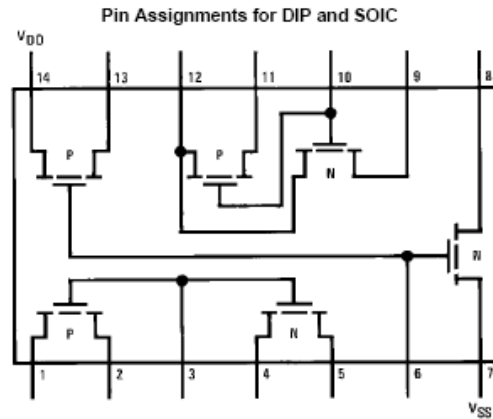
Note: All P-channel substrates are connected to V_{DD} and all N-channel substrates are connected to V_{SS}.

Top View

www.fairchildsemi.com

Absolute Maximum Ratings (Note 1)

Voltage at Any Pin	V_{SS} −0.3V to V_{DD} +0.3V
Operating Temperature Range	−40°C to +85°C
Storage Temperature Range	−65°C to +150°C
Power Dissipation (P_D)	
Dual-In-Line	700 mW
Small Outline	500 mW

Operating V_{DD} Range	V_{SS} +3.0V to V_{SS} +15V
Lead Temperature	
(Soldering, 10 seconds)	260°C

Note 1: This device should not be connected to circuits with the power on because high transient voltages may cause permanent damage.

DC Electrical Characteristics

Symbol	Parameter	Conditions	Limits									Units
			−40°C			+25°C			+85°C			
			Min	Typ	Max	Min	Typ	Max	Min	Typ	Max	
I_L	Quiescent Device	V_{DD} = 5.0V			0.5		0.005	0.05			15	μA
	Current	V_{DD} = 10V			1.0		0.005	1.0			30	μA
P_D	Quiescent Device	V_{DD} = 5.0V			2.5		0.025	2.5			75	μW
	Dissipation Package	V_{DD} = 10V			10		0.05	10			300	μW
V_{OL}	Output Voltage	V_{DD} = 5.0V			0.05		0	0.01			0.05	V
	LOW Level	V_{DD} = 10V			0.05		0	0.01			0.05	V
V_{OH}	Output Voltage	V_{DD} = 5.0V	4.95			4.95	5.0		4.95			V
	HIGH Level	V_{DD} = 10V	9.95			9.95	10		9.95			V
V_{NL}	Noise Immunity	V_{DD} = 5.0V, V_O = 3.6V			1.5		2.25	1.5			1.4	V
	(All inputs)	V_{DD} = 10V, V_O = 7.2V			3.0		4.5	3.0			2.9	V
V_{NH}	Noise Immunity	V_{DD} = 5.0V, V_O = 0.95V	3.6			3.5	2.25		3.5			V
	(All Inputs)	V_{DD} = 10V, V_O = 2.9V	7.1			7.0	4.5		7.0			V
$I_D N$	Output Drive Current	V_{DD} = 5.0V, V_O = 0.4V, V_I = V_{DD}	0.35			0.3	1.0		0.24			mA
	N-Channel	V_{DD} = 10V, V_O = 0.5V, V_I = V_{DD}	1.2			1.0	2.5		0.8			mA
$I_D P$	Output Drive Current	V_{DD} = 5.0V, V_O = 2.5V, V_I = V_{SS}	−1.3			−1.1	−4.0		−0.9			mA
	P-Channel	V_{DD} = 10V, V_O = 9.5V, V_I = V_{SS}	−0.65			−0.55	−2.5		−0.45			mA
I_I	Input Current						10					pA

AC Electrical Characteristics (Note 2)

T_A = 25°C and C_L = 15 pF and rise and fall times = 20 ns. Typical temperature coefficient for all values of V_{DD} = 0.3%/°C

Symbol	Parameter	Conditions	Min	Typ	Max	Units
t_{PLH} = t_{PHL}	Propagation Delay Time	V_{DD} = 5.0V		35	75	ns
		V_{DD} = 10V		20	50	ns
t_{TLH} = t_{THL}	Transition Time	V_{DD} = 5.0V		50	100	ns
		V_{DD} = 10V		30	50	ns
C_I	Input Capacitance	Any Input		5		pF

Note 2: AC Parameters are guaranteed by DC correlated testing.

100

AC Test Circuits
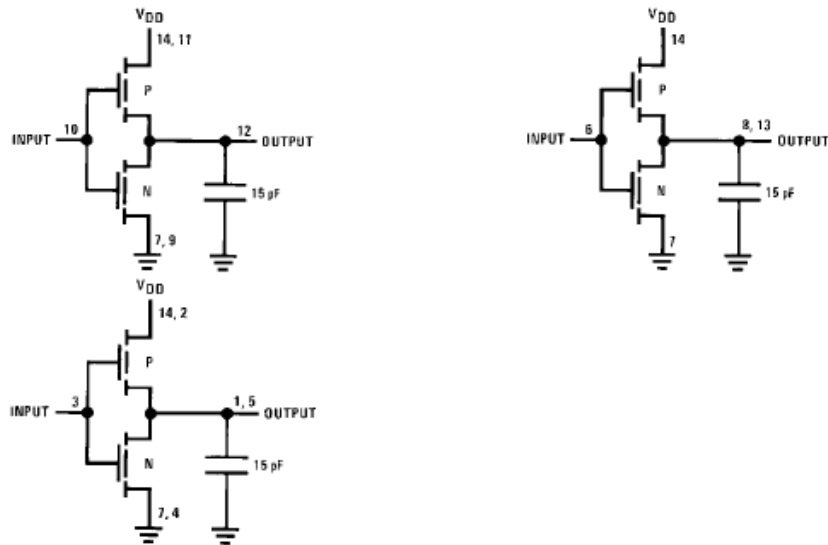
Switching Time Waveforms

101
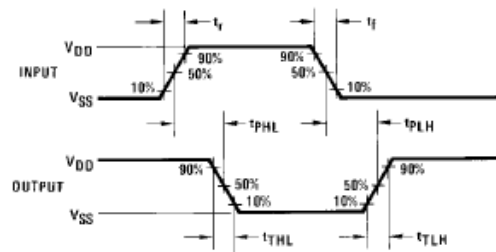
Appendix I – Measurement Computing 1608FS DAQ

Specifications

USB-1608FS

Specifications

Typical for 25 °C unless otherwise specified.
Specifications in *italic text* are guaranteed by design.

Analog input section

Table 1. Analog input specifications

Parameter	Conditions	Specification
A/D converter type		16-bit successive Approximation type
Number of channels		8 single-ended
Input configuration		Individual A/D per channel
Sampling method		Simultaneous
Absolute maximum input voltage	*CHx IN to GND.*	*±15 V max*
Input impedance		100 MOhm, min
Input ranges	Software selectable	±10 V, ±5 V, ±2 V, ±1 V
Sampling rate	Scan to PC memory	0.6 S/s to 50 kS/s, software programmable
	Burst scan to 32 k sample FIFO	20 S/s to 50 kS/s, software programmable
Throughput	Software paced	500 S/s all channels
	Scan to PC memory (Note 1)	= (100 kS/s) / (# of channels), max of 50 kS/s for any channel
	Burst scan to 32 k sample FIFO	= (200 kS/s) / (# of channels), max of 50 kS/s for any channel
Gain queue		Software configurable. Eight elements, one gain element per channel.
Resolution		16 bits
No missing codes		*15 bits*
Crosstalk	Signal DC-25 KHz	-80 dB
CAL output	User calibration source	0.625 V, 1.25 V, 2.5 V, 5.0 V, software selectable
CAL output accuracy (Note 2)		±0.5% typ, ±1.0% max
CAL current		±5 mA max
Trigger source	Software selectable	External digital: TRIG_IN

Note 1: Maximum throughput scanning to PC memory is machine dependent. While the majority of XP equipped PC's we tested allowed acquisition at the maximum rates, a few would not. The lowest maximum rate we observed on an XP equipped PC during multi-channel testing was 95 kS/s, aggregate. The rates specified are for Windows XP only. Maximum rates on operating systems that predate XP may be less and must be determined through testing on your machine.

Note 2: Actual values used for calibration are measured and stored in EEPROM.

Table 2. Calibrated absolute accuracy

Range	Accuracy (mV)
±10 V	5.66
±5 V	2.98
±2 V	1.31
±1 V	0.68

Table 3. Accuracy components - All values are (±)

Range	% of Reading	Gain error at FS (mV)	Offset (mV)
±10 V	0.04	4.00	1.66
±5 V	0.04	2.00	0.98
±2 V	0.04	0.80	0.51
±1 V	0.04	0.40	0.28

Table 4 summarizes the noise performance for the USB-1608FS. Noise distribution is determined by gathering 50 K samples with inputs tied to ground at the user connector. Samples are gathered at the maximum specified sampling rate of 50 kS/s.

Table 4. Noise performance

Range	Typical counts	LSBrms
±10 V	10	1.52
±5 V	10	1.52
±2 V	11	1.67
±1 V	14	2.12

Digital input/output

Table 5. Digital I/O specifications

Digital type	CMOS
Number of I/O	8 (DIO0 through DIO7)
Configuration	Independently configured for input or output
Pull-up/pull-down configuration	All pins pulled up to Vs via 47 K resistors (default). Positions available for pull down to ground. Hardware selectable via zero ohm resistors as a factory option.
Input high voltage	2.0 V min, 5.5 V absolute max
Input low voltage	0.8 V max, −0.5 V absolute min
Output high voltage (IOH = −2.5 mA)	3.8 V min
Output low voltage (IOL = 2.5 mA)	0.7 V max
Power on and reset state	Input

External trigger

Table 6. External trigger specifications

Parameter	Conditions	Specification
Trigger source (Note 3)	External digital	TRIG_IN
Trigger mode	Software selectable	Edge sensitive: user configurable for CMOS compatible rising or falling edge.
Trigger latency		10 µs max
Trigger pulse width		1µs min
Input high voltage		4.0 V min, 5.5 V absolute max
Input low voltage		1.0 V max, −0.5 V absolute min
Input leakage current		*±1.0µA*

Note 3:   TRIG_IN is a Schmitt trigger input protected with a 1.5K Ohm series resistor.

External clock input/output

Table 7. External clock I/O specifications

Parameter	Conditions	Specification
Pin name		SYNC
Pin type		Bidirectional
Software selectable direction	Output	Outputs internal A/D pacer clock.
	Input	Receives A/D pacer clock from external source.
Input clock rate		50 kHz, maximum
Clock pulse width	Input	1µs min
	Output	5µs min
Input leakage current		*±1.0µA*
Input high voltage		4.0 V min, 5.5 V absolute max
Input low voltage		1.0 V max, −0.5 V absolute min
Output high voltage (Note 4)	IOH = −2.5 mA	3.3 V min
	No load	3.8 V min
Output low voltage (Note 4)	IOL = 2.5 mA	1.1 V max
	No Load	0.6 V max

Note 4: SYNC is a Schmitt trigger input and is over-current protected with a 200 Ohm series resistor.

Counter section

Table 8. Counter specifications

Pin name (Note 5)	CTR
Counter type	Event counter
Number of channels	1
Input type	TTL, rising edge triggered
Input source	CTR screw terminal
Resolution	32 bits
Schmidt trigger hysteresis	*20 mV to 100 mV*
Input leakage current	*±1µA*
Maximum input frequency	1 MHz
High pulse width	*500 ns min*
Low pulse width	*500 ns min*
Input high voltage	4.0 V min, 5.5 V absolute max
Input low voltage	1.0 V max, −0.5 V absolute min

Note 5: CTR is a Schmitt trigger input protected with a 1.5K Ohm series resistor.

Memory

Table 9. Memory specifications

Data FIFO	32,768 samples, 65,536 bytes		
EEPROM	1,024 bytes		
EEPROM configuration	Address range	Access	Description
	0x000-0x07F	Reserved	128 bytes system data
	0x080-0x1FF	Read/write	384 bytes cal data
	0x200-0x3FF	Read/write	512 bytes user area

Microcontroller

Table 10. Microcontroller specifications

Type	High performance 8-bit RISC microcontroller
Program memory	16,384 words
Data memory	2,048 bytes

Power

Parameter	Conditions	Specification
Supply current	USB enumeration	< 100 mA
Supply current (Note 6)	Continuous mode	150 mA
+5 V USB power available (Note 7)	▪ Connected to self-powered hub ▪ Connected to externally-powered root port hub	4.5 V min, 5.25 V max
Output current (Note 8)		350 mA max

Note 6: This is the total current requirement for the USB-1608FS which includes up to 10 mA for the status LED.

Note 7: "Self-powered hub" refers to a USB hub with an external power supply. Self-powered hubs allow a connected USB device to draw up to 500 mA. "Root port hubs" reside in the PC's USB host Controller. The USB port(s) on your PC are root port hubs. All externally-powered root port hubs (desktop PC's) provide up to 500 mA of current for a USB device. Battery-powered root port hubs provide 100 mA or 500 mA, depending upon the manufacturer. A laptop PC that is not connected to an external power adapter is an example of a battery-powered root port hub. If your laptop PC is constrained to the 100 mA maximum, you need to purchase a self-powered hub.

Note 8: This refers to the total amount of current that can be sourced from the USB +5 V and digital outputs.

General

Device type	USB 2.0 (full-speed)
Device compatibility	USB 1.1, USB 2.0

Environmental

Operating temperature range	0 to 70 °C
Storage temperature range	-40 to 70 °C
Humidity	0 to 90% non-condensing

Mechanical

Dimensions	79 mm (L) x 82 mm (W) x 25 mm (H)
USB cable length	3 meters max
User connection length	3 meters max

Main connector and pin out

Connector type	Screw terminal
Wire gauge range	16 AWG to 30 AWG

Pin	Signal Name	Pin	Signal Name
1	CH0 IN	21	DIO0
2	AGND	22	GND
3	CH1 IN	23	DIO1
4	AGND	24	GND
5	CH2 IN	25	DIO2
6	AGND	26	GND
7	CH3 IN	27	DIO3
8	AGND	28	GND
9	CH4 IN	29	DIO4
10	AGND	30	GND
11	CH5 IN	31	DIO5
12	AGND	32	GND
13	CH6 IN	33	DIO6
14	AGND	34	GND
15	CH7 IN	35	DIO7
16	AGND	36	SYNC
17	CAL	37	TRIG IN
18	AGND	38	CTR
19	AGND	39	PC +5V
20	AGND	40	GND

Appendix J – Agilent MSO6012A Oscilloscope

lab scope performance
at a
portable scope price
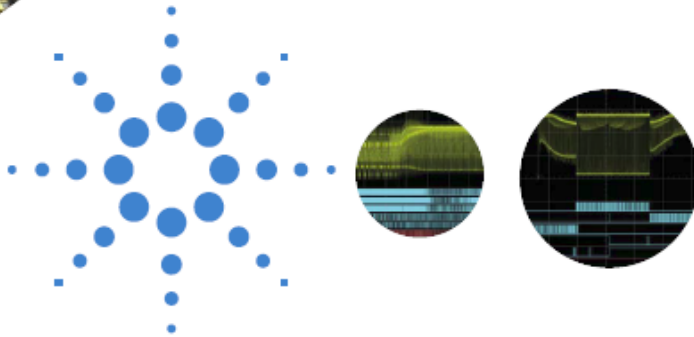
**Agilent Technologies
6000 Series Oscilloscopes**

Data Sheet

*Get superior insight into your design
challenges with integrated analog,
digital and serial test.*

Agilent Technologies

Performance characteristics

Acquisition: scope channels

Sample rate	MSO/DSO601xA/603xA: 2 GSa/sec each channel MSO/DSO605xA/610xA: 4 GSa/sec half channel*, 2 GSa/sec each channel Equivalent-time sample rate: 400 GSa/s (when real-time mode is turned off)

Standard 2 Mpts memory depth	With logic channels turned off,
	  2 Mpts half channel*, 1 Mpts full channel
	With logic channels turned on,
	  1.25 Mpts half channel*, 625 kpts full channel

Optional 8 Mpts memory depth	With logic channels turned off,
	  Option 8ML or 8MH – 8 Mpts half channel*, 4 Mpts each channel
	With logic channels turned on,
	  Option 8ML or 8MH – 5 Mpts half channel*, 2.5 Mpts each channel

Vertical resolution	8 bits
Peak detection	MSO/DSO601xA: 1-ns peak detect MSO/DSO603xA: 500-ps peak detect MSO/DSO605xA/610xA: 250-ps peak detect
Averaging	Selectable from 2, 4, 8, 16, 32, 64 ... to 65536
High resolution mode	Average mode with avg = 1 12 bits of resolution when $\geq$10 µs/div @ 4 GSa/s or $\geq$20-µs/div @ 2 GSa/s
Filter	Sinx/x interpolation (single shot BW = sample rate/4 or bandwidth of scope, whichever is less) with vectors on and in real-time mode

Acquisition: logic channels (MSO6000A or MSO-upgraded DSO6000A only)

Sample rate	2 GSa/sec one pod, 1 GSa/sec each pod
Maximum input frequency	250 MHz

Standard 2 Mpts memory depth	With scope channels turned off,
	  2 Mpts one pod, 1 Mpts each pod
	With scope channels turned on,
	  625 kpts one pod, 312 kpts each pod

Optional 8 Mpts memory depth	With scope channels turned off,
	  Option 8ML or 8MH – 8 Mpts one pod, 4 Mpts each pod
	With scope channels turned on,
	  Option 8ML or 8MH – 2.5 Mpts one pod, 1.25 Mpts each pod

Vertical resolution	1 bit
Glitch detection	2 ns (min pulse width)

* Half channel is when only one of channel 1 or 2 is turned on, and only channel 3 or 4 is turned on.

109

Performance characteristics (continued)

Vertical system: scope channels

Scope channels	MSO/DSO6xx2A: Ch 1 and 2 simultaneous acquisition MSO/DSO6xx4A: Ch 1, 2, 3 and 4 simultaneous acquisition
Bandwidth (–3dB)*	MSO/DSO601xA: DC to 100 MHz MSO/DSO603xA: DC to 300 MHz MSO/DSO605xA: DC to 500 MHz MSO/DSO610xA: DC to 1 GHz
AC coupled	MSO/DSO601xA: 3.5 Hz to 100 MHz MSO/DSO603xA: 3.5 Hz to 300 MHz MSO/DSO605xA: 3.5 Hz to 500 MHz MSO/DSO610xA: 3.5 Hz to 1 GHz
Calculated rise time (=0.35/bandwidth)	MSO/DSO601xA: 3.5 nsec MSO/DSO603xA: 1.17 nsec MSO/DSO605xA: 700 psec MSO/DSO610xA: 350 psec
Single-shot bandwidth	MSO/DSO601xA: 100 MHz MSO/DSO603xA: 300 MHz MSO/DSO605xA: 500 MHz MSO/DSO610xA: 1 GHz (in half-channel mode)
Range[1]	MSO/DSO601xA: 1 mV/div to 5 V/div (1 MΩ) MSO/DSO603xA and MSO/DSO605xA: 2 mV/div to 5 V/div (1 MΩ or 50 Ω) MSO/DSO610xA: 2 mV/div to 5 V/div (1 MΩ), 2 mV/div to 1 V/div (50 Ω)
Maximum input	CAT I 300 Vrms, 400 Vpk; transient overvoltage 1.6 kVpk CAT II 100 Vrms, 400 Vpk With 10073C or 10074C 10:1 probe: CAT I 500 Vpk, CAT II 400 Vpk
Offset range	±5 V on ranges <10 mV/div; ±20 V on ranges 10 mV/div to 200 mV/div; ±75 V on ranges >200 mV/div
Dynamic range	±8 div
Input impedance	MSO/DSO601xA: 1 MΩ ± 1% || 11 pF MSO/DSO603xA/605xA/610xA: 1 MΩ ± 1% || 14 pF or 50 Ω ± 1.5%, selectable
Coupling	AC, DC
BW limit	MSO/DSO601xA: 20 MHz selectable MSO/DSO603xA/605xA/610xA: 25 MHz selectable
Channel-to-channel isolation	DC to max bandwidth >40 dB
Standard probes	MSO/DSO601xA: 10:1 10074C shipped standard for each scope channel MSO/DSO603xA/605xA/610xA: 10:1 10073C shipped standard for each scope channel
Probe ID	MSO/DSO601xA: Auto probe sense MSO/DSO603xA/605xA/610xA: Auto probe sense and AutoProbe interface Agilent- and Tektronix-compatible passive probe sense

* Denotes warranted specifications, all others are typical. Specifications are valid after a 30-minute warm-up period and ±10 °C from firmware calibration temperature.

1 1 mV/div is a magnification of 2 mV/div setting for 100 MHz models and 2 mV/div is a magnification of 4 mV/div setting for 300 MHz to 1 GHz models. For vertical accuracy calculations, use full scale of 16 mV for 1 mV/div sensitivity setting and 32 mV for 2 mV/div sensitivity setting.

Performance characteristics (continued)

Vertical system: scope channels (continued)

ESD tolerance	±2 kV
Noise peak-to-peak	MSO/DSO601xA: 3% full scale or 2 mV, whichever is greater MSO/DSO603xA: 3% full scale or 3 mV, whichever is greater MSO/DSO605xA: 3% full scale or 3.6 mV, whichever is greater MSO/DSO610xA: 3% full scale or 4 mV, whichever is greater
DC vertical gain accuracy*[1]	±2.0% full scale
DC vertical offset accuracy	≤200 mV/div: ±0.1 div ±2.0 mV ±0.5% offset value; >200 mV/div: ±0.1 div ±2.0 mV ±1.5% offset value
Single cursor accuracy[1]	±{DC vertical gain accuracy + DC vertical offset accuracy + 0.2% full scale (~1/2 LSB)} *Example*: for 50 mV signal, scope set to 10 mV/div (80 mV full scale), 5 mV offset, accuracy = ±{2.0% (80 mV) + 0.1 (10 mV) + 2.0 mV + 0.5% (5 mV) + 0.2% (80 mV)} = ± 4.785 mV
Dual cursor accuracy*[1]	±{DC vertical gain accuracy + 0.4% full scale (~1 LSB)} *Example*: for 50 mV signal, scope set to 10 mV/div (80 mV full scale), 5 mV offset, accuracy = ±{2.0% (80 mV) + 0.4% (80 mV)} = ±1.92 mV

* Denotes warranted specifications, all others are typical. Specifications are valid after a 30-minute warm-up period and ±10 °C from firmware calibration temperature.

1 1 mV/div is a magnification of 2 mV/div setting for 100 MHz models and 2 mV/div is a magnification of 4 mV/div setting for 300 MHz to 1 GHz models. For vertical accuracy calculations, use full scale of 16 mV for 1 mV/div sensitivity setting and 32 mV for 2 mV/div sensitivity setting.

Vertical system: logic channels (MSO6000A or MSO-upgraded DSO6000A only)

Number of channels	16 logic timing channels — labeled D15 - D0
Threshold groupings	Pod 1: D7 - D0 Pod 2: D15 - D8
Threshold selections	TTL, CMOS, ECL and user-definable (selectable by pod)
User-defined threshold range	±8.0 V in 10 mV increments
Maximum input voltage	±40 V peak CAT I; transient overvoltage 800 Vpk
Threshold accuracy*	±(100 mV + 3% of threshold setting)
Input dynamic range	±10 V about threshold
Minimum input voltage swing	500 mV peak-to-peak
Input capacitance	~8 pF
Input resistance	100 kΩ ±2% at probe tip
Channel-to-channel skew	2 ns typical, 3 ns maximum

* Denotes warranted specifications, all others are typical. Specifications are valid after a 30-minute warm-up period and ±10 °C from firmware calibration temperature.

Performance characteristics (continued)

Horizontal

Range	MSO/DSO601xA: 5 nsec/div to 50 sec/div MSO/DSO603xA: 2 nsec/div to 50 sec/div MSO/DSO605xA: 1 nsec/div to 50 sec/div MSO/DSO610xA: 500 psec/div to 50 sec/div
Resolution	2.5 psec
Time base accuracy	15 ppm (±0.0015%)
Vernier	1-2-5 increments when off, ~25 minor increments between major settings when on
Delay range	Pre-trigger (negative delay): Greater of 1 screen width or 1 ms (with 8 Mpts memory option) Greater of 1 screen width or 250 μs (with 2 Mpts memory option) Greater of 1 screen width or 125 μs (with standard memory) Post-trigger (positive delay): 1 s to 500 seconds
Analog delta-t accuracy	Same channel: ±0.0015% reading ±0.1% screen width ±20 ps Channel-to-channel: ±0.0015% reading ±0.1% screen width ±40 ps *Same channel example (MSO/DSO605xA):* For signal with pulse width of 10 μs, scope set to 5 μs/div (50 μs screen width), delta-t accuracy = ±{0.0015% (10 μs) + 0.1% (50 μs) + 20 ps} = 50.17 ns
Logic delta-t accuracy	Same channel: ±0.005% reading ±0.1% screen width ±(1 logic sample period, 1 ns) Channel-to-channel: ±0.005% reading ±0.1% screen width ±(1 logic sample period) ±chan-to-chan *skew* *Same channel example:* For signal with pulse width of 10 μs, scope set to 5 μs/div (50 μs screen width), delta-t accuracy = ±{0.005% (10 μs) + 0.1% (50 μs) + 1 ns} = 51.5 ns
Modes	Main, delayed, roll, XY
XY	Bandwidth: Max bandwidth Phase error @ 1 MHz: <0.5 degrees Z Blanking: 1.4 V blanks trace (use external trigger on MSO/DSO6xx2A, channel 4 on MSO/DSO6xx4A)
Reference positions	Left, center, right

Trigger system

Sources	MSO6xx2A: Ch 1, 2, line, ext, D15 - D0 DSO6xx2A: Ch 1, 2, line, ext MSO6xx4A: Ch 1, 2, 3, 4, line, ext, D15 - D0 DSO6xx4A: Ch 1, 2, 3, 4, line, ext
Modes	Auto, Normal (triggered), single
Holdoff time	~60 ns to 10 seconds
Trigger jitter	15 ps rms

112

Appendix K – MATLAB DAQ Toolbox
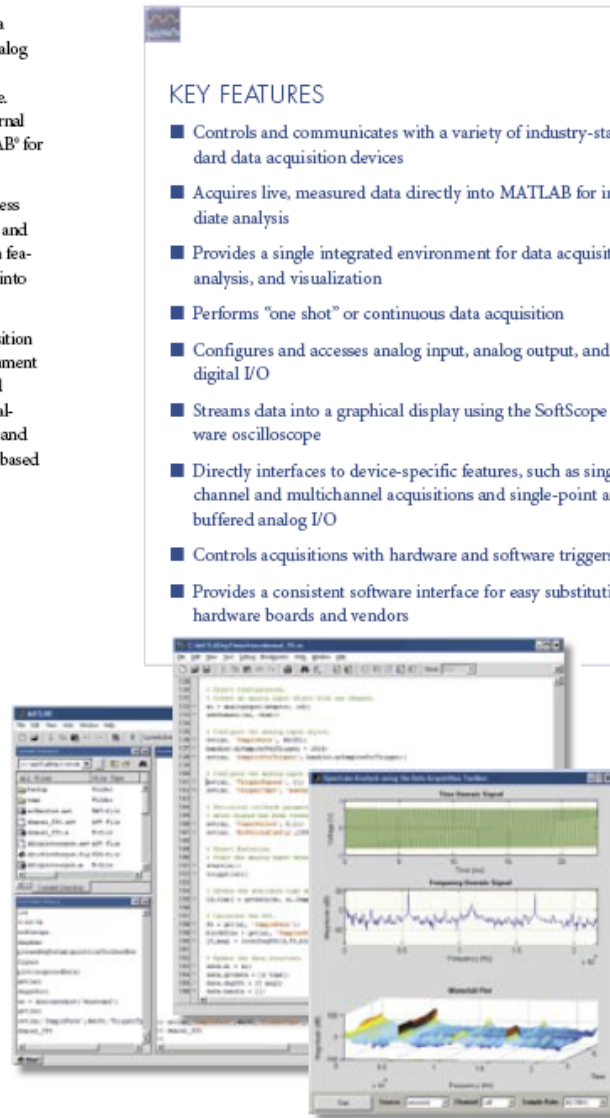
Data Acquisition Toolbox 2.8

Acquire and send out data from plug-in data acquisition boards

The Data Acquisition Toolbox provides a complete set of tools for analog input, analog output, and digital I/O from a variety of PC-compatible data acquisition hardware. The toolbox lets you configure your external hardware devices, read data into MATLAB® for immediate analysis, and send out data.

You can customize your acquisitions, access the built-in features of hardware devices, and incorporate the analysis and visualization features of MATLAB and related toolboxes into your design.

Together, MATLAB and the Data Acquisition Toolbox offer a single, integrated environment to support the entire data acquisition and analysis process. You can analyze or visualize your data, save it for post-processing, and make iterative updates to your test setup based on your analysis results.

KEY FEATURES

- Controls and communicates with a variety of industry-standard data acquisition devices
- Acquires live, measured data directly into MATLAB for immediate analysis
- Provides a single integrated environment for data acquisition, analysis, and visualization
- Performs "one shot" or continuous data acquisition
- Configures and accesses analog input, analog output, and digital I/O
- Streams data into a graphical display using the SoftScope software oscilloscope
- Directly interfaces to device-specific features, such as single-channel and multichannel acquisitions and single-point and buffered analog I/O
- Controls acquisitions with hardware and software triggers
- Provides a consistent software interface for easy substitution of hardware boards and vendors

Using the Data Acquisition Toolbox to acquire an input signal from a data acquisition board directly into MATLAB. The acquired data is displayed simultaneously as a time-domain signal, an instantaneous FFT, and a waterfall plot, making use of MATLAB signal processing and visualization capabilities.

The MathWorks

www.mathworks.com

113

INDEPENDENT ACQUISITION AND ANALYSIS

While the Data Acquisition Toolbox is collecting data, MATLAB can analyze and visualize data.

The Data Acquisition Toolbox supports three device objects: analog input, analog output, and digital I/O. The toolbox automatically performs A/D and D/A data conversions for receiving or sending data.

Supported Hardware Devices and Vendors

The Data Acquisition Toolbox supports PC-compatible data acquisition hardware from multiple vendors, including Advantech, Measurement Computing, and National Instruments, as well as Microsoft Windows compatible sound cards and the PC parallel port. The Data Acquisition Toolbox is also compatible with hardware from several data acquisition vendors via third-party adaptors.

For up-to-date information on supported third-party boards, visit www.mathworks.com/products/daq.

Communicating with Unsupported Devices

The Data Acquisition Toolbox provides an adaptor kit that enables you to build custom interfaces to hardware not supported by the toolbox. For more information, refer to the Data Acquisition Toolbox documentation.

Working with the Data Acquisition Toolbox

You can execute Data Acquisition Toolbox functions from the command line or through MATLAB programs.

Based on MATLAB object technology, the toolbox provides functions for creating device objects that are directly associated with your hardware. These objects include base properties that apply to all supported hardware, such as sample rate, trigger settings, and channel properties. They also include device-specific properties that let you access the specific features and capabilities of your hardware.

Using Device Objects

Device objects provide a gateway to the hardware's functionality and enable you to control the behavior of your acquisition. For example, you can execute any supported analog input task via an analog input object created in MATLAB.

Analog Input

The analog input functions let you acquire signals from your hardware. You can create an analog input object, add channels to the object, acquire data to memory, read data into the workspace, and preview the most recently acquired data.

Analog Output

Analog output functions let you send signals out to your hardware. You can create an analog output object, add channels, queue data sets to be output, and generate analog signals.

Two channels of live audio data displayed and analyzed using the SoftScope software oscilloscope interface. SoftScope's measurement capabilities find the peak voltage of data streaming in through channel 1.

114
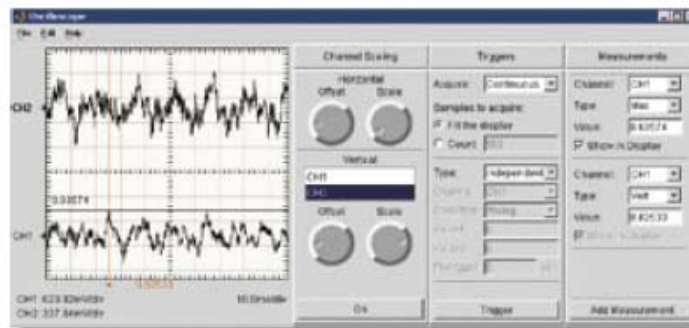
Digital I/O

Digital I/O functions enable you to generate or read digital signals using your hardware. You can create digital I/O objects, add lines, send data to the hardware, and read data into the workspace.

Channels and Lines

Data Acquisition Toolbox channels and lines are mapped to your hardware's channels and lines. The toolbox supports an unlimited number of channels/lines, enabling you to use as many as your hardware permits.

Controlling Your Acquisition

The Data Acquisition Toolbox supports a wide range of functions for controlling your acquisition. For example, you can set event information, evaluate the acquisition status, define triggers and callbacks, preview data while the device is running, and perform analysis on-the-fly. The toolbox also supports several hardware-specific properties that can be displayed and customized to your specifications.

Managing Data

Functions are provided for previewing and extracting your data for analysis. The toolbox streams data into MATLAB in double-precision floating-point format, enabling you to work with the data just as you would with any other matrix in MATLAB. You can also stream in data using a native hardware format.

Logging Data

Functions are available for logging data to disk, memory, or both while the analog input object is running. You can log data, events, and errors. In addition, functions are provided for extracting data from toolbox-generated log files.
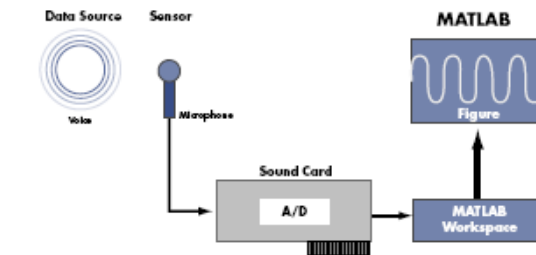
Setup for a data acquisition and analysis session. The Data Acquisition Toolbox enables MATLAB to interface with the data acquisition boards, such as sound cards.

Using SoftScope

SoftScope is a graphical user interface for selecting and configuring data acquisition sources and then acquiring, viewing, and analyzing data using a familiar, oscilloscope-like interface. SoftScope lets you quickly verify hardware operation and perform live data analysis using a library of built-in measurement functions. You can extend SoftScope with your own analysis functions and export data from SoftScope to the MATLAB workspace.

Incorporating Events and Callbacks

Most data acquisition tasks are initiated by events. An event occurs at a specific time after a condition is met. Event types supported by the Data Acquisition Toolbox include:

- Start and stop
- Number of samples acquired
- Errors
- Triggers
- Number of samples output

Events may result in one or more callbacks. All the preceding event types execute an M-file function that you specify.

Handling Errors

The Data Acquisition Toolbox provides a consistent set of error and warning messages. If a hardware error message is not handled by the toolbox, an "external error" is reported with the vendor-specific hardware error message.

Converting Engineering Units

The Data Acquisition Toolbox automatically converts acquired data into values that represent specific engineering units (for example, volts or Newtons). The toolbox directly supports linear scaling and offsets. In addition, you can use MATLAB to apply nonlinear calibration curves. You can set engineering unit conversions for each data channel.

Evaluating Your Acquisition

You can evaluate the status of your acquisition and the available data acquisition resources, including installed hardware, hardware drivers, and adaptors, by displaying:

- Device object and channel status
- Hardware information
- Data acquisition engine information

115
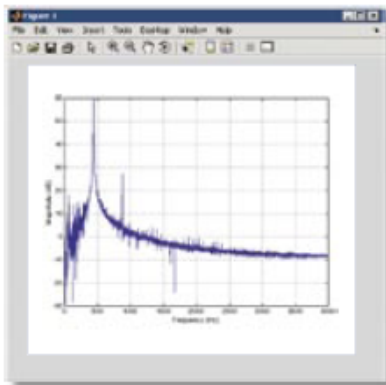
```matlab
% Create an analog input object to communicate with the
% data acquisition device.
ai = analoginput('winsound');
addchannel(ai, 1);

% Configure the object to acquire 2 seconds of data at 8000 Hz.
Fs = 8000;
duration = 2;
set(ai, 'SampleRate', Fs);
set(ai, 'SamplesPerTrigger', duration*Fs);

% Start the acquisition and retrieve the data.
start(ai);
data = getdata(ai);

% Determine the frequency components of the data.
xfft = abs(fft(data));
mag = 20*log10(xfft);
mag = mag(1:end/2);
plot(mag);

% Clean-up
delete(ai);
clear ai;
```

A script illustrating the four steps of a typical MATLAB data acquisition session: creation, configuration, acquisition, and clean-up. A few lines of code let you acquire 2 seconds of data from a data acquisition board, calculate the frequency components of the data, and plot the results in MATLAB.

Required Products
MATLAB

Related Products
Signal Processing Toolbox. Perform signal processing, analysis, and algorithm development.

Curve Fitting Toolbox. Perform model fitting and analysis

Instrument Control Toolbox. Control and communicate with test and measurement instruments

Image Acquisition Toolbox. Acquire images and video from industry-standard hardware

MATLAB Report Generator. Automatically generate documentation for MATLAB applications and data

MATLAB Compiler. Convert MATLAB applications into stand-alone applications and software components

Platform and System Requirements
For platform and system requirements, visit
www.mathworks.com/products/daq ∎

For demos, application examples,
tutorials, user stories, and pricing:
• Visit www.mathworks.com
• Contact The MathWorks directly
  US & Canada 508-647-7000

Benelux	+31 (0)182 53 76 44
France	+33 (0)1 41 14 67 14
Germany	+49 (0)241 470 750
Italy	+39 (011) 2274 700
Korea	+82 (0)2 6006 5114
Spain	+34 91 799 1880
Sweden	+46 (8)505 317 00
Switzerland	+41 (0)31 950 60 20
UK	+44 (0)1223 423 200

Visit www.mathworks.com to
obtain contact information for authorized
MathWorks representatives in countries
throughout Asia Pacific, Latin America,
the Middle East, Africa, and the rest
of Europe.

The MathWorks   Tel: 508.647.7000   info@mathworks.com   www.mathworks.com

9701v05 11/05